ABSTRACT

ELECTRO-MAGNETIC CONTROL OF CYLINDER WAKE

by
Zhihua Chen

The objective of this dissertation is to develop open and closed-loop control algorithms for manipulating wake flows past a solid cylinder in an electrically low-conducting fluid (e.g. seawater). The intent is to avoid both vortex shedding and flow separation from the body. It is desired to reduce the mean drag significantly and prevent the lift from becoming non-zero at all times. This is achieved through the introduction of a Lorentz force in the azimuthal direction generated by an array of permanent magnets and electrodes located on the solid structure. The array of actuators offers the advantage of making the Lorentz force time and space dependent. More specifically, a closed-loop control algorithm has been derived from the equations of motion capable of determining at all times the intensity of the Lorentz force in order to control the flow. This is achieved first, independently of the flow (open loop algorithm) and second, based on some partial flow information measured on the surface of the solid body (closed-loop algorithm). The latter offers the advantage of requiring a significantly reduced amount of control power. After considering the flow past a fixed solid structure, there is control of the more complex flow-structure interaction that occurs when the body is free to move. Thus it is possible to prevent any flow induced vibration from occurring.

ELECTRO-MAGNETIC CONTROL OF CYLINDER WAKE

by
Zhihua Chen

A Dissertation
Submitted to the Faculty of
New Jersey Institute of Technology
in Partial Fulfillment of the Requirements for the Degree of
Doctor of Philosophy in Mechanical Engineering

Department of Mechanical Engineering

May 2001

APPROVAL PAGE

ELECTRO-MAGNETIC CONTROL OF CYLINDER WAKE

Zhihua Chen

Nadine Aubry, Ph.D., Dissertation Advisor — Date
Professor, Department of Mechanical Engineering and Mathematical Sciences,
New Jersey Institute of Technology, Newark NJ

Ernest S. Geskin, Ph.D., Committee Member — Date
Professor, Department of Mechanical Engineering,
New Jersey Institute of Technology, Newark NJ

Anthony D. Rosato, Ph.D., Committee Member — Date
Associate Professor, Department of Mechanical Engineering,
New Jersey Institute of Technology, Newark NJ

Pushpendra Singh, Ph.D., Committee Member — Date
Assistant Professor, Department of Mechanical Engineering,
New Jersey Institute of Technology, Newark NJ

Burt Tilley, Ph.D., Committee Member — Date
Assistant Professor, Department of Mathematical Sciences,
New Jersey Institute of Technology, Newark NJ

BIOGRAPHICAL SKETCH

Author: Zhihua Chen

Degree: Doctor of Philosophy in Mechanical Engineering

Place of Birth: Hunan, P. R. China

Undergraduate and Graduate Education:

- Doctor of Philosophy in Mechanical Engineering, 2001
  New Jersey Institute of Technology, Newark, NJ

- Doctor of Philosophy in Power Engineering, 1997
  Nanjing University of Science & Technology, Nanjing, P. R. China

- Master of Science in Mechanical Engineering, 1994
  Nanjing University of Science & Technology, Nanjing, P. R. China

- Bachelor of Science in Agricultural Machinofacture, 1989
  Hunan Agriculture University, Changsha, P. R. China

Major: Mechanical Engineering

Publications:

Nadine Aubry and Zhihua Chen, Electro-magnetic feedback control of wake flows, ICTAM Symposium, Aug. 27-Sep. 2, 2000, Chicago, Illinois, USA.

Nadine Aubry, Zhihua Chen and Fu Li, Closed loop control of wake flows, IUTAM Symposium on Bluff Body Wakes and Vortex-induced Vibrations, 13-16 June, 2000, Marseille, France.

To my family and parents

ACKNOWLEDGMENT

I would like to express my deepest gratitude to my advisor, Professor Aubry, without whom the completion of this dissertation would have been impossible, for her continuous encouragement and support during the past several years. Her generous advice and constant faith have made my time with her a very challenging and rewarding experience.

Special thanks are given to Professor Geskin, Professor Rosato, Professor Singh and Professor Tilley for actively serving in my dissertation committee.

I would also like to thank all the researchers in the Computational Fluid Dynamics Laboratory, for many useful discussions and continued help, all contributing to a friendly environment.

Finally, I am very indebted to my wife, Aihua Zhang, for giving me great support that helped me concentrate on my research.

TABLE OF CONTENTS

Chapter **Page**

LIST OF FIGURES

LIST OF FIGURES
(Continued)

Figure **Page**

LIST OF FIGURES
(Continued)

Figure **Page**

LIST OF FIGURES
(Continued)

Figure **Page**

LIST OF FIGURES
(Continued)

Figure **Page**

CHAPTER 1

INTRODUCTION

1.1 Background

The flow past a circular cylinder is an important and fundamental topic in fluid mechanics. It also remains one of the most investigated and best understood bluff body wake problems. It is well known that at very low Reynolds numbers ($Re \ll 1$), the flow is steady and symmetric with respect to both the vertical axis and the horizontal centerline. Here, the Reynolds number Re is defined by $Re = 2u_\infty a/\nu$, where u_∞ is the free-stream velocity far from the cylinder, a is the cylinder radius and ν is the kinematic viscosity. As the Reynolds number increases, a change occurs in the flow patterns, resulting in the break-up of the upstream-downstream symmetry with respect to the vertical axis; indeed, the flow separates on the downstream side, forming two counter-rotating eddies which become more and more elongated as time increases until they reach a maximal size. The latter increases with Reynolds number. The eddies of maximal size remain stable and attached to the body for Reynolds numbers below the critical value ($Re_c \geq 47$). Above Re_c, unsteadiness arises spontaneously even though all the imposed conditions are being held steady and vortex shedding appears behind the circular cylinder, resulting in the well-known Karman vortex street. At a higher Reynolds number ($Re \geq 200$), the flow becomes three-dimensional and turbulent, and vortex shedding consists of more complicated patterns. Only recently, much progress has been made in the understanding of the secondary instability towards a spanwise-periodic three-dimensional flow (Williamson 1996, Henderson 1996 *et al*).

The appearance of vortex shedding is accompanied by a large fluctuation of drag and lift forces, which may cause structural vibrations and acoustic noise, and

shorten the life of the solid structure. Therefore, the ability to control the wake of a bluff body is of great importance from a practical engineering viewpoint. The goal here is to reduce drag, increase mixing or heat transfer, or enhance combustion (Park *et al* 1994). In many cases, this is achieved by either enhancing or suppressing vortex shedding.

Over the years, many control methods have been developed. These include passive open loop control techniques, such as the use of a splitter plate (Roshko 1955; Gerrard 1966; Apelt, West & Szewczyk 1973; Apelt & West 1975; Unal & Rockwell 1988; Cimbala & Garg 1991; Kwon & Choi 1996 *et al*;), base bleed (Wood 1964; Bearman 1967; Schumm, Berger & Monkewitz 1994 *et al*), and a small secondary cylinder (Strykowski & Sreenivasan 1990). These techniques do not require any energy input to the flow. In contrast, active open loop control methods have also been investigated widely. These include the rotary oscillation of the cylinder (Tokumaru & Dimotakis 1991, Kang and Choi 1999), the insertion of additional vortices in the flow (Tang & Aubry 1997 *et al*), wake heating (Noto 1985; *et al*), forced cylinder vibrations (Wehrmann 1965, *et al*), acoustic forcing (Blevins 1985; You and Choi *et al* 1998) and time-harmonic forcing (Karniadakis & Triantafyllou 1989).

The feedback control of vortex shedding has been investigated theoretically in the last few years. An approach for controlling fluid flow has been examined by Abergel & Temam (1990) and Sritharan (1991). Monkewitz (1989) and Park *et al* (1993) studied the possibility of feedback control via global oscillations. Roussopoulos (1993) performed experiments both in wind and in an open water channel; his results have shown that up to 10 units of Reynolds numbers above the onset of vortex shedding, it was possible to suppress the wake. Park *et al* (1994) showed numerically that complete suppression of vortex shedding can be achieved at

$Re = 60$, using a single sensor and a pair of blowing/suction actuators. Gunzburger *et al* (1996) implemented the latter feedback control scheme in a physical experiment by sensing the pressure distribution on the cylinder surface, and using actuators consisting of injection and suction of fluid through orifices on the surface. They reported a remarkable lift reduction without, however, being able to suppress vortex shedding completely.

Min and Choi (1999) developed a systematic method of controlling vortex shedding behind a bluff body using a suboptimal feedback control procedure developed by Abergel *et al* (1990) (choi *et al* (1993)). In order to investigate the performance of their control algorithm, they chose three cost functions which are all related to the pressure distribution on the cylinder surface. Their results showed that the technique can reduce the drag and lift significantly and weaken, or even suppress, vortex shedding at the Reynolds number values $Re = 100$ and $Re = 160$.

Some control methods are successful at controlling or suppressing vortex shedding through a large modification (e.g. a splitter plate of length $10a$ or a flapping foil of chord $4a$, where a is the radius of the cylinder. Some other approaches, such as the insertion of a small cylinder in the wake, are small local modifications, but are usually restricted to a small range of Reynolds numbers; in many cases, control methods are based on physical intuition and the qualitative observation of flow phenomena. Even in the cases where vortex shedding can be controlled or suppressed successfully, it is often not practical for applications in real engineering situations.

1.2 Electro-Magnetic Control of Vortex Shedding

In an electrically conducting fluid (such as sea water), it is possible, through the motion of a conducting material in a magnetic field, to generate an electromotive force and cause an electric current of density $\vec{j}$ to flow. The current induces its own magnetic field and organizes a volume force distribution inside the fluid. The induced currents, together with the external magnetic field, generate a Lorentz force $\vec{F_l}$ which, in turn, influences the fluid flow. It is worthwhile noticing that the Lorentz force can be produced by the application of either a magnetic field or a combination of magnetic and electric fields. In such MHD (Magneto-Hydro-Dynamic) flows, the Lorentz force distribution can be adapted to a prescribed, desired action through the application of suitably chosen magnetic and electric fields. However, in MHD flows with a weakly conducting fluid (such as sea water), the induced magnetic and electric fields are negligible. Therefore, the possibility of affecting the flow effectively requires that an external electric field be imposed. In such EMHD (electro-magneto-hydro-dynamic) flows, electrical currents, fed via electrodes to a low conducting fluid, will only slightly penetrate into the fluid, so the Lorentz force will be non-negligible only in some vicinity of the electrodes. Such electro-magnetic forces in electrically conducting fluid provide an alternative flow control method. In order to achieve a specific goal, one needs to determine the appropriate configuration of external magnetic and electric fields yielding some optimal Lorentz force distribution.

The main advantage of the latter control strategy for electrically conducting fluids is that the Lorentz force acts on a volume of the flow, and it may be possible to tune the force to act only in specific regions of the flow. Many techniques using electric and magnetic fields have been proposed in weakly conducting fluids, in order to achieve turbulent boundary layer control, transition delay and drag reduction.

For instance, Nosenchuck and Brown (1995) performed experiments by injecting an electrolyte into a non-conducting pure water turbulent boundary layer. They employed special arrangements of single actuators "*tiles*" ; these tiles were designed in order to obtain a global modification of the near wall flow. The authors reported a a dramatic reduction in turbulence intensity and in skin friction. Gailitis and Lielansis (1961) developed a specific arrangement which consisted of alternating electrodes and magnets along the streamwise direction in order to achieve drag reduction; the technique was tested recently by Henoch and Stace (1995) to control a turbulent boundary layer. In their experiment, the Lorentz force is generated by the simple strip-like geometry shown in Figure 2.1. Their results showed an increase in drag at low Reynolds numbers, and a small drag decrease at high Reynolds numbers. Using the same geometry, Crawford and Karniadakis (1997) performed numerical simulations based on a spectral element method and corroborated the slight net increase in drag at low Reynolds numbers. More precisely, they simulated a channel flow subjected to a streamwise Lorentz force applied on one wall. The simulations were performed at the Reynolds number $Re = 200$ and the interaction parameter values $N = 0.1$ and $N = 0.4$. Here, the interaction parameter is defined as the ratio between the Lorentz force intensity to the inertia forces. The authors find a shear stress increase on the controlled wall in both cases. Such an increase is due to the fact that the Lorentz force distribution acts as a source of spanwise and normal vorticity and, therefore, influences the turbulent flow.

Regarding the flow past a cylinder, it was experimentally demonstrated by Lahjomri *et al* (1993) that a streamwise magnetic field leads to a delayed onset of vortex shedding. On the numerical side, Mutschke *et al* (1997, 1998) carried out two-dimensional (2-D) and three-dimensional (3-D) stability analyses for a wake flow subjected to a streamwise magnetic field and demonstrated the suppression of the instability for the 2-D problem.

Weier and co-workers (1998) presented results from flow visualizations and numerical calculations on the active open loop control of the flow around a cylinder by means of electro-magnetic forces. The main focus of their research consisted of separation control, drag reduction, and modification of the cylinder wake structure. A cylindrical test body was covered with electrodes and magnets whose role was to create a Lorentz force parallel to the body surface. Their results showed that Lorentz forces directed with the mean flow are able to prevent the boundary layer from separating away from the solid body.

Although many experiments and numerical analyses have been carried out for such MHD flows, little is known about the instability and transition scenarios except for the general belief that magnetic fields have a damping influence. Due to the difficulty of flow measurements in liquid metal flows at small Reynolds numbers, all known experimental results are at relatively high Reynolds numbers. Furthermore, there has not been any investigation on the design of *reactive* flow control based on some instantaneous flow information for these flows.

1.3 Control of Vortex-Induced Vibration

The appearance of vortex shedding, accompanied by the fluctuation of drag and lift, may cause structural vibrations of the solid body. Due to the destructive effect of such vortex-induced vibrations on offshore structures, bridges, towers and heat exchangers, vortex shedding and its control have attracted the interest of many researchers over the years.

Much experimental work has been performed on flows over elastic structures. Vandiver (1991) has performed field experiments to examine the factors that are important in predicting flow induced vibrations of long flexible cables. Griffin (1992)

has compiled many experimental results to demonstrate the relationship between the cross-flow vibration amplitude and the mass-damping product. Brika & Laneville (1993) performed an experimental study of the vortex-induced oscillations of a long flexible circular cylinder. The stationary amplitudes they obtained exhibited a hysteresis loop somewhat different from observations resulting from earlier studies. The concept of *lock-in* vortex shedding has been revised by many researchers. Atsaratanee & Benaroya *et al* carried out experiments to characterize the flow in the near wake of a stationary and freely-oscillating cylinder in and near the lock-in range.

Techet and Triantafyllou (1998) measured the forces at both ends of the forced harmonic motion and free vibrations of uniform and tapered cylinders at the Reynolds number value, $Re = 3800$. Their results showed that free-vibration tests of a uniform cylinder with low equivalent structural damping yield the amplitude response curve as a function of the nominal reduced velocity in agreement with previous results (Khalak & Williamson 1996). In addition, the Digital Particle Image Velocimetry (DPIV) technique is used widely to unveil the shedding patterns of the flow (Williamson and Roshko 1988, Techet & Triantatyllou 1998).

Experimental studies of vortex-induced vibrations of a cylinder have established some important conclusions. For instance, it is well-known that the vortex induced vibration phenomenon is a self-limiting process, with an upper bound for the amplitude of the vibrations. The magnitude of the lift force depends on the vibration amplitude, which itself has some relation with the reduced damping and the phase difference between the lift force and the motion of the cylinder.

Numerical work has not been as extensive as experimental studies. Recently, progress has been made in understanding and modeling the near-wake dynamics of bluff bodies. Such progress has led to new predictive models that give an accurate

description of the flow field as well as offer an opportunity to revisit the vortex-induced vibration problem.

Dutsch *et al* (1998) investigated numerically the laminar flow induced by the harmonic in-line oscillation of a circular cylinder. The drag and the added-mass coefficients were calculated and compared for different grid levels and time steps. With the use of a spectral element spatial discretization, Blackburn and Henderson (1996) investigated the vortex-induced vibration problem by solving the two-dimensional Navier-Stokes equations in an accelerating frame of reference attached to the cylinder at the Reynolds number value $Re = 250$. Newman and Karniadakis (1995, 1997) performed a direct numerical simulation study of the flow past a freely vibrating cable using body-fitted coordinates at the Reynolds numbers $Re = 100$ and $Re = 200$. Three cases of cable motion were considered: (i) the cable was stationary and straight, (ii) the cable motion was specified (standing wave) and (iii) the cable was free to interact with the flow. The results obtained were consistent with experimental data. Zhou, So and Lam (1998) studied a two-dimensional flow past an elastic circular cylinder using the VIC (vortex-in-cell) discrete vortex method to investigate the responses of the cylinder, the induced forces on the cylinder, and the effects of cylinder motion on the vortex structure in the wake.

So far, studies regarding vortex-induced vibrations do not provide a clear understanding of the character and mechanism of this phenomenon. In addition, little work has been done for the control of vortex-induced vibrations. In this thesis, we will develop a novel feedback control algorithm and test it numerically. Our goal is to control both vortex shedding and vortex-induced vibrations.

1.4 Research Objectives

The purpose of our work is to develop both open loop and closed-loop control algorithms for manipulating wake flows past a fixed cylinder in an electrically low-conducting fluid (e.g. seawater). Our goal is to avoid flow separation from the surface of the body and fully suppress vortex shedding.

Emerging closed-loop control techniques invite a fundamental question: Based on some partial information on the flow dynamics, can one design an efficient control algorithm to reach a desirable effect? Since we are interested in low-conducting fluids, we concentrate here on the possibility of manipulating a fluid flow by means of arrays of electrodes and permanent magnets generating electro-magnetic body forces, i.e. Lorentz forces, in the fluid. The advantage of this non-invasive technique is that it acts on an extended part of the fluid volume rather than being limited to the solid surface. In addition, it can be miniaturized and permit flow manipulation in the sub-micrometer world.

Since the phenomenon of flow separation is due to the loss of momentum close to the separation point, a promising technique seems to be the generation of a *tangential* Lorentz force at the appropriate azimuthal location on the cylinder surface. Such a force originates, for instance, from alternating electrodes and magnets N, +, S, -, etc. along the span of the cylinder. The electrodes and magnets are arranged so that the resulting Lorentz force is symmetric with respect to the flow centerline. It was recently demonstrated experimentally and numerically that an array of electrodes and magnets distributed all around the body and energized at all times can suppress vortex shedding and delay flow separation. Here that more localized electrode and magnet arrays have been shown, activated only at times when they are needed, can achieve similar results and even suppress separation completely.

Our numerical simulation is based on the two-dimensional formulation of the Navier-Stokes equations in an exponential-polar coordinate system. The exponential mapping allows us to deal with a very large physical domain while the computational box remains relatively small. This allows us to avoid the well-known blockage effect. The *vorticity/streamfunction* formulation of the Navier-Stokes equations expressed with respect to dimensionless variables has been chosen. These equations are subject to the no-slip boundary conditions on the surface of the body and the two-dimensional potential flow at infinity. The impulsive start is simulated by using potential flow as the initial condition, except on the surface of the cylinder where the absence of slip is imposed. Everywhere, except on the surface of the cylinder, the flow is initially potential. An adaptive scheme is developed in order to increase the efficiency of our numerical code. This scheme consists of moving the boundary used for the vorticity transport equation further and further away from the body as the vorticity is transported outward. Thus our full physical domain has been divided into two subdomains, Region I and Region II, the vorticity being fully contained in Region I. The numerical method consists of an alternating-direction-implicit (ADI) algorithm for the vorticity transport equation and fast Fourier transforms (FFT) for the Poisson equation with second-order accuracy. More details on the numerical simulation can be found in Aubry and Tang (1998). In the present work, we add the electro-magnetic force as a body force in the right-hand side of the Navier-Stokes equations. After reproducing the results reported in Weier *et al* (1998) for the case of a time independent, uniformly distributed force around the surface of the body, we introduce novel open loop and closed-loop control algorithms.

1.5 Summary of this Study

This dissertation is organized as follows: In Chapter 2, we introduce the governing equations and the numerical methods to integrate the latter. Chapter 3 reports our results concerning the open loop control algorithm using the Lorentz force either applied all around the cylinder surface or acting on a portion of the cylinder surface only. Applying the Lorentz force has been found on only a portion of the cylinder area can have an effect on the flow dynamics very similar to that obtained with the Lorentz force distributed along the entire surface. However, the former technique saves energy. The results have been described obtained in the case where the Lorentz force is no longer constant but sinusoidal with various forcing frequencies. For forcing frequencies close to the Strouhal frequency, lock-in occurs even at low values of the Lorentz force amplitude. In chapter 4, we describe our feedback control procedures at both zero total drag coefficient and zero pressure drag coefficient. In both cases, vortex shedding have been suppressed behind the cylinder completely. In chapter 5, we numerically simulate vortex-induced vibrations of the cylinder at the Reynolds number values $Re = 100$ and $Re = 200$. The feedback control method developed in Section 4 has been applied to the flow past the vibrating cylinder and show that vortex shedding can be suppressed in this case as well. Finally, we summarize our findings in Chapter 6.

CHAPTER 2

COMPUTATIONAL METHODS

2.1 Governing Equations

The case for which the electrically conducting fluid has been considered being the incompressible viscous liquid around an insulating circular cylinder in an external uniform magnetic field, and the only body force is the Lorentz force. The two-dimensional incompressible Navier-Stokes equations then become as follows:

$$\frac{\partial u}{\partial x} + \frac{\partial v}{\partial y} = 0 \tag{2.1}$$

$$\frac{\partial u}{\partial t} + u\frac{\partial u}{\partial x} + v\frac{\partial u}{\partial y} = -\frac{1}{\rho}\frac{\partial P}{\partial x} + \nu\left(\frac{\partial^2 u}{\partial x^2} + \frac{\partial^2 u}{\partial y^2}\right) + \frac{F_{lx}}{\rho} \tag{2.2}$$

$$\frac{\partial v}{\partial t} + u\frac{\partial v}{\partial x} + v\frac{\partial v}{\partial y} = -\frac{1}{\rho}\frac{\partial P}{\partial y} + \nu\left(\frac{\partial^2 v}{\partial x^2} + \frac{\partial^2 v}{\partial y^2}\right) + \frac{F_{ly}}{\rho} \tag{2.3}$$

where $\vec{F_l}$ is the Lorentz force that results from the vector product of the current density $\vec{j}$ $(Amps/m^2)$ and the magnetic induction $\vec{B}$ $(Tesla)$

$$\vec{F_l} = \vec{j} \times \vec{B}. \tag{2.4}$$

Defining the vorticity $\Omega = \nabla \times \vec{u}$ and the streamfunction Ψ as follows:

$$\Omega = \frac{\partial v}{\partial x} - \frac{\partial u}{\partial y},$$

$$u = \frac{\partial \Psi}{\partial y}, \qquad v = -\frac{\partial \Psi}{\partial x}.$$

The equations of motion expressed in terms of the vorticity and streamfunction can be derived from the above equations (2.1)–(2.3):

$$\frac{\partial \Omega}{\partial t} + u\frac{\partial \Omega}{\partial x} + v\frac{\partial \Omega}{\partial y} = \nu\left(\frac{\partial^2 \Omega}{\partial x^2} + \frac{\partial^2 \Omega}{\partial y^2}\right) + \frac{1}{\rho}\left(\frac{\partial F_{ly}}{\partial x} - \frac{\partial F_{lx}}{\partial y}\right) \tag{2.5}$$

$$\frac{\partial^2 \Psi}{\partial x^2} + \frac{\partial^2 \Psi}{\partial y^2} = -\Omega \tag{2.6}$$

Introducing the cylindrical coordinates system

$$\begin{aligned} x &= r cos\theta \\ y &= r sin\theta \\ F_{lx} &= F_{lr} cos\theta - F_{l\theta} sin\theta \\ F_{ly} &= F_{lr} sin\theta + F_{l\theta} cos\theta \end{aligned}$$

Equation (2.5)then becomes:

$$\frac{\partial \Omega}{\partial t} + u_r \frac{\partial \Omega}{\partial r} + \frac{1}{r} u_\theta \frac{\partial \Omega}{\partial \theta} = \nu [\frac{1}{r} \frac{\partial}{\partial r} (r \frac{\partial \Omega}{\partial r}) + \frac{1}{r^2} \frac{\partial^2 \Omega}{\partial \theta^2}] + \frac{1}{\rho} [\frac{1}{r} \frac{\partial (r F_{l\theta})}{\partial r} - \frac{1}{r} \frac{\partial F_{lr}}{\partial \theta}] \quad (2.7)$$

Considering the following dimensionless variables

$$\begin{aligned} &\Omega^* = \Omega a / u_\infty, \qquad \Psi^* = \Psi / a u_\infty, \qquad u_r^* = u_r / u_\infty, \\ &u_\theta^* = u_\theta / u_\infty, \qquad t^* = t u_\infty / a, \qquad \theta^* = \theta, \\ &r^* = r / a, \qquad B^* = B / B_0, \qquad j^* = j / \sigma u_\infty B_0 \end{aligned}$$

where a is cylinder radius, u_∞ denotes the free-stream velocity. B_0 and σ refer to the magnetic field and the electrical conductivity, respectively.

For the sake of simplicity of the presentation, hereafter we drop the star superscript for the dimensionless variables, and introduce the exponential-polar coordinates system (ξ, η) defined as:

$$r = e^{2\pi\xi}, \qquad \theta = 2\pi\eta$$

Now a similar analysis has been performed to derive the streamfunction equation (2.6), so that the *vorticity/streamfunction* formulation of the Navier-Stokes

equations in the transformed coordinates becomes:

$$\begin{aligned} E\frac{\partial\Omega}{\partial t}+\frac{\partial(U_r\Omega)}{\partial\xi}+\frac{\partial(V_\theta\Omega)}{\partial\eta} &= \frac{2}{Re}(\frac{\partial^2\Omega}{\partial\xi^2}+\frac{\partial^2\Omega}{\partial\eta^2}) \\ &+ NE^{\frac{1}{2}}(\frac{\partial F_\theta}{\partial\xi}+2\pi F_\theta-\frac{\partial F_r}{\partial\eta}) \qquad (2.8) \\ \frac{\partial^2\Psi}{\partial\xi^2}+\frac{\partial^2\Psi}{\partial\eta^2} &= -E\Omega \qquad (2.9) \end{aligned}$$

where U_r, V_θ and E are new dependent variables defined as

$$\begin{aligned} U_r &= E^{\frac{1}{2}}u_r=\frac{\partial\Psi}{\partial\eta} \\ V_\theta &= E^{\frac{1}{2}}u_\theta=-\frac{\partial\Psi}{\partial\xi} \\ E &= 4\pi^2e^{4\pi\xi} \end{aligned}$$

In Equation (2.8) the dimensionless parameter, referred to as "*interaction parameter*"

$$N=\frac{\sigma B_0^2a}{\rho u_\infty}=\frac{j_0B_0a}{\rho u_\infty^2},$$

appears in the non-dimensionalization process. In addition, the usual Reynolds number is also seen.

$$Re=\frac{2u_\infty a}{\nu}.$$

It is clear that the interaction parameter N is the ratio of the electromagnetic force to the inertia forces. In the present work, all fluid properties such as density (ρ), kinematic viscosity (ν), and electric conductivity (σ) are assumed to be constant, and the cylinder is considered to be electrically insulated.

2.1.1 Initial and Boundary Conditions

Except on the surface of the cylinder where the absence of slip is imposed, the flow can be considered initially potential. Since at the surface of the cylinder, the the

derivative $\partial^2\Psi/\partial\eta^2$ is equal to zero, the expression of the vorticity can be obtained from Equation (2.9). At $t = 0$, the following equations thus hold:

Away from the cylinder surface, $\xi > 0$

$$\Omega = 0, \qquad \Psi = -2sh(2\pi\xi)sin(2\pi\eta)$$

On the cylinder surface, $\xi = 0$

$$\Omega = -\frac{1}{E}\frac{\partial^2\Psi}{\partial\xi^2}.$$

The boundary conditions for Equations (2.8) and (2.9) consist of (i) the no-slip boundary condition on the surface, and (ii) the potential flow at the outer boundary of the domain (referred to as infinity):

Away from the cylinder surface, $\xi = \xi_\infty$

$$\Omega = 0, \qquad \Psi = -2sh(2\pi\xi)sin(2\pi\eta)$$

On the cylinder surface, $\xi = 0$

$$\Psi = 0, \qquad \Omega = -\frac{1}{E}\frac{\partial^2\Psi}{\partial\xi^2}.$$

2.1.2 Numerical Methods

The vorticity transport equation (2.8) is solved with the use of Alternative-Direction Implicit (ADI) algorithm and the streamfunction equation (2.9) is integrated by means of a Fast Fourier Transform (FFT) algorithm. The accuracy of the numerical scheme is second order in space and first order in time. These techniques are standard and more details can be found in the literature.

An ADI algorithm is implemented to solve the vorticity transport equation (2.8), leading to the discretized formulae:

$$E_i\frac{\Omega^{n+\frac{1}{2}}_{(i,j)}-\Omega^{n}_{(i,j)}}{\frac{1}{2}\Delta t}+\frac{(U_\eta\Omega^{n+\frac{1}{2}})_{(i,j+1)}-(U_\eta\Omega^{n+\frac{1}{2}})_{(i,j-1)}}{2\Delta\eta}-\frac{2}{Re}\frac{\Omega^{n+\frac{1}{2}}_{(i,j+1)}-2\Omega^{n+\frac{1}{2}}_{(i,j)}+\Omega^{n+\frac{1}{2}}_{(i,j-1)}}{\Delta\eta^2}=$$
$$-\frac{(U_\xi\Omega^{n})_{(i+1,j)}-(U_\xi\Omega^{n})_{(i-1,j)}}{2\Delta\xi}+\frac{2}{Re}\frac{\Omega^{n}_{(i+1,j)}-2\Omega^{n}_{(i,j)}+\Omega^{n}_{(i-1,j)}}{\Delta\xi^2}$$
$$+NE_i^{\frac{1}{2}}[\frac{F_{l\theta(i+1,j)}-F_{l\theta(i-1,j)}}{2\Delta\xi}+2\pi F_{l\theta(i,j)}]$$

$$E_i\frac{\Omega^{n+1}_{(i,j)}-\Omega^{n+\frac{1}{2}}_{(i,j)}}{\frac{1}{2}\Delta t}+\frac{(U_\xi\Omega^{n+1})_{(i+1,j)}-(U_\xi\Omega^{n+1})_{(i-1,j)}}{2\Delta\xi}-\frac{2}{Re}\frac{\Omega^{n+1}_{(i+1,j)}-2\Omega^{n+1}_{(i,j)}+\Omega^{n+1}_{(i-1,j)}}{\Delta\xi^2}=$$
$$-\frac{(U_\eta\Omega^{n+\frac{1}{2}})_{(i,j+1)}-(U_\eta\Omega^{n+\frac{1}{2}})_{(i,j-1)}}{2\Delta\eta}+\frac{2}{Re}\frac{\Omega^{n+\frac{1}{2}}_{(i,j+1)}-2\Omega^{n+\frac{1}{2}}_{(i,j)}+\Omega^{n+\frac{1}{2}}_{(i,j-1)}}{\Delta\eta^2}$$
$$+NE_i^{\frac{1}{2}}[\frac{F_{l\theta(i+1,j)}-F_{l\theta(i-1,j)}}{2\Delta\xi}+2\pi F_{l\theta(i,j)}]$$

where U_ξ, U_η are ξ, η velocity components which are calculated at the n^{th} time step.

The streamfunciton was solved by adopting an efficient algorithm using fast Fourier transforms (FFT) with second-order accuracy as in Hockney (1970):

$$\frac{\Psi^{n}_{(i+1,j)}-2\Psi^{n}_{(i,j)}+\Psi^{n}_{(i-1,j)}}{\Delta\xi^2}+\frac{\Psi^{n}_{(i,j+1)}-2\Psi^{n}_{(i,j)}+\Psi^{n}_{(i-1,j)}}{\Delta\xi^2}=-E_i\Psi^{n}_{(i,j)}$$

In our numerical scheme, we use

$$\frac{\partial\Omega^{n}_{(0,j)}}{\partial\xi}=\frac{-3\Omega^{n}_{(0,j)}+4\Omega^{n}_{(1,j)}-\Omega^{n}_{(2,j)}}{2\Delta\xi}$$

which gives us second-order accuracy to calculate the vorticity flux in equation (2.18).

2.1.3 Static Symmetric Lorentz Force

From Equation (2.4), the Lorentz force results from the vector product of the current density $\vec{j}$ and the magnetic induction $\vec{B}$. The current density $\vec{j}$, in turn, is given by

Ohm's law as the sum of the current due to the presence of the electric field $\vec{E}$ and the current induced by the motion of the electro-conducting medium at speed $\vec{U}$ in the presence of a magnetic field. That is:

$$\vec{j} = \sigma(\vec{E} + \vec{U} \times \vec{B}),$$

where $\sigma(S/m)$ denotes the electrical conductivity.

In low conducting fluids like seawater, the induced electrical current ($\vec{j} = \sigma\vec{U} \times \vec{B}$) are generally too small to produce any noticeable effect compared to the current associated with the electric field, and is thus neglected. The Lorentz force then reduces to

$$\vec{F_l} = \sigma\vec{E} \times \vec{B}.$$

Experiments show that the external applied current will only penetrate into the liquid within a short distance of the electrodes and will decay rapidly. One can thus assume that the Lorentz force will be effective only in some vicinity of the electrodes, within the boundary layer. Grienberg (1961) used a series expansion to determine the electromagnetic field distributions and found that, within a good approximation, the Lorentz force decays exponentially.

As an example, we show the configuration which was proposed by Gailitis and Lielausis (1961), which consists of alternating streamwise electrodes and magnets over a flat plate and, therefore, produces a Lorentz force in the streamwise direction (Figure 2.1). Here "N" and "S" indicate north and south magnet poles and "+" and "-" indicate positive and grounded electrodes, respectively.

In order to control the cylinder wake, the cylinder is mounted with a special array of electrodes and permanent magnets on the surface as shown in Figure 2.2.

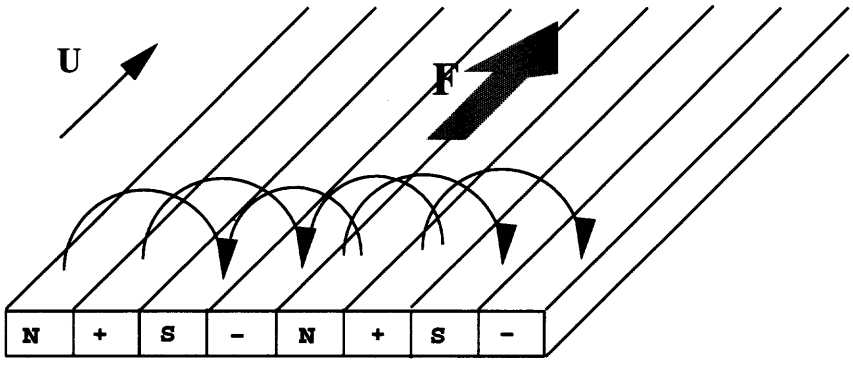

Figure 2.1 Sketch of the streamwise electrodes and magnets over a flat plate (from Crawford and Karniadakis 1997).

This consists of two half cylinders, each obtained from the bend of plate as shown in Figure 2.1. In this way, the Lorentz force on the surface of cylinder is directed parallel to the cylinder surface and keeps the same direction on both half sides (see Figure 2.2c). The force $\vec{F}$ in equation (2.8) is modeled by the simple relation which was given by Weier *et al.* (1998). It is defined as follows:

$$\vec{F} = e^{-\alpha(r-1)} g(\theta) \vec{e_\theta} \qquad with \quad g(\theta) = \begin{cases} 1 & 5° \leq \theta \leq 175° \\ -1 & 185° \leq \theta \leq 355° \\ 0 & \text{elsewhere} \end{cases} \tag{2.10}$$

The above equation is a simplification of the real experimental situation. The slots are located at front and rear stagnation points where no electrodes are present, so the limits of the θ are $5° \sim 175°$ and $185° \sim 355°$. Any radial force component has been neglected. The value α describes the electromagnetic penetration into the liquid which is mainly defined by the electrode spacing and modeled in correspondence to the experimental situation by $\alpha = 5\pi/4$. From the above equation we see that the Lorentz force is symmetric on both sides of the cylinder, and the forces

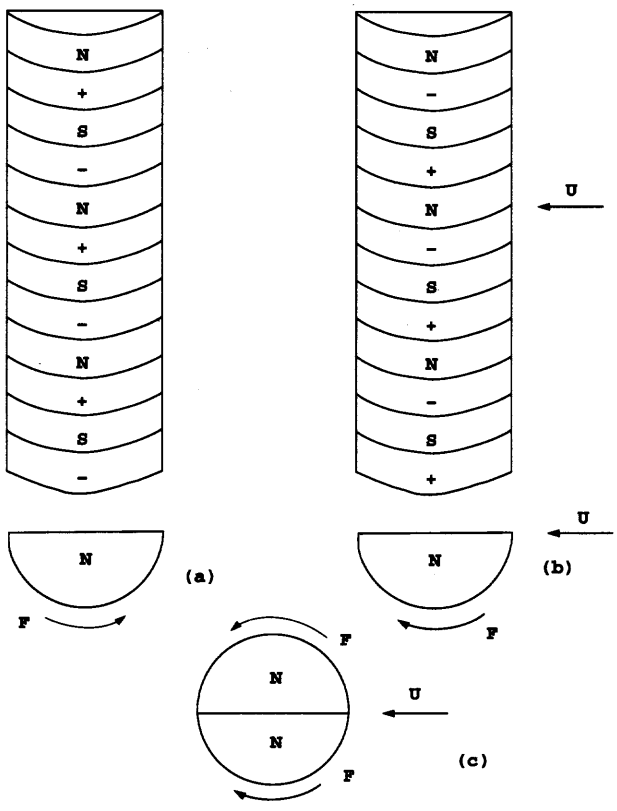

Figure 2.2 Sketch of the cylinder equipped with electrodes and magnets.

on both sides keep the same direction at all the time.

2.1.4 Periodic Symmetric Lorentz Force

Since the Lorentz force is a function of the applied current density, it is easy to implement the sinusoidal force in time by feeding the electrodes in an appropriate manner. In this way, the production of electrolytic bubbles using the time dependent currents can be avoided, and the electrode reactions can be reduced at the same time. Therefore, the corrosion at the anodes should be decreased dramatically. This approach may be more effective from the economical point of view than previous DC model, If the Lorentz force has an excitation frequency f, the dimensionless term

can be $f_e = fa/u_\infty$, then force $\vec{F}$ in equation (2.8) is given by:

$$\vec{F} = cos(\omega t)e^{-\alpha(r-1)}g(\theta)\vec{e_\theta} \tag{2.11}$$

Where $\omega = 2\pi f_e$, t denotes dimensionless time and $g(\theta)$ is given from equation (2.8). Thus, the Lorentz force is symmetrical on both sides of the cylinder and changes direction at a certain frequency f_e.

2.1.5 Periodic Antisymmetric Lorentz Force

If the whole cylinder consisted of the bend of one flat plate, the Lorentz force on both sides of the cylinder would have the same angular direction at every instant. For sinusoidal forcing with an excitation frequency f_e, the Lorentz force can be written in the following form:

$$\vec{F} = cos(\omega t)e^{-\alpha(r-1)}\vec{e_\theta} \tag{2.12}$$

where $\omega = 2\pi f_e$, and t denotes dimensionless time. Thus, the Lorentz force is periodic and antisymmetric.

2.2 Pressure Coefficient

The pressure coefficient at one point θ on the surface of the cylinder can be calculated from the definition

$$C_p^\theta = \frac{P_\theta - P_\infty}{\frac{1}{2}\rho u_\infty^2}$$

The above equation can also be written as

$$C_p^\theta = \frac{1}{\frac{1}{2}\rho u_\infty^2}(P_\theta - P_0) - \frac{1}{\frac{1}{2}\rho u_\infty^2}(P_\infty - P_0) \tag{2.13}$$

where P_0 is the pressure at the front stagnation point. From the Navier-Stokes equation in a MHD flow, we can write

$$\frac{\partial \vec{u}}{\partial t} = -\frac{1}{\rho}\nabla P - (\vec{u}\cdot\nabla)\vec{u} + \nu\nabla^2\vec{u} + \frac{1}{\rho}\vec{F}_l$$

On the surface of the cylinder $\vec{u} = 0$, the above equation becomes:

$$\begin{aligned}
\frac{1}{\rho}\nabla P &= \nu\nabla^2\vec{u} + \frac{1}{\rho}\vec{F}_l \\
&= \nu[\nabla(\nabla\cdot\vec{u}) - \nabla\times(\nabla\times\vec{u})] + \frac{1}{\rho}\vec{F}_l \\
&= -\nu\nabla\times\vec{\Omega} + \frac{1}{\rho}\vec{F}_l
\end{aligned}$$

In two-dimensional cylindrical coordinates, we have:

$$\nabla\times\vec{\Omega} = \frac{1}{r}\frac{\partial\Omega_z}{\partial\theta}\vec{e_r} - \frac{\partial\Omega_z}{\partial r}\vec{e_\theta}$$

Letting $\Omega_z = \Omega$, and considering that the surface of cylinder is defined by $r = 1$, we can write

$$\frac{1}{\rho}\frac{\partial P}{\partial r} = -\nu\left[\frac{1}{r}\frac{\partial\Omega}{\partial\theta}\right]_{r=1} + \frac{1}{\rho}F_{lr} \tag{2.14}$$

$$\left[\frac{1}{\rho r}\frac{\partial P}{\partial\theta}\right]_{r=1} = \nu\frac{\partial\Omega}{\partial r} + \frac{1}{\rho}F_{l\theta} \tag{2.15}$$

Integrating Equation (2.15) in the θ direction from the limit $\theta = 0 \sim \theta$, and writing the equation in the exponential-polar coordinate system (ξ, η) gives:

$$\begin{aligned}
\frac{1}{\rho}(P_\theta - P_0) &= \nu\int_0^\theta \frac{\partial\Omega}{\partial r}d\theta + \frac{1}{\rho}\int_0^\theta F_{l\theta}d\theta \\
&= \nu\int_0^\eta \frac{\partial\Omega}{\partial\xi}d\eta + \frac{2\pi}{\rho}\int_0^\eta F_{l\theta}d\eta
\end{aligned}$$

The above equation can then be written as

$$\begin{aligned}\frac{1}{\frac{1}{2}\rho u_\infty^2}(P_\theta - P_0) &= \frac{2\mu}{\rho u_\infty^2}\int_0^\eta \frac{\partial\Omega}{\partial\xi}d\eta + \frac{4\pi\sigma B_0^2}{\rho u_\infty}\int_0^\eta F_\theta d\eta \\ &= \left[\frac{4a}{Re\, u_\infty}\int_0^\eta \frac{\partial\Omega}{\partial\xi}d\eta + \frac{4\pi N}{a}\int_0^\eta F_\theta d\eta\right]_{a=1,u_\infty=1} \\ &= \frac{4}{Re}\int_0^\eta \frac{\partial\Omega}{\partial\xi}d\eta + 4\pi N\int_0^\eta F_\theta d\eta \end{aligned} \tag{2.16}$$

The Navier-Stokes equation in the r direction for a flow subjected to an MHD field can then be obtained from Equation (2.13) as follows.

$$\frac{\partial u_r}{\partial t} = -\frac{1}{\rho}\frac{\partial P}{\partial r} - u_r\frac{\partial u_r}{\partial r} - \frac{u_\theta}{r}\frac{\partial u_r}{\partial\theta} + \frac{u_\theta^2}{r} - \frac{\nu}{r}\frac{\partial\Omega}{\partial\theta} + \frac{F_{lr}}{\rho}$$

Using the fact that the Lorentz force in the r direction is zero, i.e. $F_{lr} = 0$, we now integrate the previous equation in the r direction from $r = 1 \sim \infty$.

$$\begin{aligned}\frac{1}{\rho}(P_\infty - P_0) = &-\int_1^\infty \frac{\partial u_r}{\partial t}dr - \int_1^\infty u_r\frac{\partial u_r}{\partial r}dr - \int_1^\infty \frac{u_\theta}{r}\frac{\partial u_r}{\partial\theta}dr \\ &+\int_1^\infty \frac{u_\theta^2}{r}dr - \nu\int_1^\infty \frac{1}{r}\frac{\partial\Omega}{\partial\theta}dr\end{aligned}$$

This equation can be written in terms of (ξ, η) as follows.

$$\begin{aligned}\frac{1}{\rho}(P_\infty - P_0) = &-2\pi\int_0^\infty \frac{\partial u_r}{\partial t}e^{2\pi\xi}d\xi - \frac{1}{2}u_\infty^2 - \int_0^\infty u_\theta\frac{\partial u_r}{\partial\eta}d\xi \\ &+2\pi\int_0^\infty u_\theta^2 d\xi - \nu\int_0^\infty \frac{\partial\Omega}{\partial\eta}d\xi\end{aligned}$$

so we have

$$\begin{aligned}\frac{2}{\rho u_\infty^2}(P_\infty - P_0) = &-4\pi\int_0^\infty \frac{\partial u_r}{\partial t}e^{2\pi\xi}d\xi - 1 - 2\int_0^\infty u_\theta\frac{\partial u_r}{\partial\eta}d\xi \\ &+4\pi\int_0^\infty u_\theta^2 d\xi - \left[\frac{4}{Re}\frac{a}{u_\infty}\int_0^\infty \frac{\partial\Omega}{\partial\eta}d\xi\right]_{(a=1,u_\infty=1)}.\end{aligned} \tag{2.17}$$

Substituting Equations (2.16) and (2.17) into Equation (2.13) gives

$$C_p^\theta = 1 + \frac{4}{Re}\int_0^\eta \frac{\partial \Omega}{\partial \xi} d\eta + 4\pi N \int_0^\eta F_{l\theta} d\eta + 4\pi \int_0^\infty \frac{\partial u_r}{\partial t} e^{2\pi\xi} d\xi$$
$$+2\int_0^\infty u_\theta \frac{\partial u_r}{\partial \eta} d\xi - 4\pi \int_0^\infty u_\theta^2 d\xi + \frac{4}{Re}\int_0^\infty \frac{\partial \Omega}{\partial \eta} d\xi \qquad (2.18)$$

2.3 Force Coefficient

The solid cylinder experiences a net force due to the action of the fluid. The total force $\vec{F}_t$ acting on the body is opposite to the force on the fluid and is obtained by integrating the shear stress and pressure along the body surface.

$$\vec{F}_t = \int\int_A \vec{p}\, dA + \int\int_A \vec{\tau}_w\, dA$$

Figure 2.3 shows the force acting on an element of surface of the circular cylinder. The $x-$ component of the total force, $\vec{F}_t$, or drag F_{tx}, consists of skin friction drag and the pressure drag,$(F_{\tau x}, F_{px})$. The friction drag, $F_{\tau x}$, corresponds to the wall shear stress along the cylinder surface, while the pressure drag F_{px} can be obtained from the pressure along the cylinder surface.

The total drag can be expressed as

$$\begin{aligned} F_{tx} &= F_{px} + F_{\tau x} \\ &= \int_0^{2\pi} rP cos\theta\, d\theta + \int_0^{2\pi} r\tau_{r\theta} sin\theta\, d\theta \end{aligned} \qquad (2.19)$$

Similarly, the total lift's expression is

$$\begin{aligned} F_{ty} &= F_{py} + F_{\tau y} \\ &= -\int_0^{2\pi} rP sin\theta\, d\theta + \int_0^{2\pi} r\tau_{r\theta} cos\theta\, d\theta \end{aligned} \qquad (2.20)$$

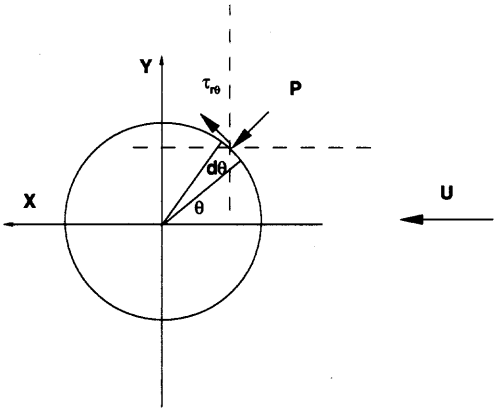

Figure 2.3 Force acting on an element of surface of the cylinder

Using Equation (2.14), the right hand-side of Equation (2.19) can be written as

$$\begin{aligned} F_{px} &= \int_0^{2\pi} rP cos\theta \, d\theta \\ &= -\int_0^{2\pi} \frac{\partial P}{\partial \theta} sin\theta \, d\theta \\ &= -\mu \int_0^{2\pi} \frac{\partial \Omega}{\partial r} sin\theta \, d\theta - \int_0^{2\pi} F_{l\theta} \, d\theta \end{aligned} \tag{2.21}$$

while the shear stress on the surface of the cylinder is expressed as follows.

$$\begin{aligned} \tau_{r\theta} &= \mu[r\frac{\partial}{\partial r}(\frac{u_\theta}{r}) + \frac{1}{r}\frac{\partial u_r}{\partial \theta}] \\ &= \mu \frac{\partial u_\theta}{\partial r} \\ &= \mu\Omega \end{aligned} \tag{2.22}$$

Substitution of Equations (2.21) and (2.22) into Equation (2.19) gives

$$F_{tx} = -\mu \int_0^{2\pi} \frac{\partial \Omega}{\partial r} sin\theta \, d\theta - \int_0^{2\pi} F_{l\theta} sin\theta \, d\theta + \mu \int_0^{2\pi} \Omega sin\theta \, d\theta$$

The dimensionless total drag and lift - or drag and lift coefficients - are defined as

$$\begin{aligned} C_d &= \frac{F_{tx}}{\frac{1}{2}\rho u_\infty^2 d} \\ C_l &= \frac{F_{ty}}{\frac{1}{2}\rho u_\infty^2 d} \end{aligned}$$

where a is the radius of the cylinder.

$$\begin{aligned} C_d &= \frac{F_{px} + F_{\tau x}}{\frac{1}{2}\rho u_\infty^2 d} \\ &= C_{pd} + C_{fd} \\ &= -\frac{\mu}{\frac{1}{2}\rho u_\infty^2 d}\int_0^{2\pi} \frac{\partial \Omega}{\partial r} sin\theta \, d\theta - \frac{\sigma B_0^2}{\frac{1}{2}\rho u_\infty d}\int_0^{2\pi} F_\theta sin\theta d\theta + \frac{\mu}{\frac{1}{2}\rho u_\infty^2 d}\int_0^{2\pi} \Omega sin\theta \, d\theta \\ &= \frac{2}{Re}\int_0^1 (2\pi\Omega - \frac{\partial \Omega}{\partial \xi}) sin(2\pi\eta) \, d\eta - 2\pi N \int_0^1 F_\theta sin(2\pi\eta) \, d\eta \end{aligned} \tag{2.23}$$

where C_{pd}, C_{fd} are the pressure drag and friction drag coefficients.

Using a similar procedure, the total lift coefficient can be written as

$$\begin{aligned} C_l &= \frac{F_{py} + F_{\tau y}}{\frac{1}{2}\rho u_\infty^2 d} \\ &= C_{pl} + C_{fl} \\ &= \frac{2}{Re}\int_0^1 (2\pi\Omega - \frac{\partial \Omega}{\partial \xi}) cos(2\pi\eta) \, d\eta - 2\pi N \int_0^1 F_\theta cos(2\pi\eta) \, d\eta \end{aligned} \tag{2.24}$$

CHAPTER 3

NUMERICAL RESULTS FOR OPEN LOOP CONTROL

In this chapter, numerical results for open loop control at the Reynolds number value $Re = 200$ are presented and discussed. The actuators (exerting Lorentz forces) are distributed either on the entire surface of the cylinder or on smaller portions of the surface during the entire computational time. When the Lorentz force acts on the entire cylinder surface, we consider the case where the force is symmetric, as well as the case where the force is antisymmetric. For all computer runs reported in this thesis, the computational time step is $\triangle t = 0.005$. The interaction parameter values in Section 3.1 are chosen in order to allow comparison with the results of Weier *et al.* (1998).

3.1 Lorentz Force on all Cylinder Surface

Our computations performed for different values of the interaction parameter N show that the results are in excellent agreement with those of Weier *at al.* (1998). Figure 3.1 shows a sequence of instantaneous computed streamlines for $N = 0, 2, 5, 50$. The isolines of the streamfunction (i.e. streamlines) have equal values for all presented figures. At zero interaction parameter, $N = 0$, corresponding to the case where the Lorentz force is turned off, the flow is unsteady and shows the characteristic features of the Karman vortex street. For a small Lorentz force, corresponding to an interaction parameter value of $N = 2$, one observes an interesting modification of the flow. Although the flow is still unsteady, the flow separation region is greatly diminished. Behind the cylinder, a region with two relatively small recirculation bubbles forms. Figures 3.1.c and 3.1.d show that a further increase of the interaction

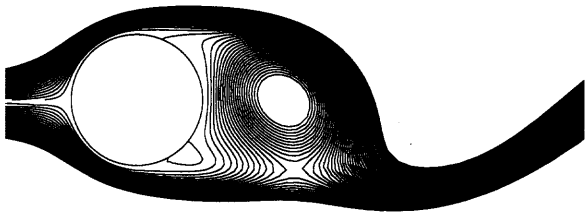

a) N=0

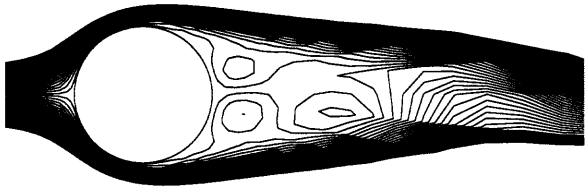

b) N=2

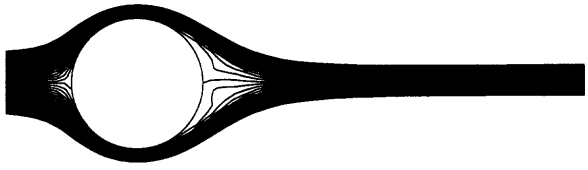

c) N=5

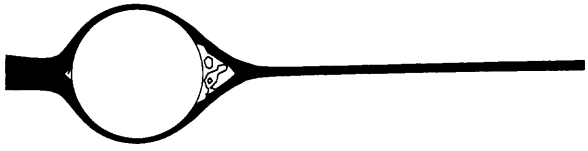

d) N=50

Figure 3.1 Streamlines of the flow at Reynolds number $Re = 200$ with various interaction parameters

parameter N fully suppresses separation and stabilizes the flow. As the interaction parameter, N, increases, streamlines get closer to each other and the fluid gets more and more accelerated by the Lorentz force. The higher the magnitude of force, the stronger the accelerating effect. Figures 3.1.c,d show the accelerating effect on the fluid not only behind the cylinder, but also in front of the cylinder. On the rear face of the cylinder, the accelerated fluid separates from the surface of the cylinder forming two jets (symmetric with respect ot the center line) which meet downstream, e.g. $N = 50$, the two jets meet close to the cylinder, at about 0.5 diameter behind the rear stagnation point. In between the two jets, one can observe a recirculation zone consisting of several small vortices. Our numerical results, in excellent agreement with those of Weier *et al* (1998), show that a Lorentz force tangential to the surface of the circular cylinder is capable of altering the cylinder boundary layer and preventing boundary layer separation.

The vorticity and pressure distributions on the cylinder surface at different interaction parameter values are shown in Figures 3.2 and 3.3. The angle θ is defined from the front to the rear stagnation point. From the vorticity distribution in Figure 3.2, one can see that an increase in the interaction parameter (and therefore in the Lorentz force) leads to an increase in vorticity. Higher values of the Lorentz force result in a steeper gradient of the velocity profile at the wall, thus causing higher vorticity values. The zero vorticity point corresponding to the separation point on the cylinder is lifted away from the horizontal axis, thus making separation disappear all together.

As the Lorentz force increases, the pressure distribution reaches lower values due to the accelerated fluid, although close to the rear stagnation point the pressure increases due to the reduction of the recirculation region. Figure 3.3 shows that at $N = 5$, the pressure value at the rear stagnation point is even larger than the value

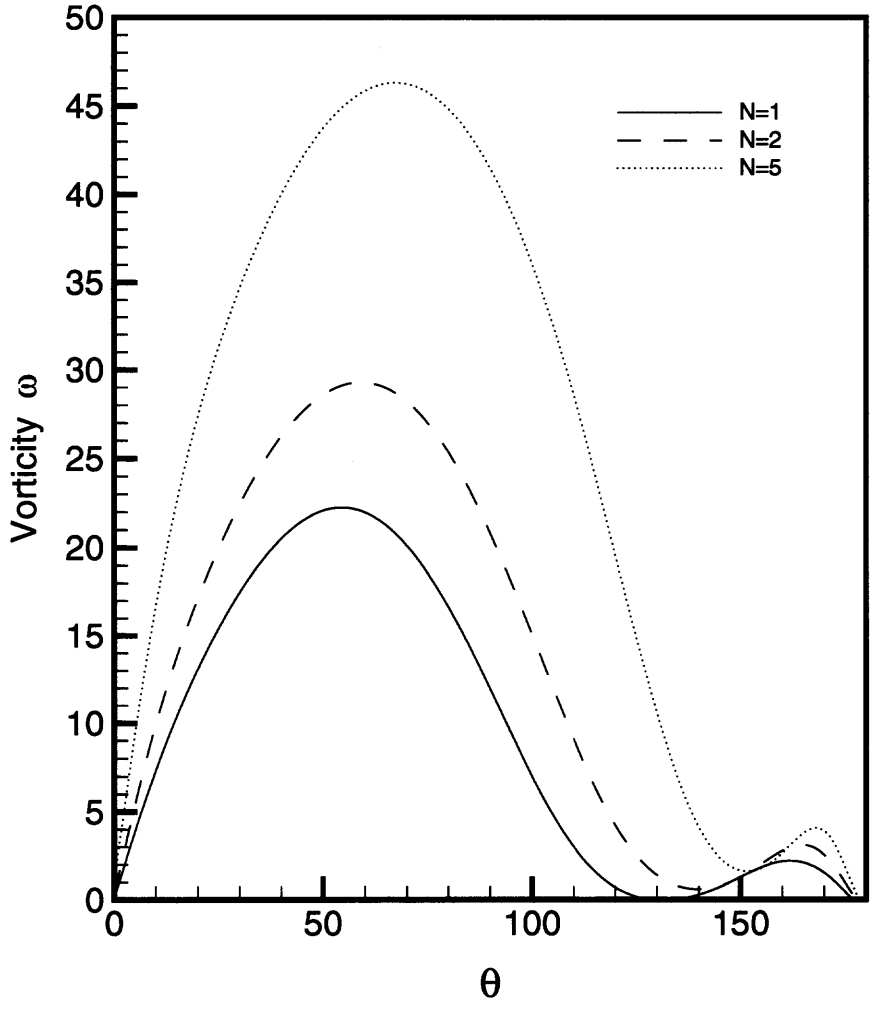

Figure 3.2 Vorticity distribution along the surface of the cylinder at various interaction parameter values

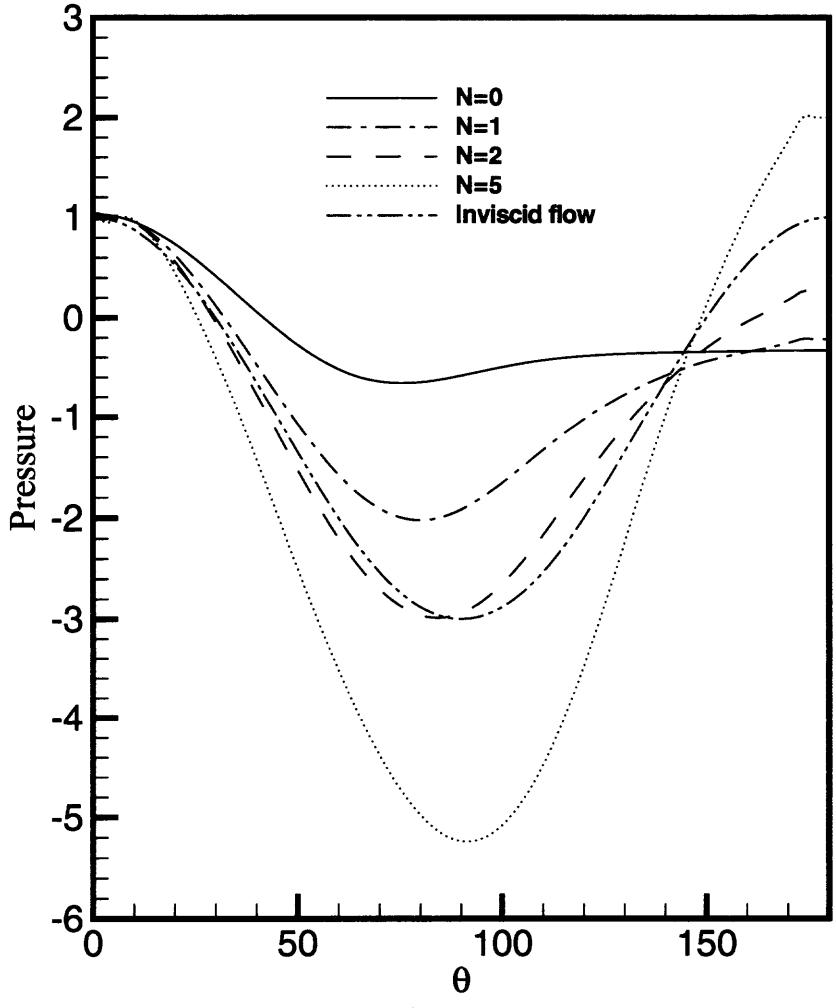

Figure 3.3 Pressure distribution along the surface of the cylinder at various interaction parameter values

of the front stagnation point. This implies a net force opposed to the mean flow direction due to the pressure difference between front and rear stagnation points.

Figure 3.4 shows the time history of the pressure, friction, and total drag coefficients at different values of the interaction parameter at Reynolds number $Re = 200$. These results, in agreement with those reported by Weier *et al* (1998), summarize some of the flow features we found in previous diagrams. More specifically, pressure drag C_{pd} decreases with increasing interaction parameter because of separation suppression. At sufficiently large values of the Lorentz force, a jet in the vicinity of the rear stagnation point increases pressure there. When the force is sufficiently large to create pressure values which are larger in the rear than in the front of the cylinder, the pressure drag becomes negative, leading to thrust on the cylinder. In contrast, friction drag C_{fd} increases with increasing interaction parameter. This is due to the increased wall friction resulting from the steeper velocity gradient caused by the accelerated fluid at the wall. The total drag coefficient C_d, equal to the sum of the pressure C_{pd} and friction drag coefficient C_{fd}, is always smaller than the value it had when the Lorentz force was turned off.

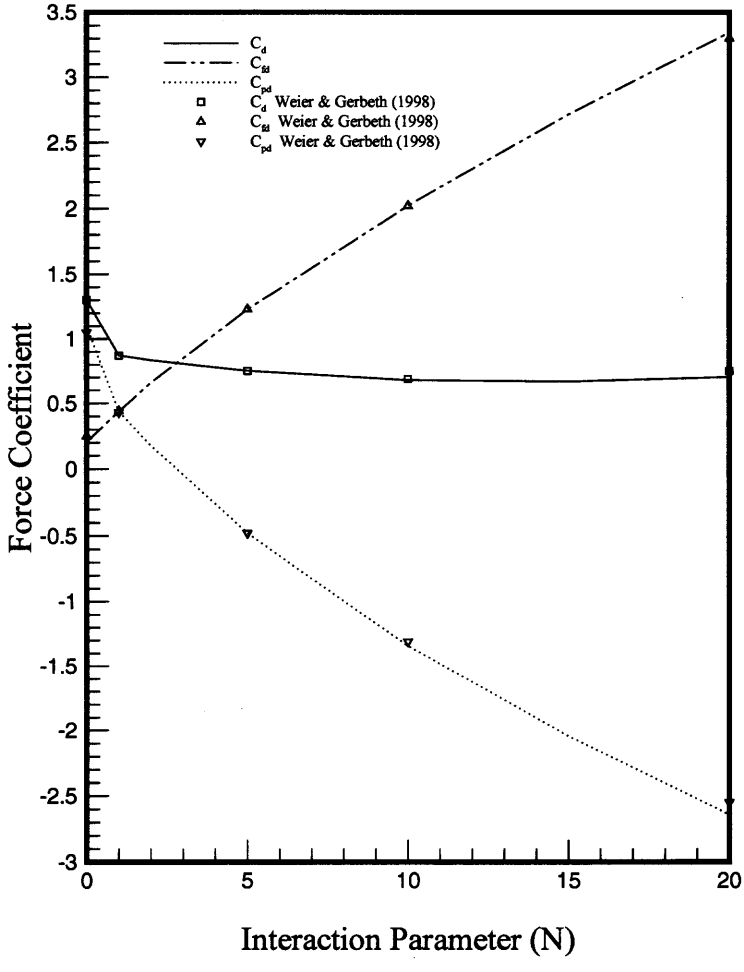

Figure 3.4 Time history of the pressure, friction and total drag coefficient at various interaction parameters

3.2 Localized Lorentz Force

Results shown in the above section are obtained from the actuation over the entire cylinder surface. In terms of practical implementation, local actuations may save energy while being as efficient. When localized forces are used, their precise location is a critical factor in the effectiveness of suppressing vortex shedding. Park *et al* (1994) found that if the actuator was located too far from the separation point on the surface of the cylinder, suppression of vortex shedding could not be obtained. In the uncontrolled flow at $Re = 200$, separation takes place on the cylinder surface at about $\pm 110°$ from the front stagnation point. Therefore, the location of our actuators has been selected at beginning slightly upstream of the separation point, that is at $\pm 95°$ from the stagnation point. The Lorenz force in Equation (2.8) can then be written as

$$\vec{F} = e^{-\alpha(r-1)} g(\theta) \vec{e_\theta} \qquad with \quad g(\theta) = \begin{cases} 1 & 95° \leq \theta \leq 175° \\ -1 & 185° \leq \theta \leq 265° \\ 0 & \text{elsewhere} \end{cases} \tag{3.1}$$

Using the same numerical method as described in Chapter 2, we obtain the following results. Figures 3.5 and 3.6 show the instantaneous streamlines for the interaction parameter values $N = 0, 1, 2, 3, 5, 7, 10, 15$ and the corresponding vorticity contours, respectively. Here as before, the streamlines have equal values for all presented figures. As we compare the results with those of Figure 3.1 (see Section 3.1), we see that the Lorentz force applied to a portion of the cylinder surface only is as efficient as the Lorentz force applied on the whole surface. Separation is fully suppressed at the interaction parameter value $N = 3$. Once again, the acceleration of the fluid on the rear half of cylinder surface takes place, which can be observed from the narrowing of the streamlines behind the cylinder. Further increase of the

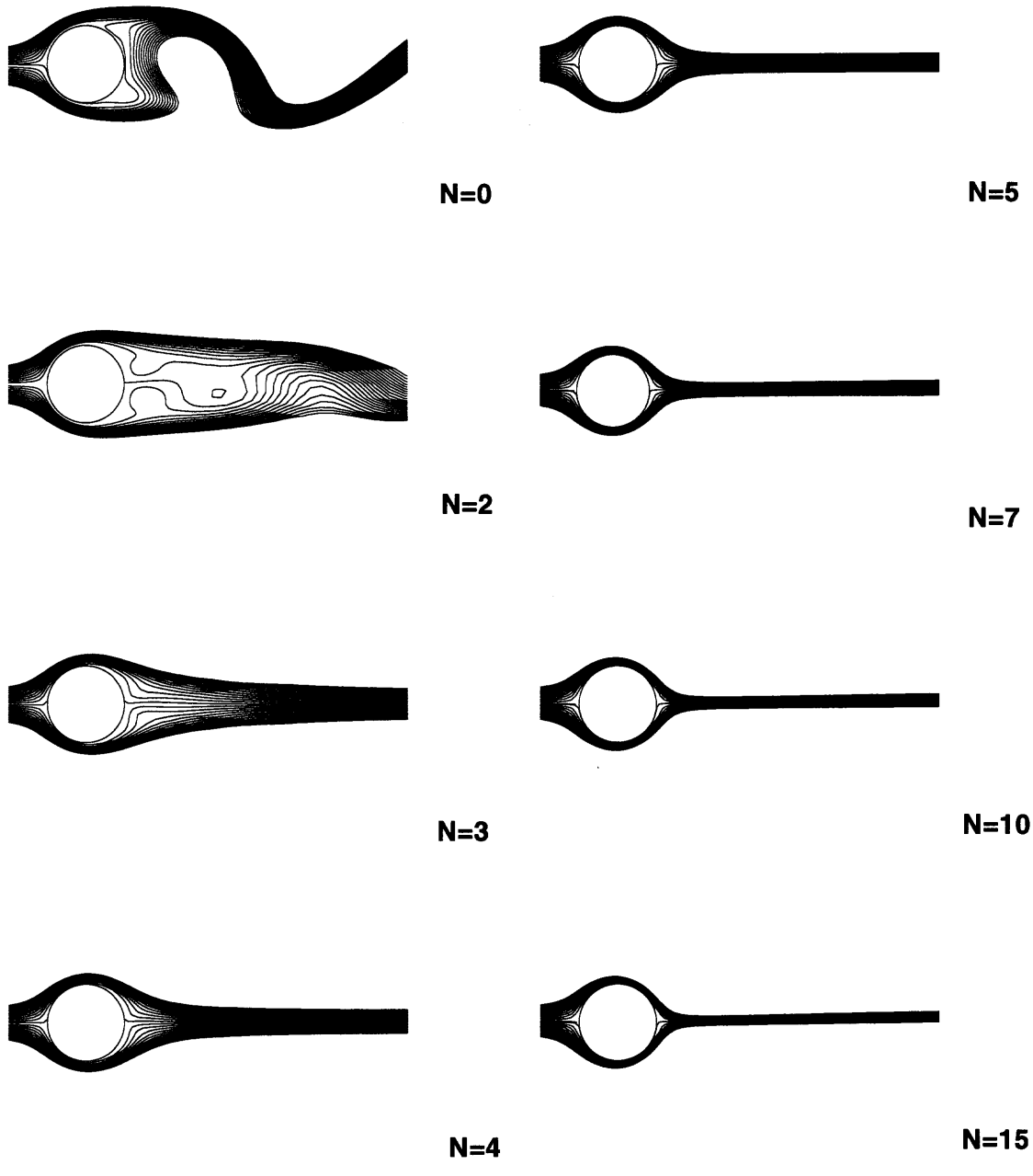

Figure 3.5 Instantaneous streamlines for the interaction parameter values $N = 0, 2, 3, 4, 5, 7, 10, 15$.

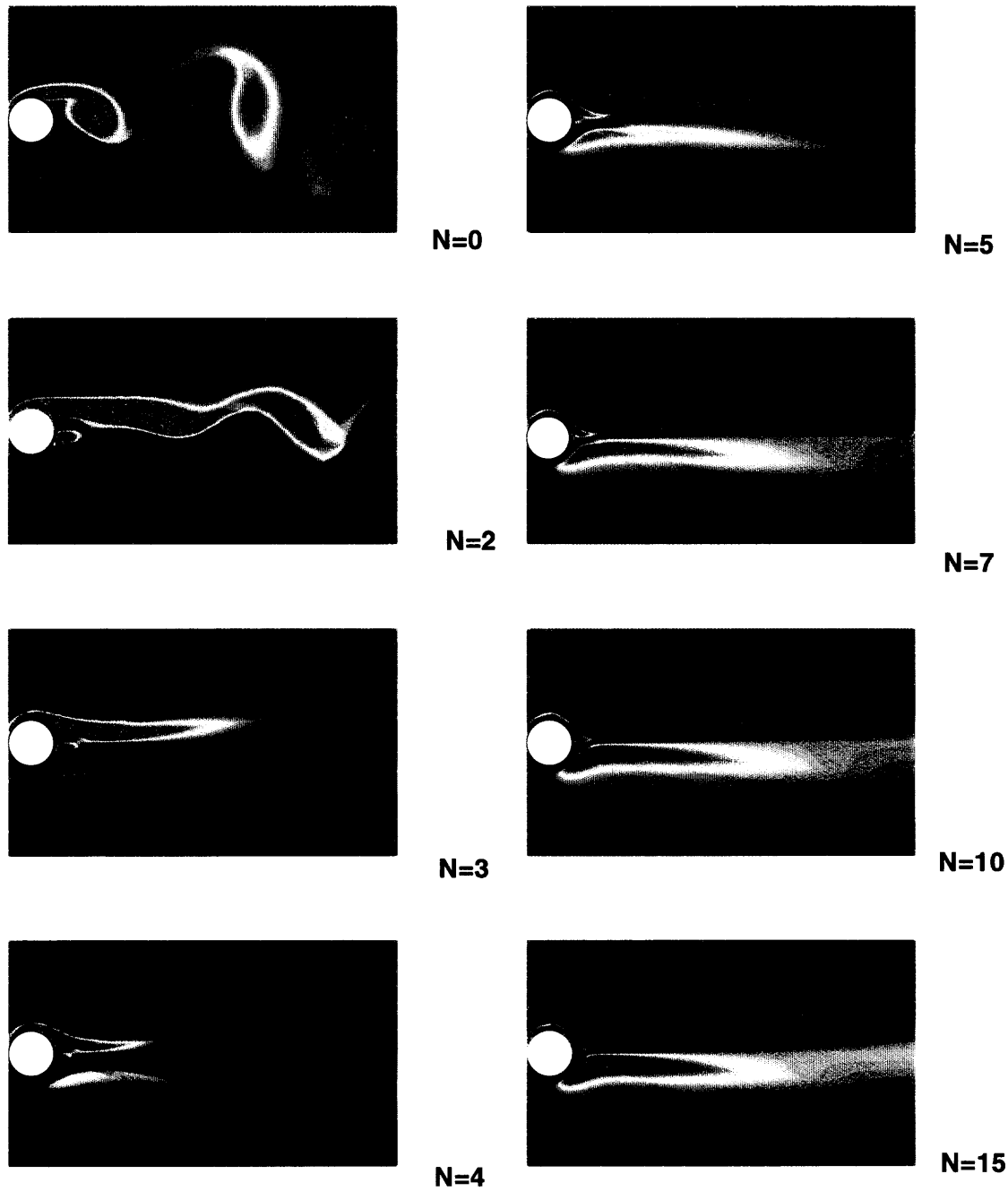

Figure 3.6 Instantaneous vorticity contours at the interaction parameter values $N = 0, 2, 3, 4, 5, 7, 10, 15$.

interaction parameter N leads to streamlines closer to each other. On the rear face of the cylinder, the accelerated fluid separates from the cylinder at about 100°, forming two jets (see Figures 3.5 and 3.6). At high interaction parameter values, the Lorentz force acts mainly as a thrust generator.

Figures 3.7 and 3.8 show the vorticity and pressure coefficient distributions on the cylinder surface where θ is defined from the front to the rear stagnation point. It is clear from Figure 3.7 that the increase of surface force leads to an increase in vorticity. The same tendency can be observed in Figure 3.2 although differences occur between these two figures. First, in Figure 3.7, the increase in the amplitude of vorticity with the interation parameter is smaller than the increase of vorticity in Figure 3.2. Second, the highest vorticity point in Figure 3.2 is almost fixed at the cylinder surface, while it moves back toward the rear stagnation point in Figure 3.7. This can be explained as follows. With the increase of the intensity of the Lorentz force applied to a portion of the cylinder surface, the actuation area experiences a higher shear that results in higher vorticity compared to the rest of the cylinder surface.

The pressure over the actuation area decreases with the increase of surface force, while the pressure at the rear stagnation point increases due to the reduction of recirculation region, to the point that when $N = 5$, it actually becomes larger than that of the front stagnation point.

Figure 3.9 displays the time history of the force coefficient with different interaction parameter values. It is clear that as the interaction parameter N increases, the pressure, lift and total drag coefficient decrease, which is consistent with some of the flow features previously found. Pressure drag decreases with the increase of the interaction parameter due to the suppression of flow separation. When the interaction parameter becomes sufficiently high, the pressure at the rear stagnation point

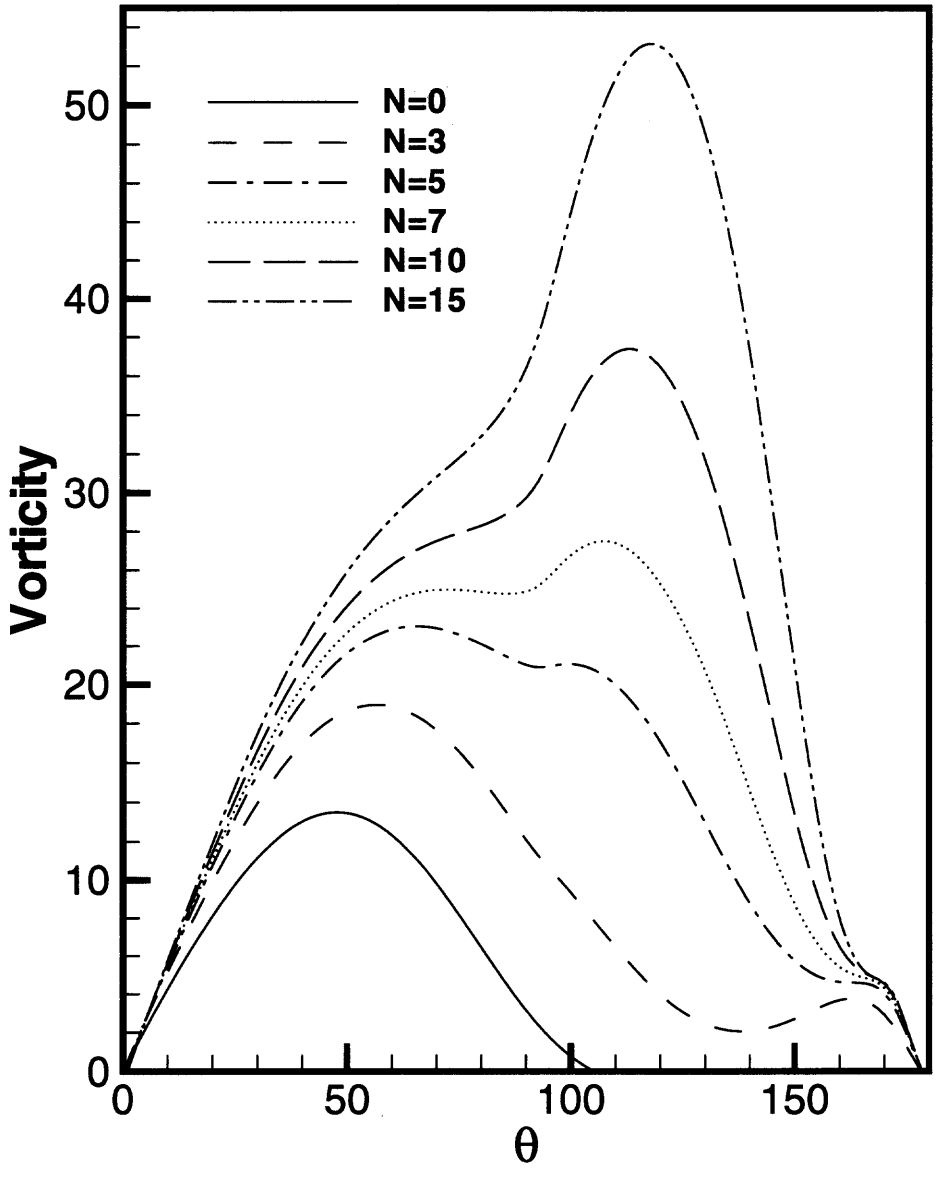

Figure 3.7 Vorticity distribution on the cylinder surface for various interaction parameter values.

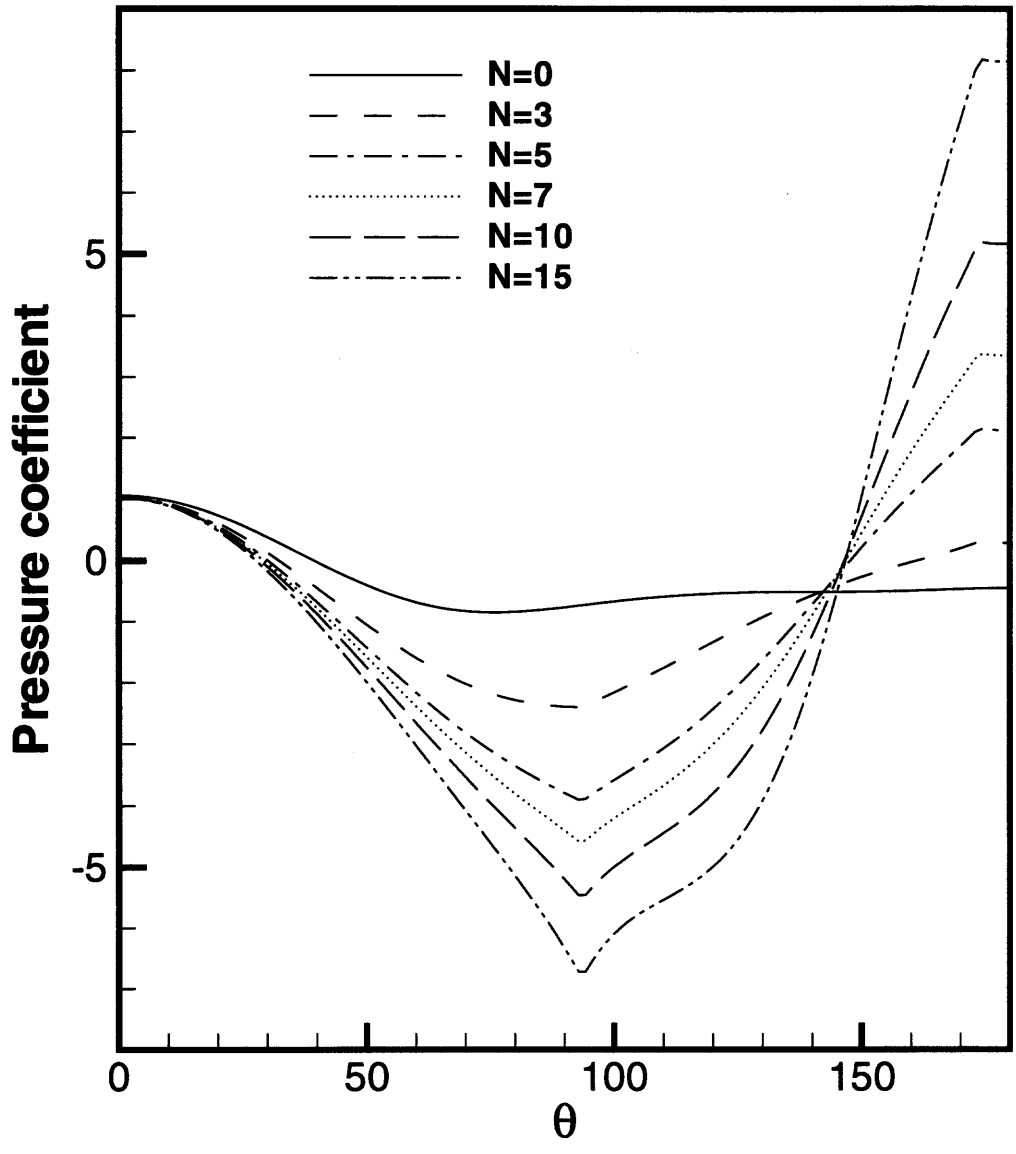

Figure 3.8 Pressure distribution on the cylinder surface for various interaction parameter values.

becomes even higher than at the front stagnation point. Therefore, the pressure drag coefficient becomes negative. On the other hand, the friction drag increases as the interaction parameter increases. The total drag also experiences some discrepancies between Figures 3.9 and 3.4. In the localized Lorentz force, the friction drag increase slower than the pressure drag decreases. This implies that the total drag is always dominated by the effect of the pressure drag and that it indeed decreases. Consequently, the localized force is at least as efficient as the distributed force in reducing the total drag coefficient.

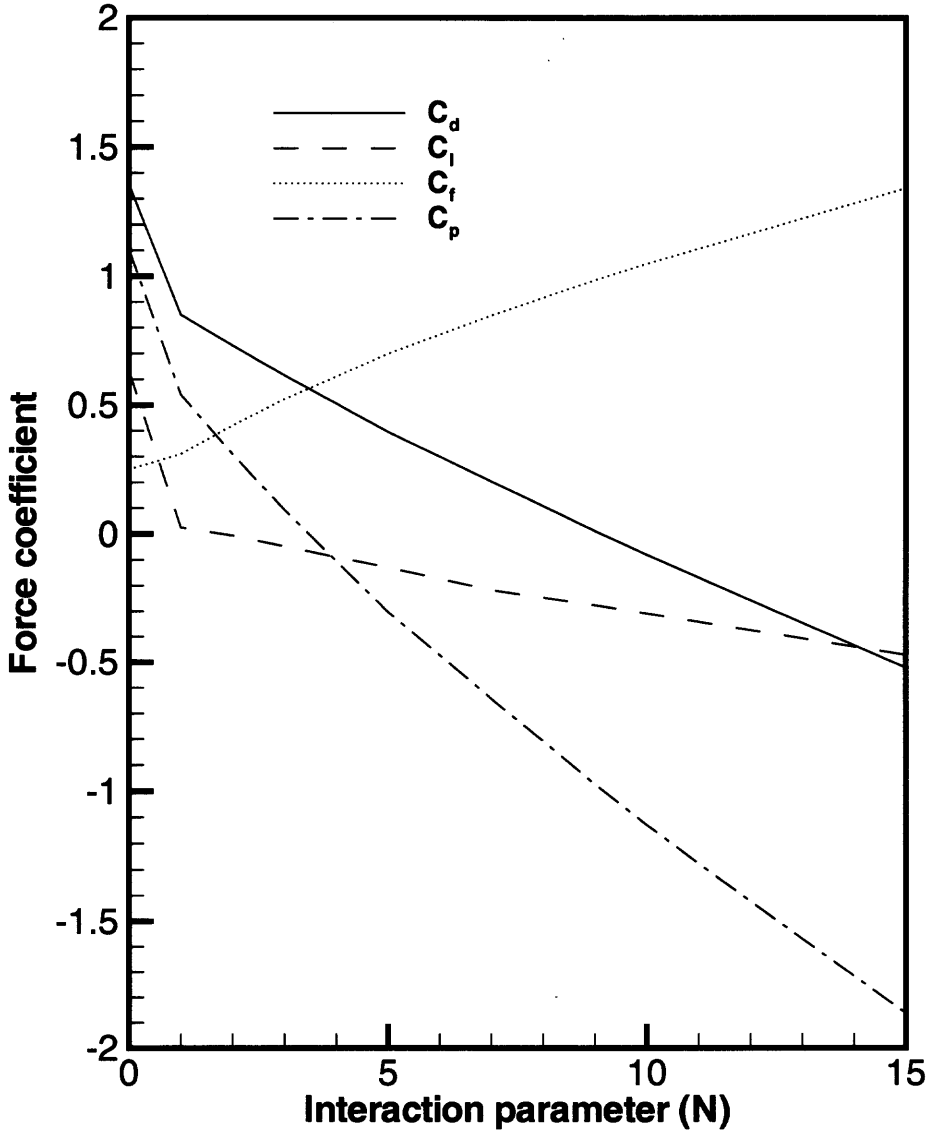

Figure 3.9 Time history of the force coefficient with various interaction parameter values.

3.3 Time Periodic Lorentz Force

In this section, we explore the influence of the time periodic of the Lorentz force onto the efficiency of the flow control technique. The case is first considered where the Lorentz force is symmetric with respect to the centerline (Section 2.1.4), and second the case where the Lorentz force is antisymmetric (Section 2.1.5).

Figures 3.10. 3.11 and 3.12 present the flow characteristics for various values of the interaction parameter ($N = 5, 10, 20$). Figure 3.10 shows the flow streamlines for various interaction parameter and Lorentz force frequency values. It is clear that the flow structure depends on both the magnitude of the Lorentz force and the excitation frequency.

In the symmetric case, the flow consists of a symmetric vortex street when the values of the interaction parameter and force frequency are appropriately chosen ($N = 5, f_e = 0.2$). When the excitation frequency increases, the flow becomes somewhat comparable to the flow past a vibrating cylinder, which vibrates in line with the oncoming flow (Ongoren and Rockwell (1988)).

Figures 3.11 and 3.12 show that when the Lorentz force excitation frequency is close to the Strouhal number frequency ($St = 2af/U_{infty}$, where f denotes the frequency of natural vortex shedding), that is $f_e = 0.2$, the lock-in phenomenon occurs. Figure 3.11 shows the time history of the drag coefficient at various values of the Lorentz force frequency and interaction parameter. The oscillation frequency of the drag coefficient is dominated by the Lorentz force frequency, and the amplitude of the drag increases as the force frequency and interaction parameter increase. At sufficiently large values of the Lorentz force frequency, the drag exhibits two different frequencies, one corresponding to the Lorentz force frequency, and the other one being the natural vortex shedding frequency.

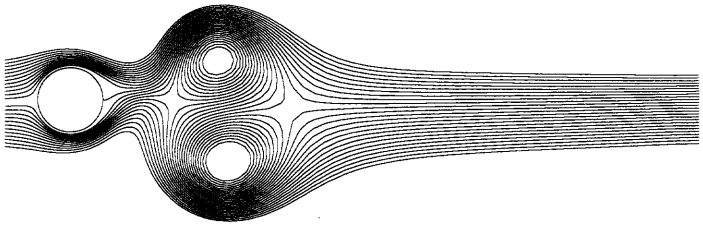

f_e=0.05

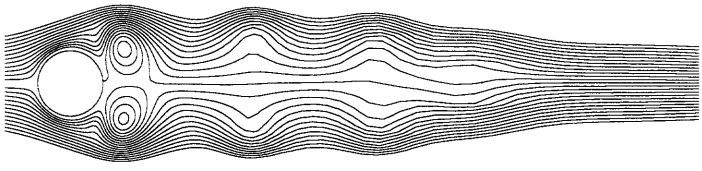

f_e=0.2

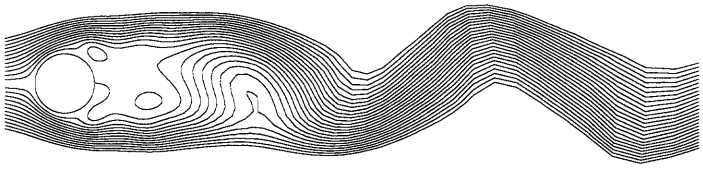

f_e=0.4

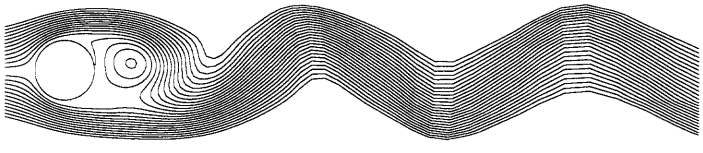

f_e=0.8

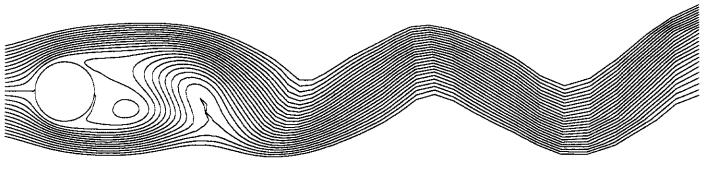

f_e=1.6

(a) N=5

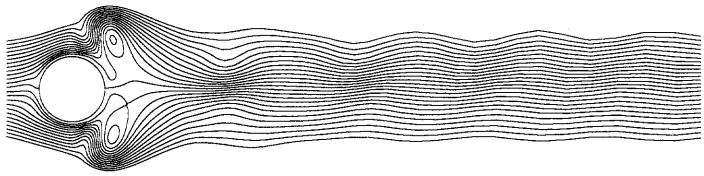

f_e=0.2

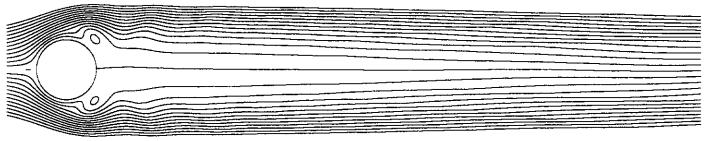

f_e=0.4

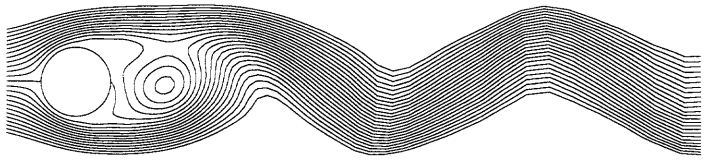

f_e=0.8

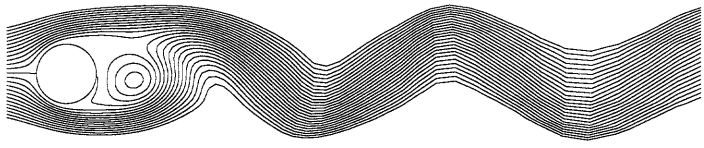

f_e=1.6

(b) N=10

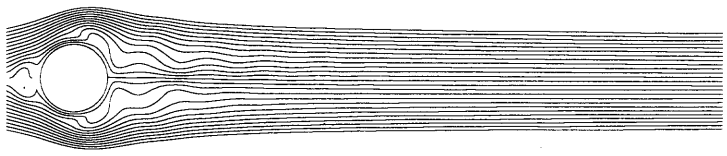

f_e=0.4

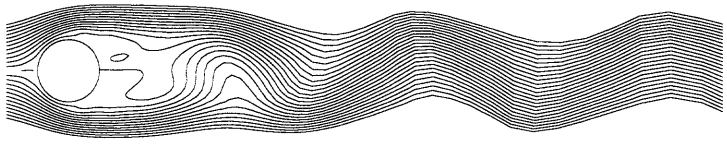

f_e=0.8

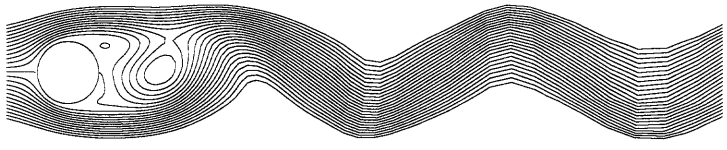

f_e=1.6

(c) N=20

Figure 3.10 Flow streamlines in the case of a symmetric Lorentz force for various values of the interaction parameter and Lorentz force frequency.

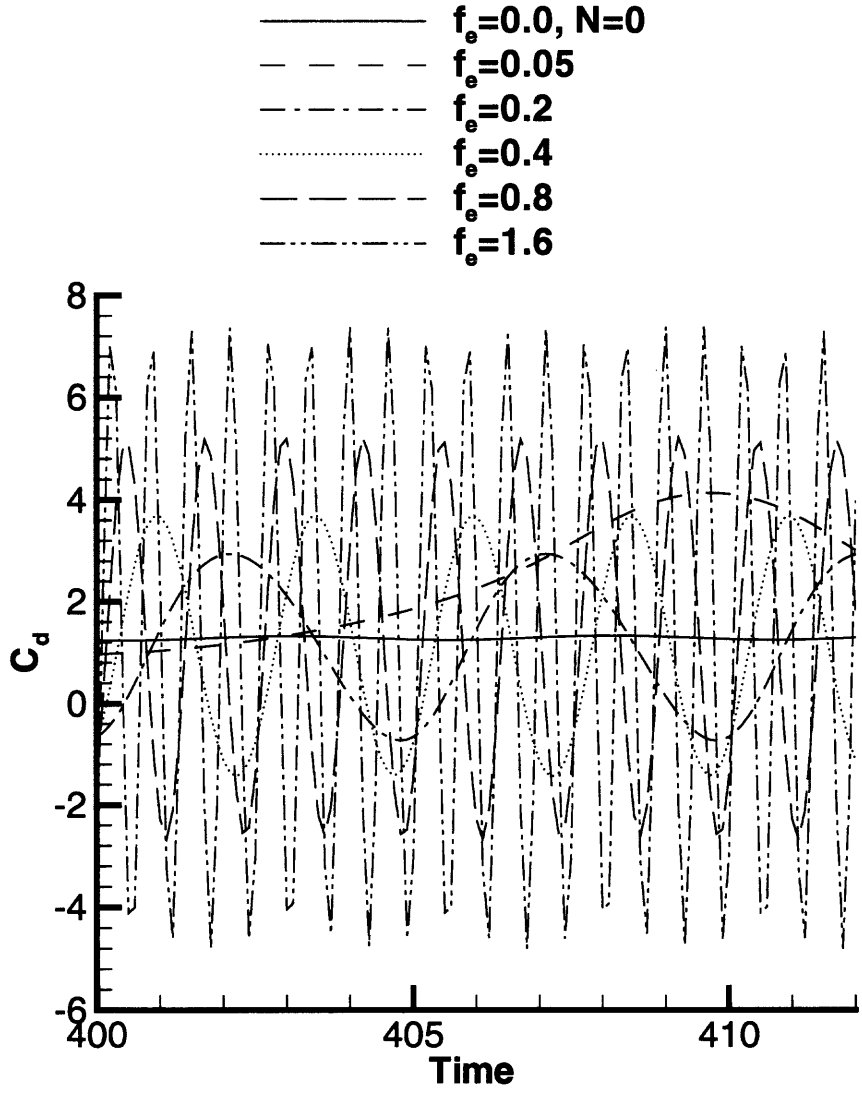
f_e=0.0, N=0
f_e=0.05
f_e=0.2
f_e=0.4
f_e=0.8
f_e=1.6
C_d
8
6
4
2
0
-2
-4
-6
400
405
410
Time

(a) N=5

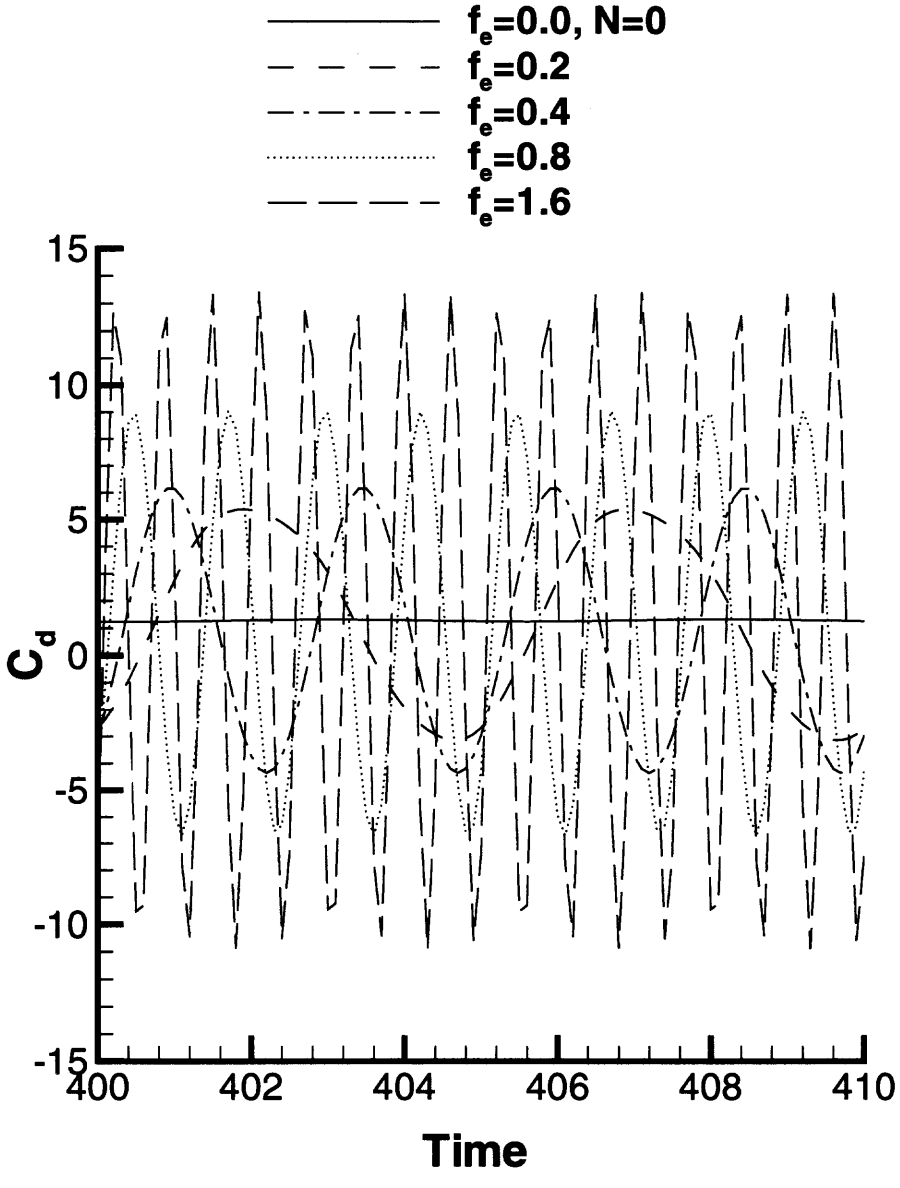
f_e=0.0, N=0
f_e=0.2
f_e=0.4
f_e=0.8
f_e=1.6
15
10
5
0
-5
-10
-15
C_d
400
402
404
406
408
410
Time

(b) N=10

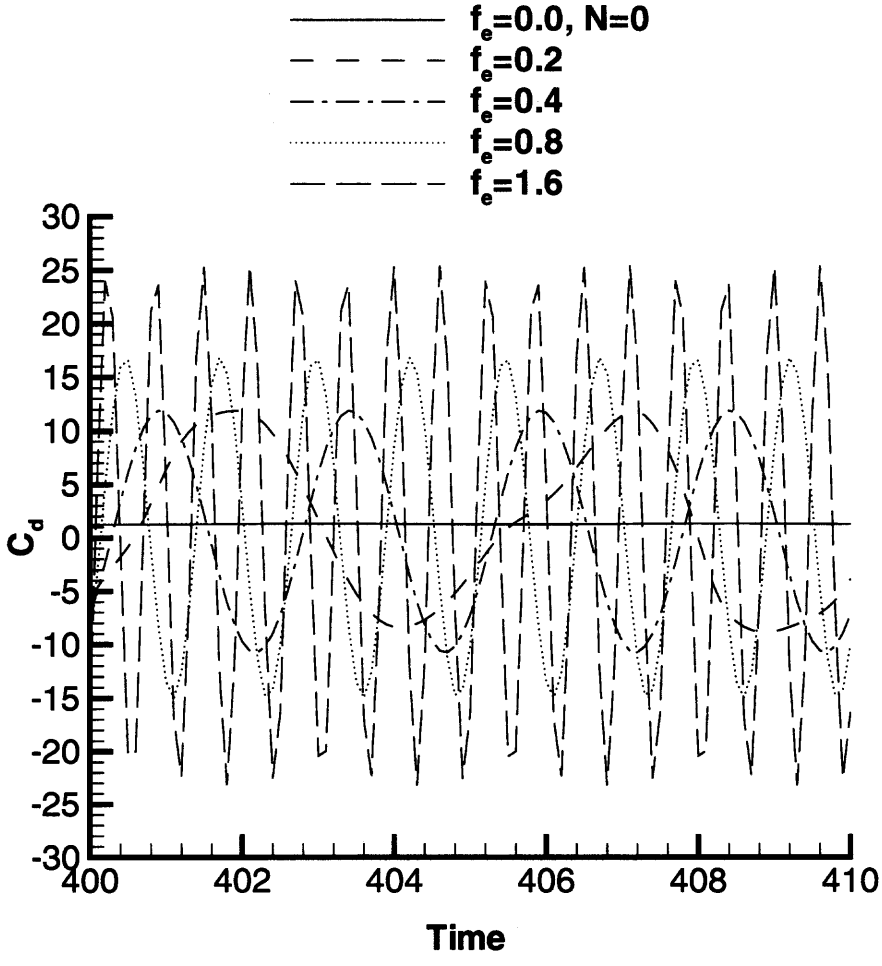

(c) N=20

Figure 3.11 Time history of the drag coefficient for various values of the interaction parameter and force frequency in the case of a symmetric Lorentz force.

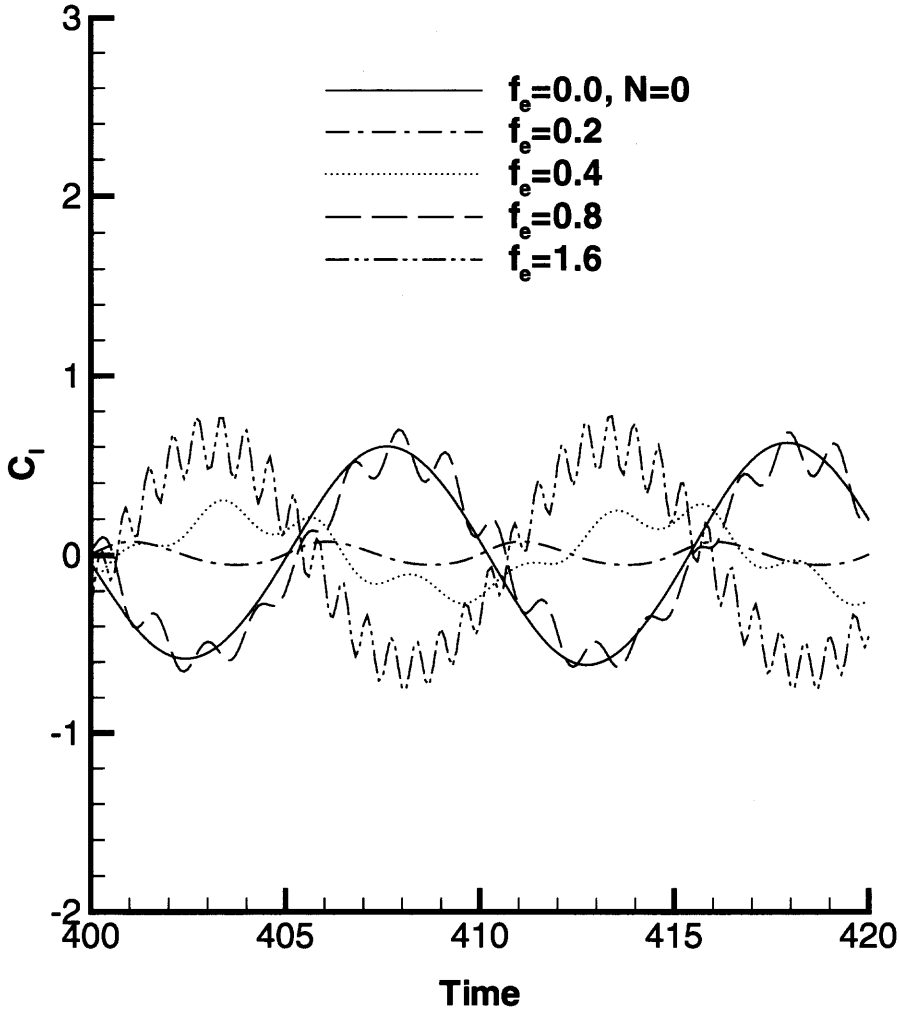

(a) N=5

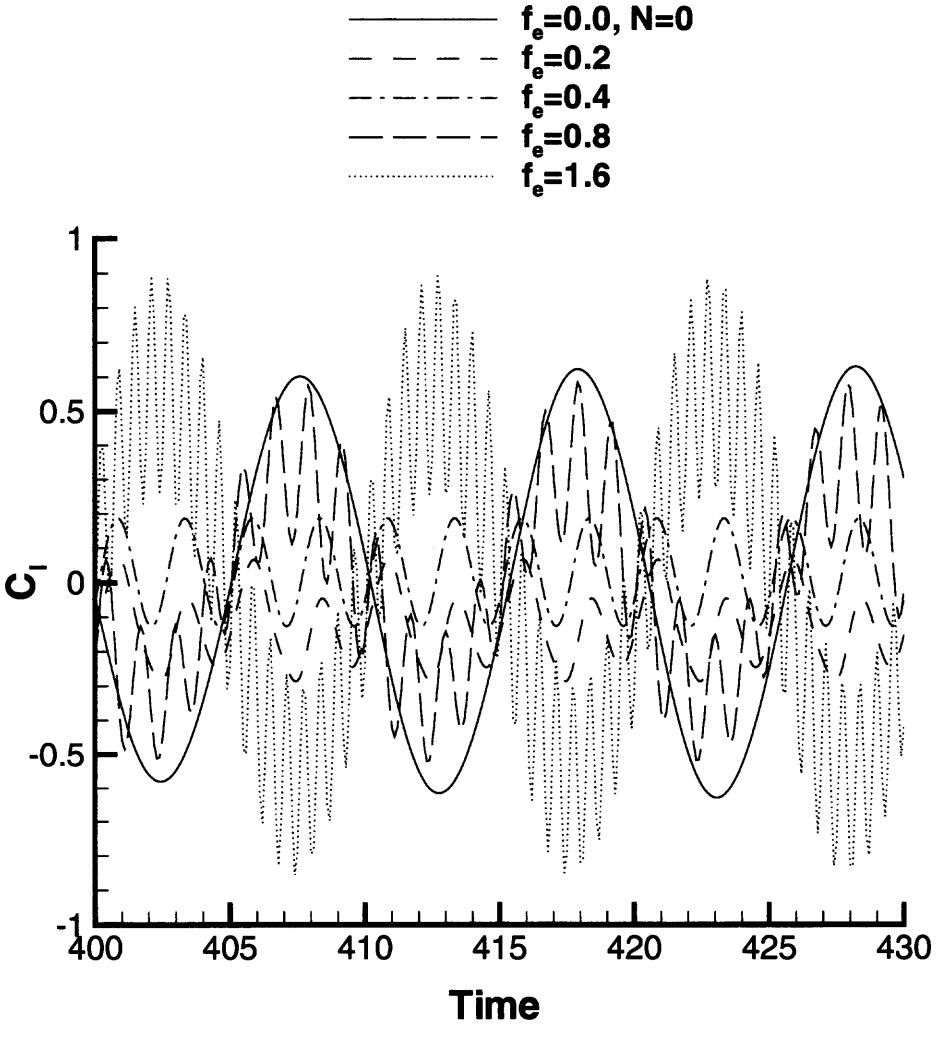
f_e=0.0, N=0
f_e=0.2
f_e=0.4
f_e=0.8
f_e=1.6
1
0.5
0
-0.5
-1
C_l
400
405
410
415
420
425
430
Time

(b) N=10

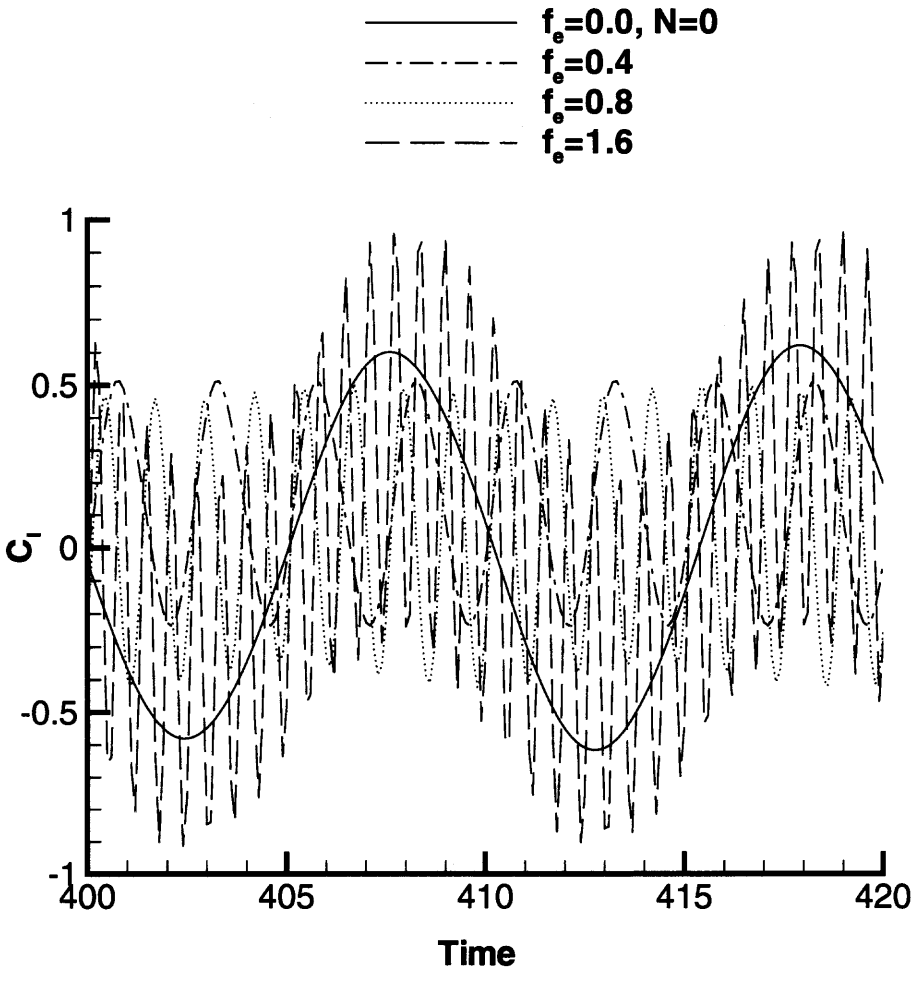

(c) N=20

Figure 3.12 Time history of the lift coefficient for various values of the interaction parameter and Lorentz force frequency in the case of a symmetric Lorentz force.

Figure 3.12 displays the time history of the lift coefficient for various values of the Lorentz force frequency and interaction parameter. Like the drag, the amplitude of the lift coefficient increases with the Lorentz force frequency and its frequency corresponds to that of the drag.

When the Lorentz force is antisymmetric with respect to the centerline, the effect is somewhat different. Figure 3.13 shows the streamlines for various values of the interaction parameter and Lorentz force frequency. One can observe that when the Lorentz force frequency becomes sufficiently large, the flow structure does not change much with the interaction parameter.

Figure 3.14 displays the time history of the drag force for various values of the Lorentz force frequency at certain interaction parameter values. When the Lorentz force frequency is sufficiently large, the drag exhibits two different frequencies, one corresponding to the natural vortex shedding frequency, the other one coinciding with the Lorentz force frequency. In contrast with what happens in the symmetric case, the amplitude of the drag force decreases as the Lorentz force frequency increases. Likewise, Figure 3.15 shows that the amplitude of the lift decreases as the frequency of the Lorentz force increases. Here, again, the oscillation frequency is controlled by the Lorentz force frequency. In particular, the occurrence of the two different frequencies in the lift coefficient is visible even at small interaction parameter values.

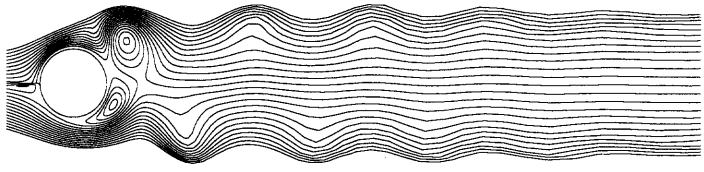

f_e=0.2

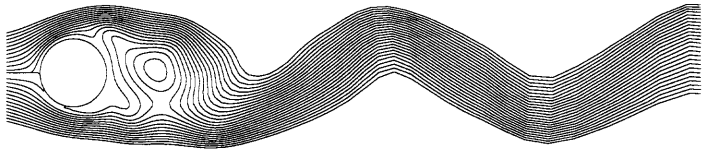

f_e=0.4

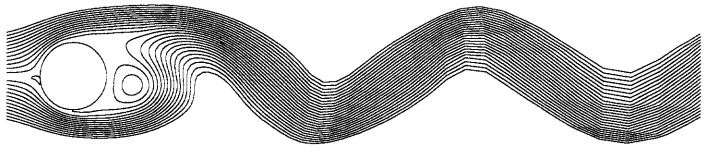

f_e=0.8

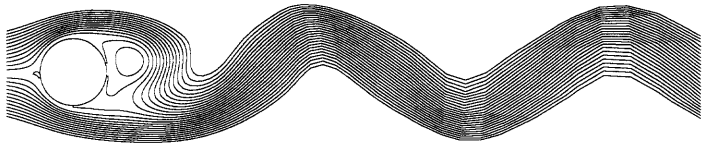

f_e=1.6

(a) N=5

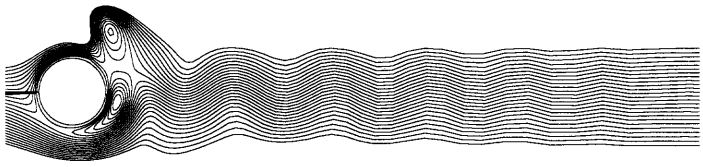

f_e=0.2

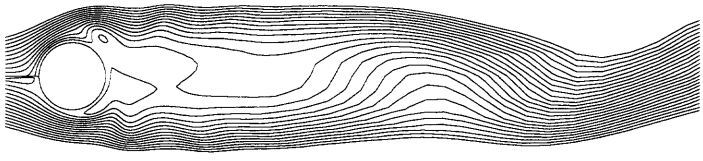

f_e=0.4

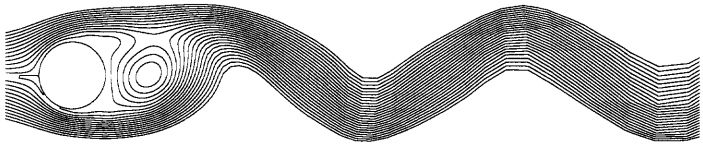

f_e=0.8

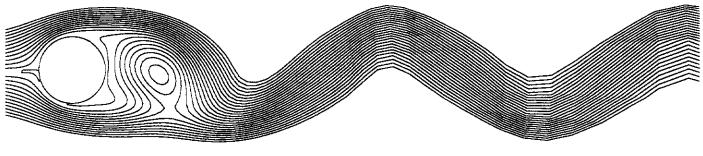

f_e=1.6

(b) N=10

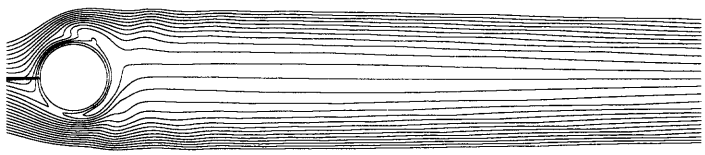

f_e=0.4

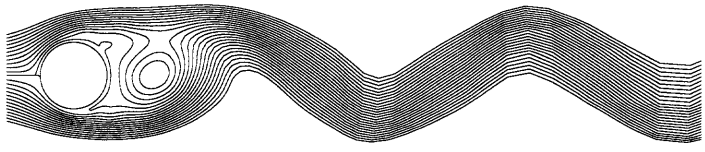

f_e=0.8

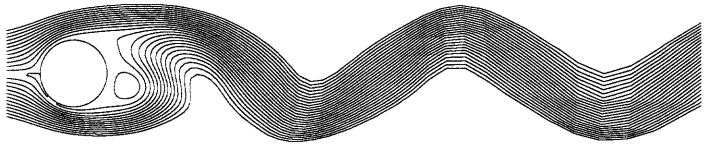

f_e=1.6

(c) N=20

Figure 3.13 Flow streamlines for various values of the interaction parameter and Lorentz force frequency in the case of an antisymmetric Lorentz force.

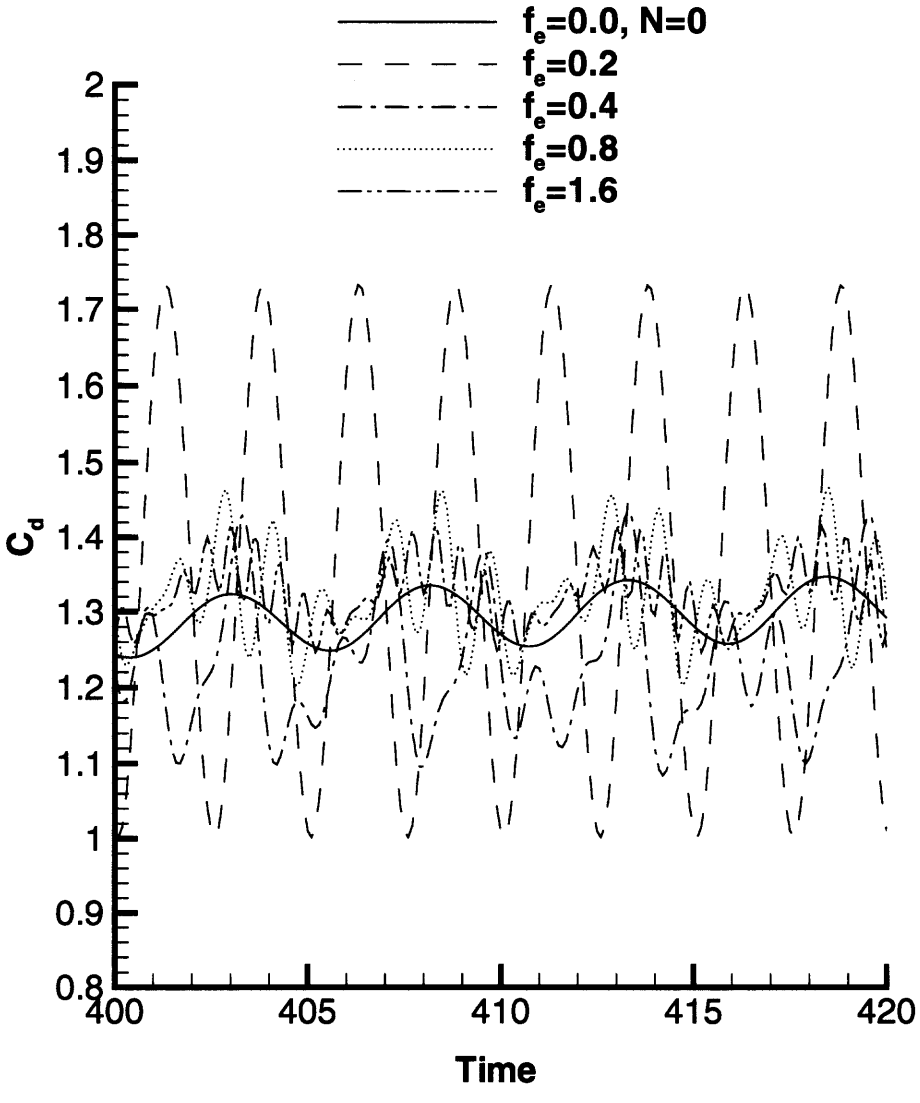
f_e=0.0, N=0
f_e=0.2
f_e=0.4
f_e=0.8
f_e=1.6
C_d
2
1.9
1.8
1.7
1.6
1.5
1.4
1.3
1.2
1.1
1
0.9
0.8
400
405
410
415
420
Time

(a) N=5

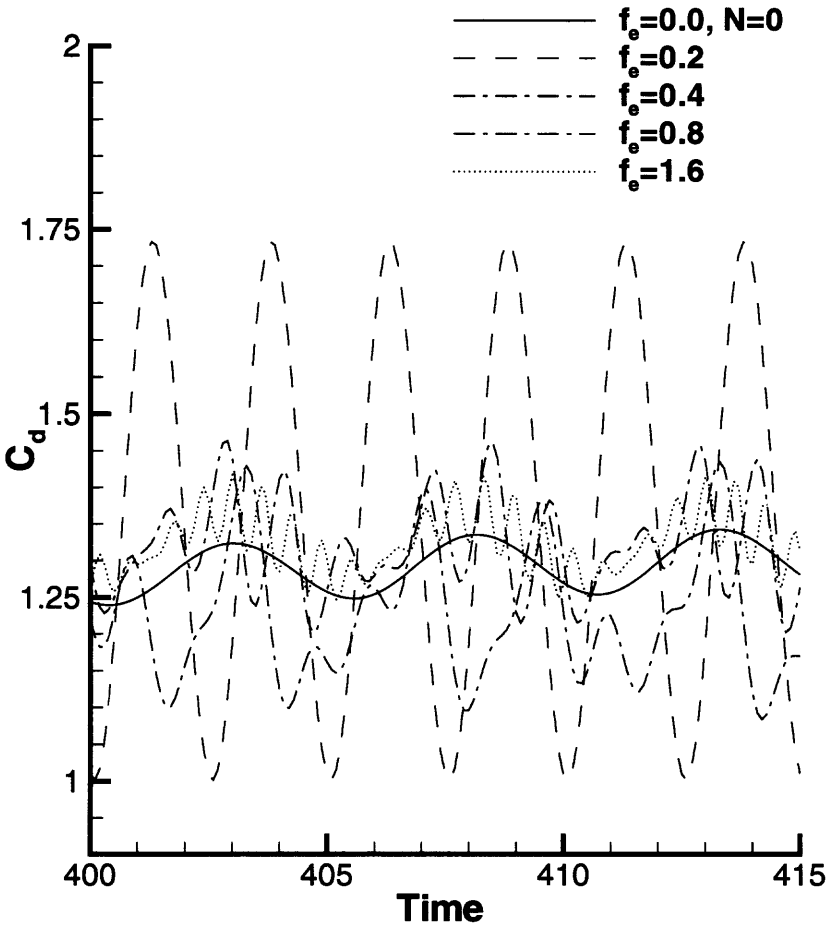
f_e=0.0, N=0
f_e=0.2
f_e=0.4
f_e=0.8
f_e=1.6
2
1.75
1.5
1.25
1
C_d
400
405
410
415
Time

(b) N=10

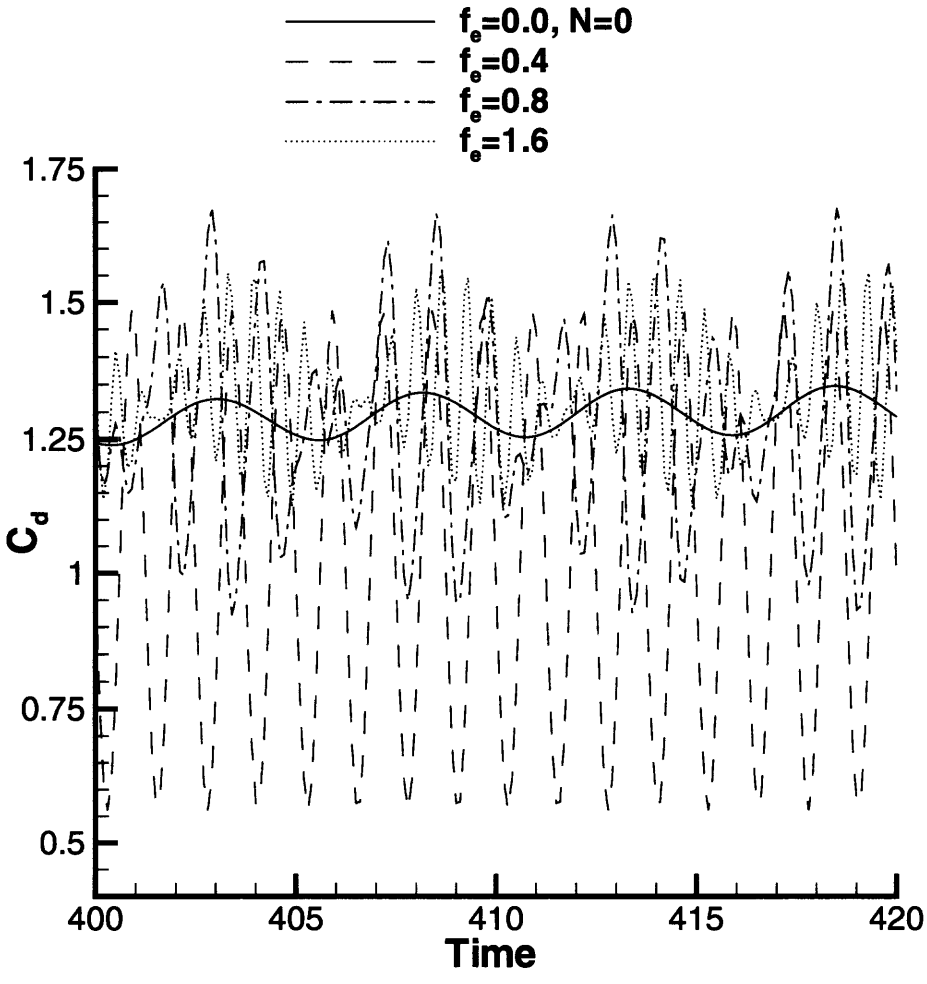

(c) N=20

Figure 3.14 Time history of the drag coefficient for various values of the interaction parameter and force frequency in the case of an antisymmetric Lorentz force.

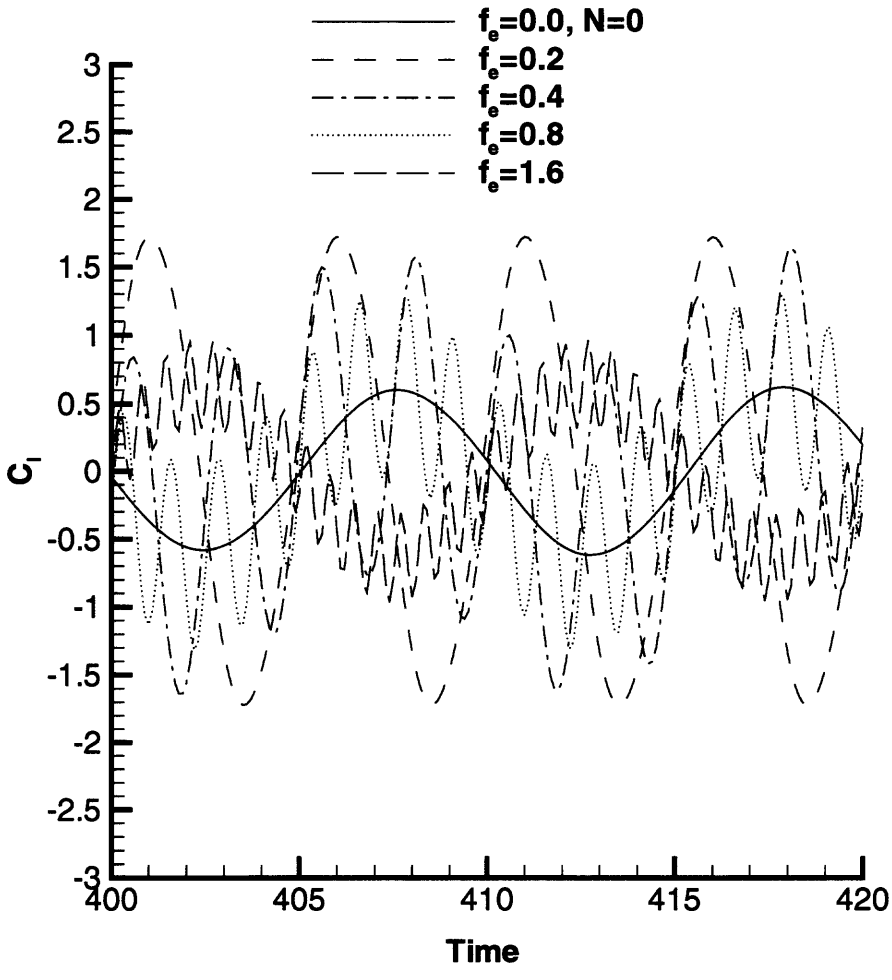
f_e=0.0, N=0
f_e=0.2
f_e=0.4
f_e=0.8
f_e=1.6
C_l
3
2.5
2
1.5
1
0.5
0
-0.5
-1
-1.5
-2
-2.5
-3
400
405
410
415
420
Time

(a) N=5

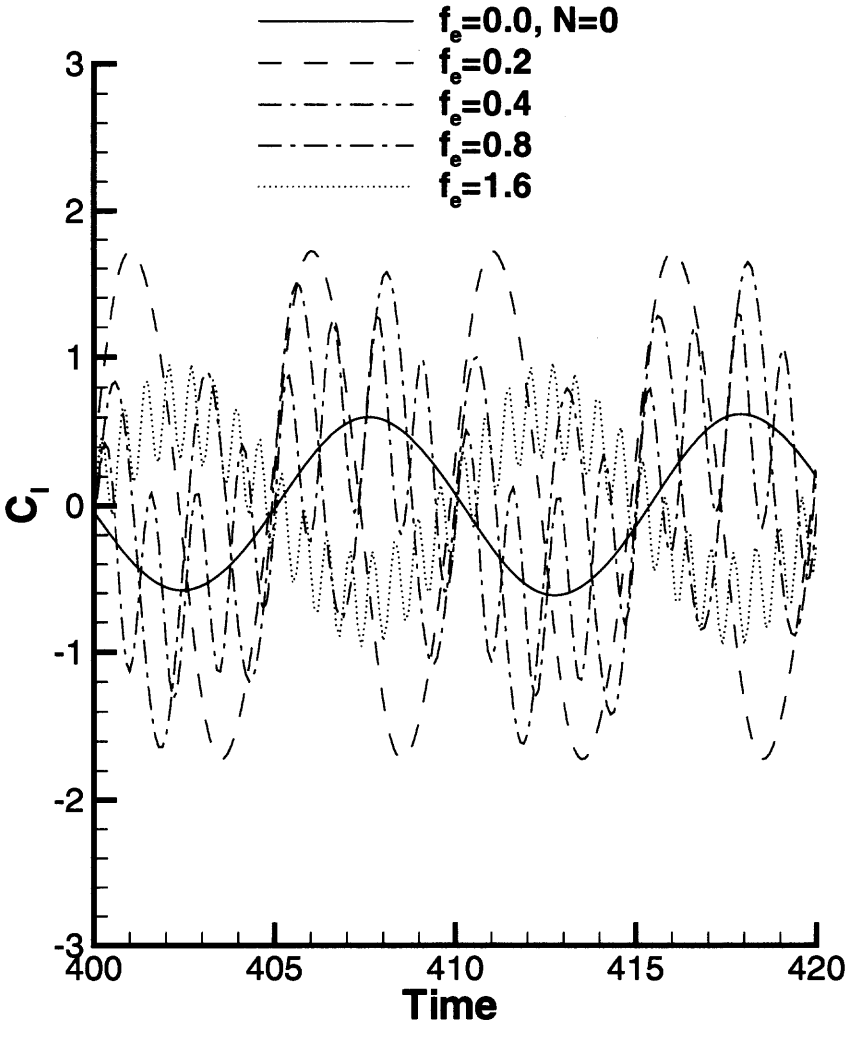
f_e=0.0, N=0
f_e=0.2
f_e=0.4
f_e=0.8
f_e=1.6
C_l
3
2
1
0
-1
-2
-3
400
405
410
415
420
Time

(b) N=10

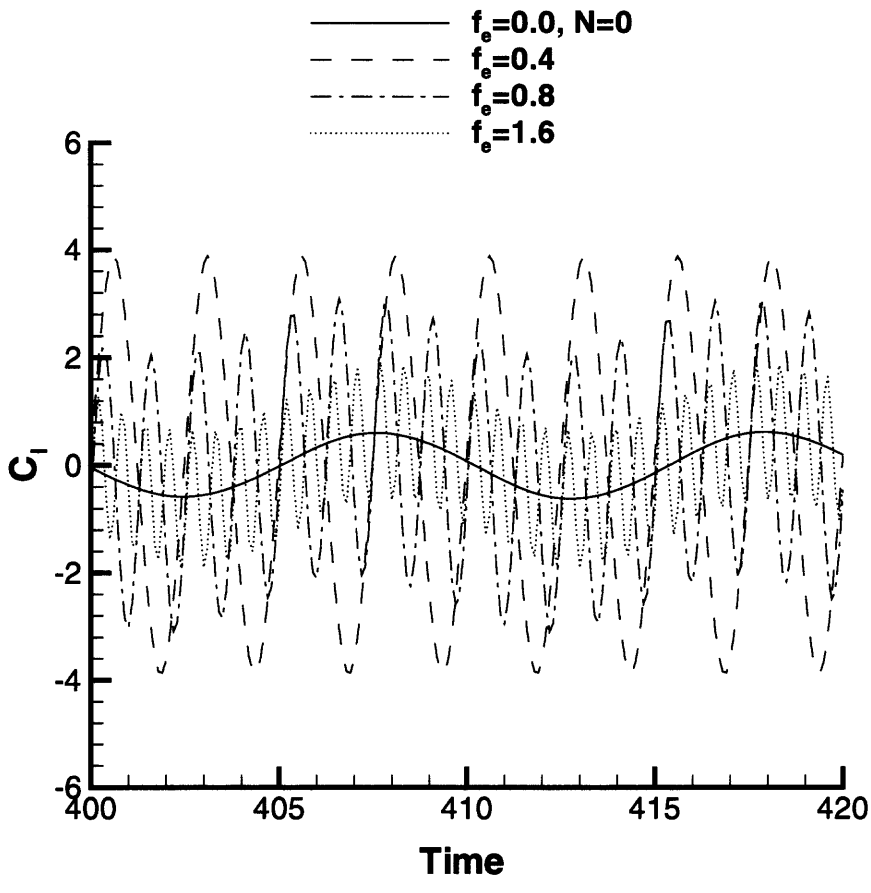

(c) N=20

Figure 3.15 Time history of the lift coefficient for various values of the interaction parameter and Lorentz force frequency in the case of an antisymmetric Lorentz force.

3.4 Summary

In this chapter, the two dimensional Navier-Stokes equations with open loop control are solved numerically. The control actuators exert Lorentz forces which are distributed on both halves of the cylinder surface. With the use of a symmetric and static Lorentz force over the entire surface of the cylinder, the vortex shedding behind the cylinder weakens and eventually completely disappears when the Lorentz force (or interaction parameter) is sufficiently large.

The localized Lorentz force along the rear surface of the cylinder was also used to control the vortex shedding behind the cylinder. In this case, our numerical results show that the efficiency of the localized Lorentz force in controlling the flow is to that of the Lorentz force distributed over the whole surface. When the interaction parameter is about $N \geq 3$, vortex shedding completely disappears, and the total drag coefficient decreases as the Lorentz force increases due to the predominant role played by the pressure on the total drag coefficient.

When a sinusoidal Lorentz force is applied, with the force frequency higher than the Strouhal frequency and an appropriately chosen interaction parameter, the cylinder flow consists of a vortex street which is more narrow than it is in the unforced case. For force frequencies near the Strouhal frequency, a lock-in of the flow occurs even for small values of the interaction parameter and the frequency of the flow is determined by the frequency of the Lorentz force. As the Lorentz force frequency increases, the flow exhibits two different frequencies, one corresponding to the vortex shedding frequency and another one coinciding with the Lorentz force frequency.

CHAPTER 4

CLOSED-LOOP CONTROL OF THE CYLINDER WAKE

From previous studies, we know the flow past a cylinder can be controlled by applying electromagnetic forces on the surface of the cylinder in an electrically conducting fluid. However, it is not economical to apply the Lorentz forces over the entire cylinder surface and/or at all times. The extent of the area of actuation, together with the time period during which it is applied, need to be considered. In this chapter, we consider closed-loop control for this purpose. When vortex shedding appears, it is accompanied by flow separation, asymmetry in the pressure on the surface of the cylinder occurs, and fluctuations in the drag and lift coefficients. Two effective closed-loop control algorithms for manipulating wake flows are developed here, based on the detection (sensing) of the flow separation point on the surface of the solid body. The actuators are the same as those described in Chapter 2 and consist of an array of electrodes and magnets suitably mounted on the localized surface of the cylinder. In our numerical code, our control technique is applied at every computational time step ($\Delta t = 0.005$) That is, sensing and actuation are updated at every computational time step.

4.1 Closed-Loop Control with $C_d = 0$

There is obviously a close relation between vortex shedding and flow separation on the surface of the cylinder. When vortex shedding takes place, the separation point moves along the surface of the cylinder. From Sections 3.1 and 3.2, we know that the suppression of flow separation can suppress vortex shedding and lead to a steady flow solution. It seems, therefore, appropriate to base our sensor on detecting flow separation. The flow separation point is identified as the location where the shear

stress is zero, that is where $\tau_{r\theta} = 0$. From Equation (2.22), we see that

$$\begin{aligned} \tau_{r\theta} &= \mu \frac{\partial u_\theta}{\partial r} \\ &= \mu\Omega \end{aligned}$$

From the above equation, the shear stress is proportional to the vorticity (Ω). Thus, the separation point can be also identified as a zero-vorticity point.

There is always a deficit in momentum in the (uncontrolled) flow past a cylinder. Since the momentum deficit is measured by the momentum thickness which is directly proportional to the drag force on the cylinder (Ronald L. Panton, 1996), the momentum added to the fluid by applying the Lorentz force can balance the momentum deficit caused by the cylinder, the thus leading to zero momentum thickness. In this case, the drag force will also be equal to zero. The corresponding interaction parameter, that is the interaction parameter needed to suppress any non-zero drag, can be derived from Equation (2.21) as follows.

$$N = \frac{1}{\pi Re} \frac{\int_0^1 (2\pi\Omega - \frac{\partial\Omega}{\partial\xi}) sin(2\pi\eta) d\eta}{\int_0^1 F_\theta sin(2\pi\eta) d\eta}. \tag{4.1}$$

Inspired by the investigation of Park *et al* (1994), the start-up point of the location of our actuators has been chosen at 10° degrees upstream of the separation point. The expression of $\vec{F}$ in Equation (2.8) can be written as follows.

$$\vec{F} = e^{-\alpha(r-1)} g(\theta) \vec{e_\theta} \qquad with \quad g(\theta) = \begin{cases} 1 & \theta' - 10° \leq \theta \leq 175° \\ -1 & 185° \leq \theta \leq 370° - \theta' \\ 0 & \text{elsewhere} \end{cases} \tag{4.2}$$

Here, the angle θ' denotes the location of the separation point at any time on the upper surface of the cylinder. Obviously, θ' is a function of time.

The control switch has been turned on in the following manner. Control is turned on only when the separation point leaves a small neighborhood of the rear stagnation point (within 5° degrees). Otherwise, it is turned off. Our numerical simulation results show that the separation point moves along the cylinder surface even after control is turned on, due to the unsteadiness of the flow.

When control is applied at, or downstream of, the separation point, the efficiency of the control technique is compromised. There is thus a need to activate actuators slightly upstream of the separation point.

Thus a detection system has been built to adapt to this need. When the absolute value of the vorticity at a point on the rear surface of the cylinder decreases below a certain threshold δ ($\delta > 0$), expressed as $\mid \Omega \mid \leq \delta$, we turn on the actuator. In our numerical simulation, we have chosen $\delta = 3.0$. Now the numerical results has been described by using this technique.

The closed-loop control is applied to the flow at Reynolds number $Re = 200$, starting at time $t = 440$, when the flow is in its well-developed vortex shedding regime (Figure 4.2b). Figure 4.1 shows the instantaneous vorticity contours and the corresponding streamlines at $Re = 200$ when the closed-loop control technique is in effect. One observes that the separation point disappears and that vortex shedding is fully suppressed. This can be compared to the instantaneous vorticity contours and flow streamlines obtained without control at time $t = 200$ and $t = 400$ (Figure 4.2). Figures 4.3 and 4.4 highlight the process through which vortex shedding is suppressed over a short time period. It is clear that our closed-loop control strategy has a significant effect on the flow and that it successfully suppresses any time dependency of the flow.

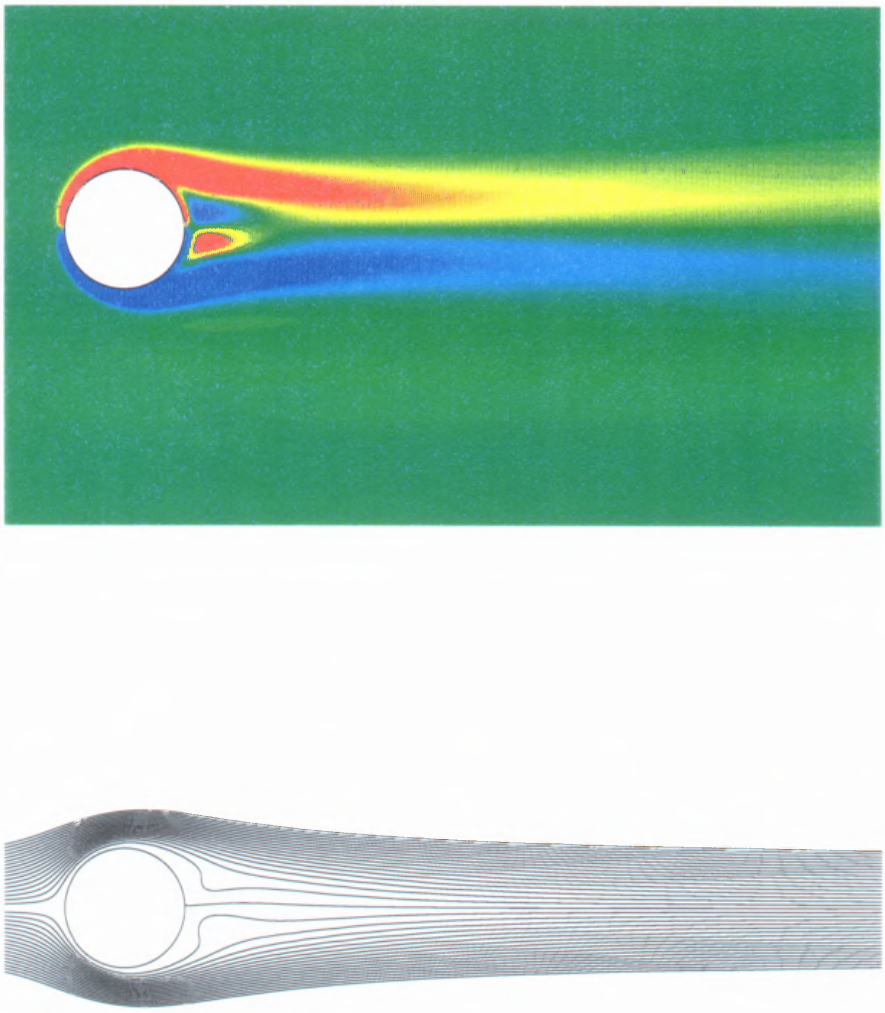

Figure 4.1 Instantaneous vorticity contours and corresponding flow streamlines at $t = 600$ after the closed-loop control algorithm is applied.

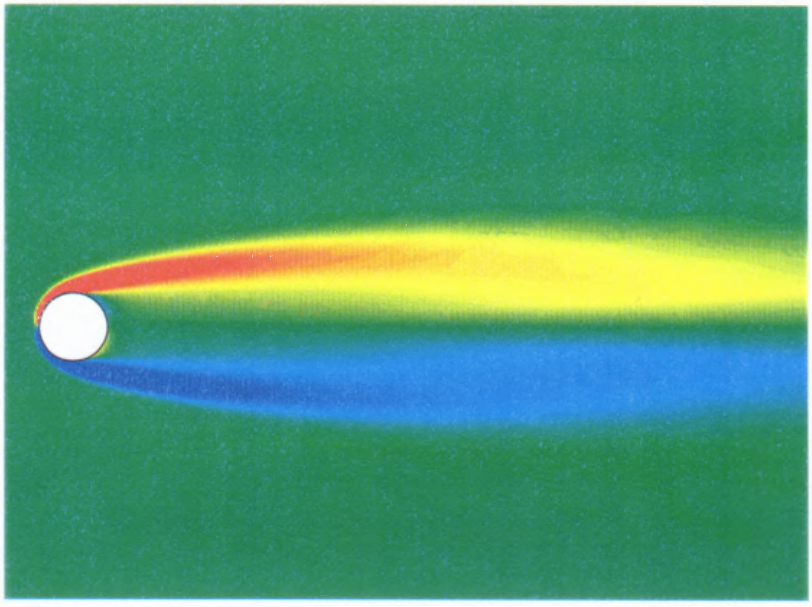

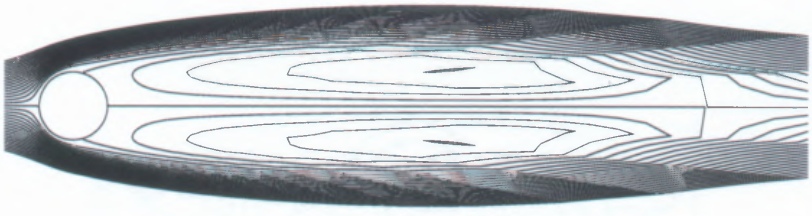

(a) t=200

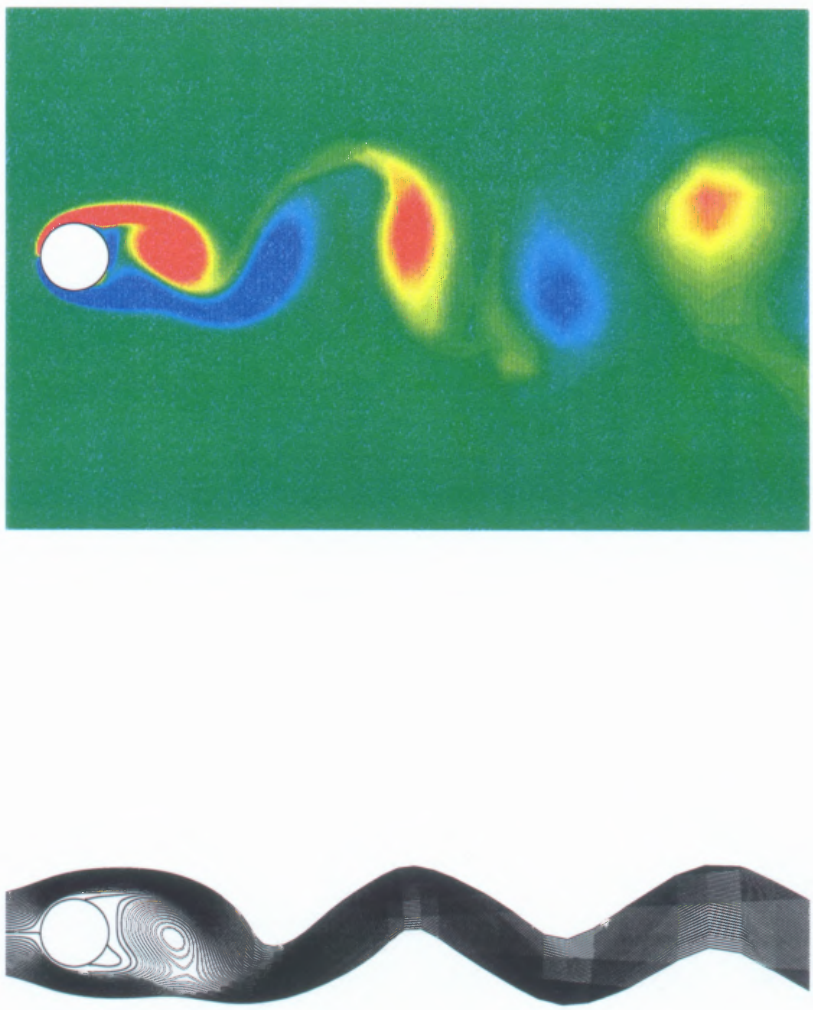

(b) t=400

Figure 4.2 Instantaneous vorticity contours and corresponding flow streamlines in the uncontrolled flow.

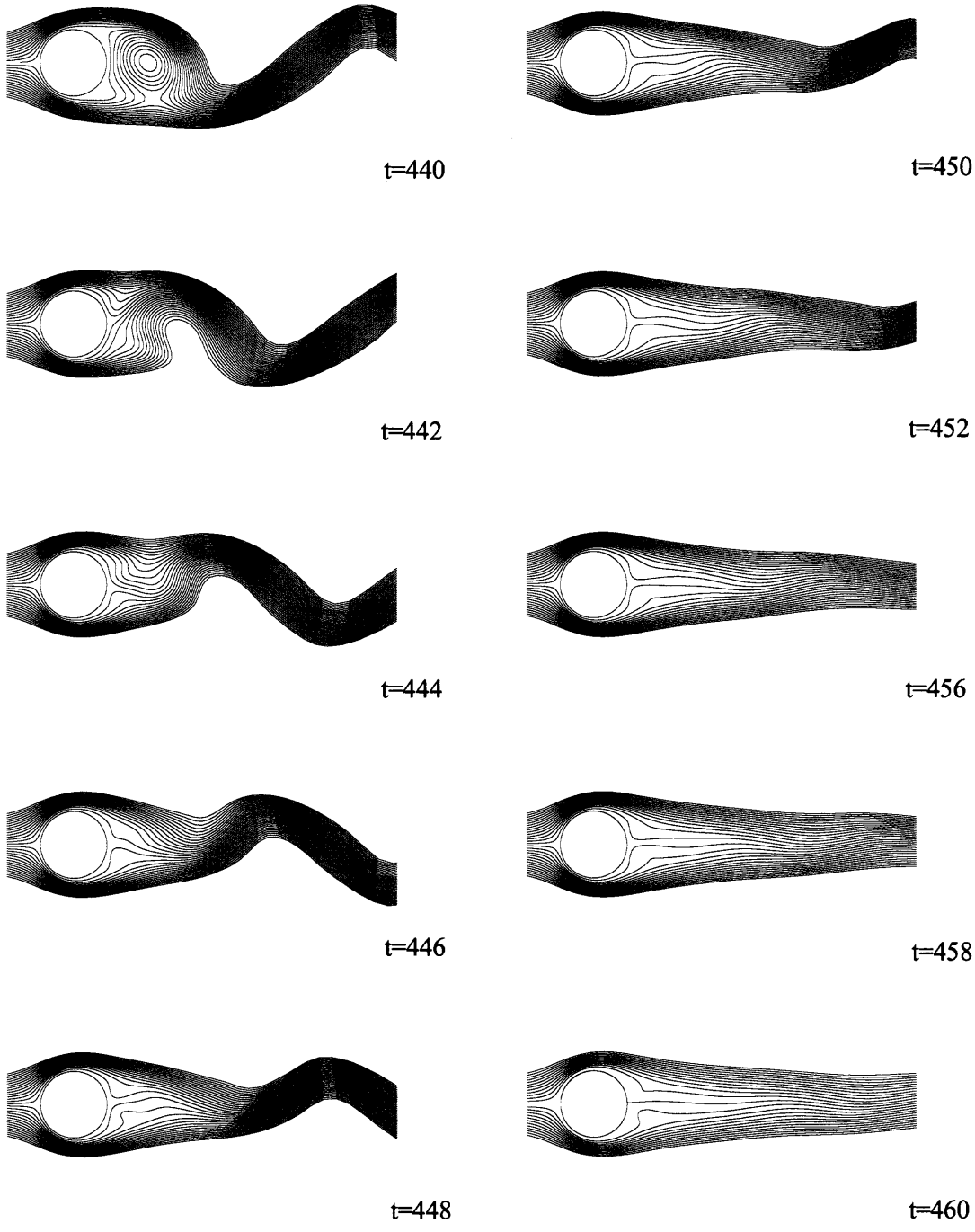

Figure 4.3 Streamlines showing the suppression of vortex shedding by closed-loop control. The closed-loop control algorithm is applied at time $t = 440$ and successive times.

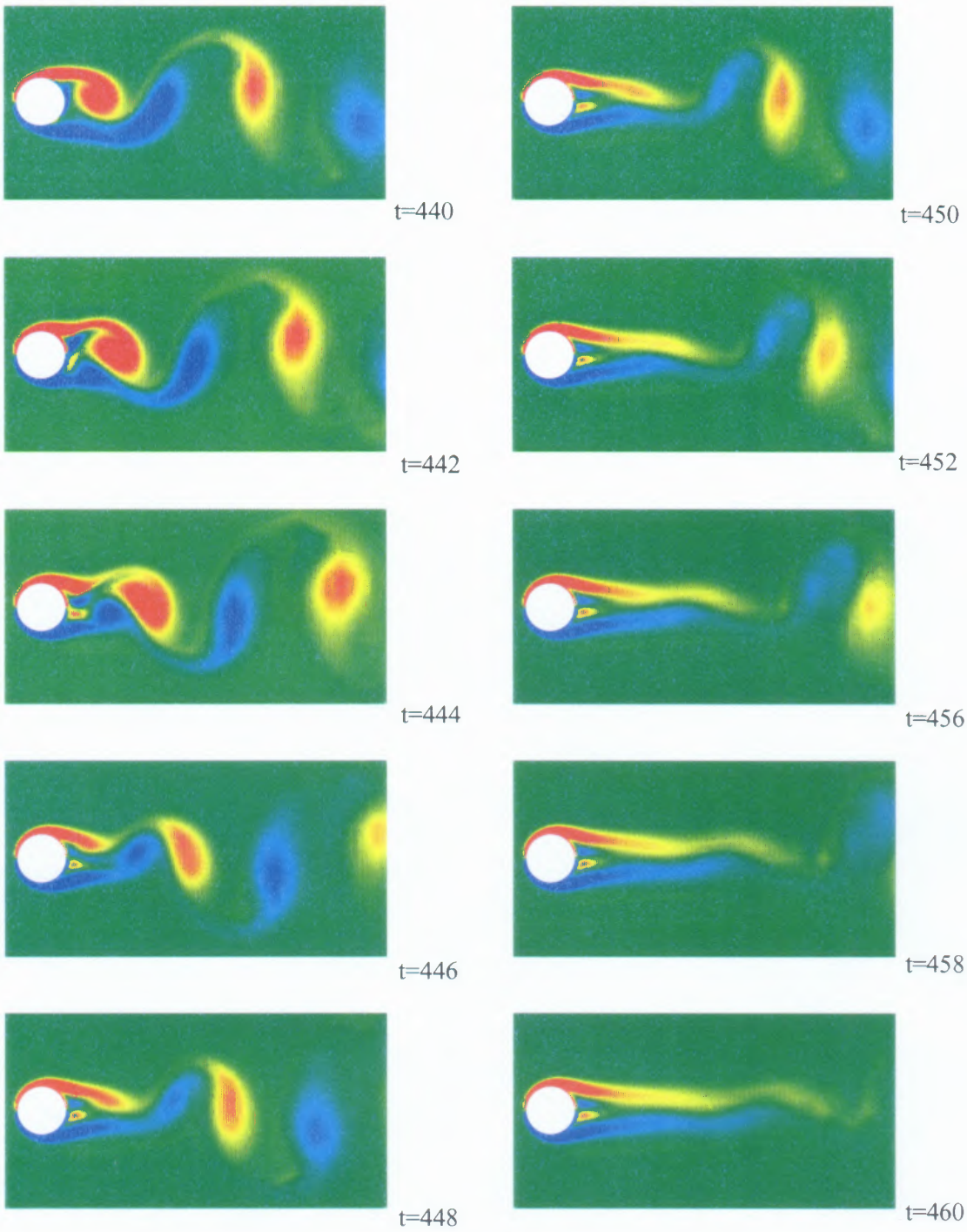

Figure 4.4 Vorticity contours showing the suppression of the vortex shedding by feedback control. The closed-loop control algorithm is applied at time $t = 440$ and successive times.

The vorticity and pressure distributions on the solid body can be compared to the uncontrolled flow results in Figures 4.5 and 4.6. As before, the angle θ is defined from the front to the rear stagnation point. In particular, the vorticity distribution in Figure 4.5 shows that the separation is suppressed with the application of the Lorentz force and that the vorticity on the surface of the cylinder is increased compared with that of the uncontrolled flow. Again, this is due to the fact that the fluid is accelerated by the Lorentz force and that the shear stress on the surface of the cylinder is increased. Likewise, the pressure distribution decreases under the influence of the Lorentz force along the actuation area, while it increases at the rear stagnation point due to the reduction of the recirculation region.

Figure 4.7 shows the time history of the lift and drag force coefficients. It is clear that both coefficients are successfully reduced to almost zero. Under the action of the control, the pressure drag decreases to a negative value while the friction drag increases, so that they eventually balance each other, resulting in zero total drag.

Figure 4.8a shows the time history of the interaction parameter and the location of the separation point. After the time when the control algorithm is switched on, the interaction parameter first fluctuates and then becomes stable. From Figure 4.8b, one can see that the separation point vibrates along the rear surface of the cylinder in the uncontrolled flow and that it mighrates to the rear stagnation point over a very short amount of time. In this region, such vibrations are fully suppressed.

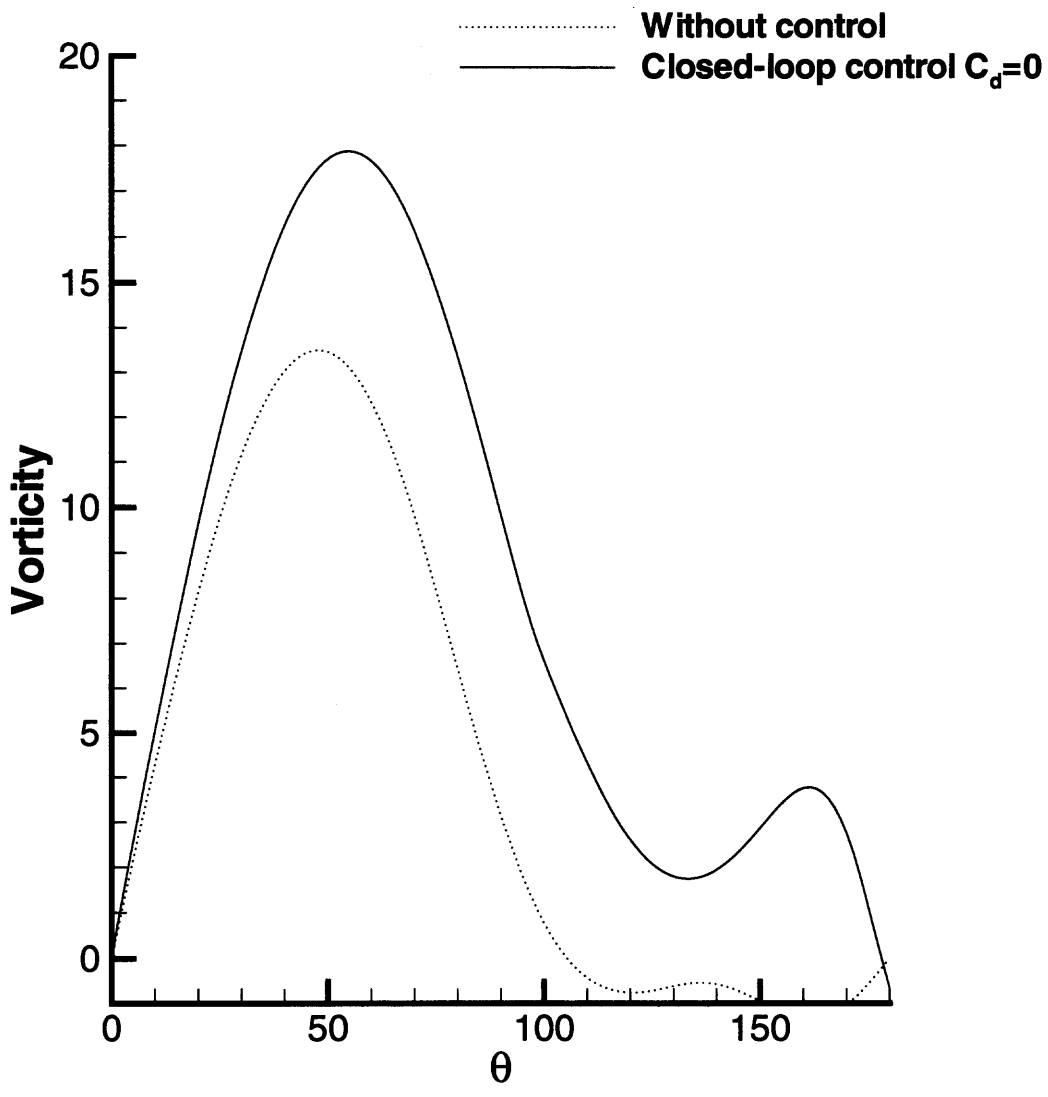

Figure 4.5 Vorticity distribution on the cylinder surface from the front stagnation point to rear stagnation point in the uncontrolled flow, as well as in the flow with closed-loop control.

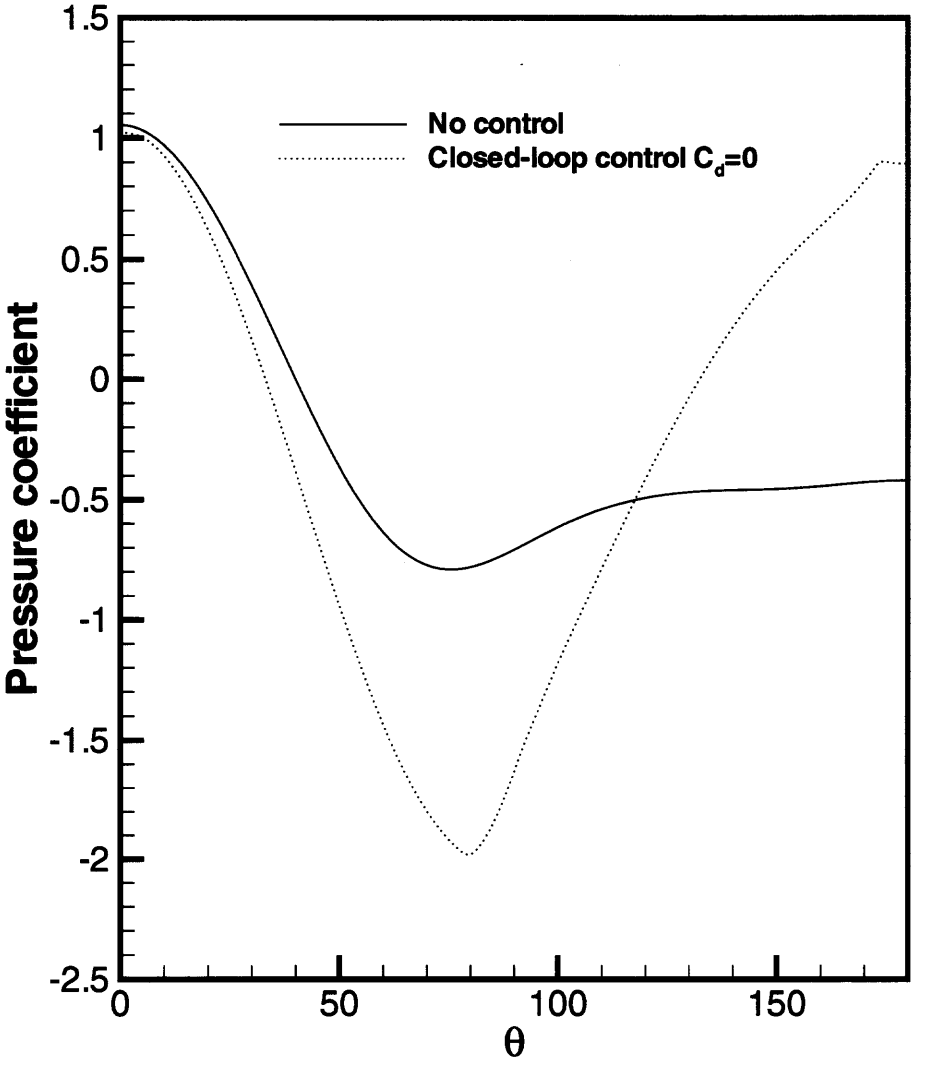

Figure 4.6 Pressure distribution on the cylinder surface from the front stagnation point to the rear stagnation point, in the uncontrolled flow, as well as in the flow with closed-loop control.

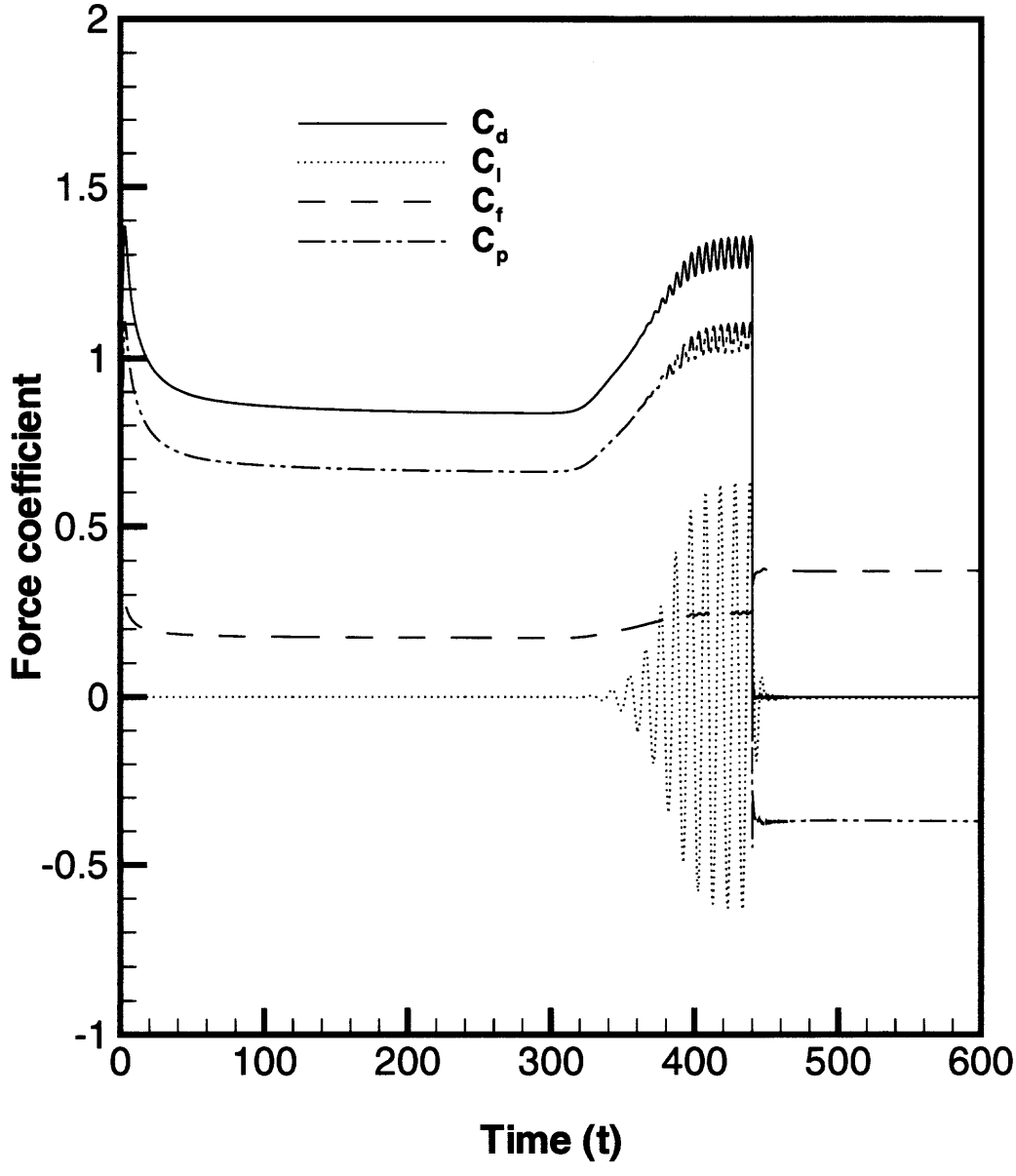

Figure 4.7 Time history of the drag and lift force coefficients. The closed-loop control is applied at time $t = 440$ and at successive times.

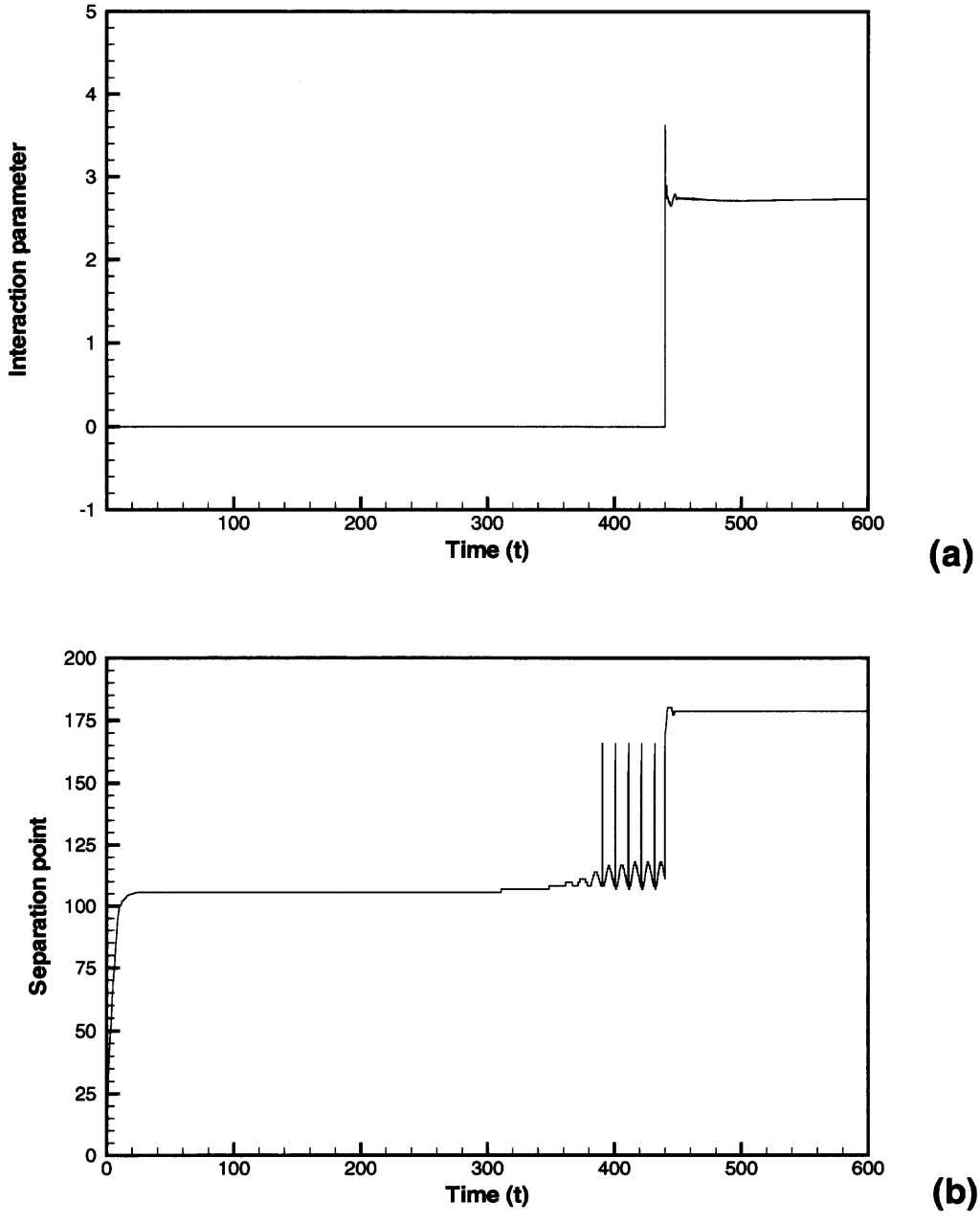

Figure 4.8 Time history of (a) the interaction parameter and (b) the location of the separation point. The closed-loop control is applied at time $t = 440$ and at successive times.

4.2 Closed-Loop Control with $C_{pd} = 0$

In the previous section, we developed a closed-loop control technique for the control of the vortex shedding behind a circular cylinder with the use of actuators (exerting the Lorentz force) in order to make the total drag coefficient equal to zero. In the present section, a similar closed-loop control algorithm is used to make the pressure drag coefficient equal to zero ($C_{pd} = 0$). From Equation (2.21), we can derive the expression for the interaction parameter as follows.

$$N = -\frac{1}{\pi Re}\frac{\int_0^1 \frac{\partial \Omega}{\partial \xi} sin(2\pi\eta)d\eta}{\int_0^1 F_\theta sin(2\pi\eta)d\eta}. \tag{4.3}$$

In this case, the fact that the pressure drag coefficient is equal to zero implies that the total drag coefficient is equal to the friction drag coefficient only, which is larger than zero. This is caused by the applied Lorentz force that increases the wall friction and, therefore, makes the friction drag coefficient larger than before.

Figure 4.9 shows the instantaneous vorticity contours and streamlines at two times, $t = 600$ and $t = 700$ for the flow at Reynolds number $Re = 200$, after the closed-loop control algorithm is applied, based on $C_{pd} = 0$. A comparison with Figure 4.1 shows that it takes a longer time to stabilize the flow to a steady solution using this technique rather than the previous one. Figures 4.10 and 4.11 display the vorticity contours and flow streamlines, showing the destabilization process of vortex shedding by closed-loop control based on $C_{pd} = 0$. The time it takes to control the flow is larger than the time it takes to control the flow based on $C_d = 0$. During the initial period, vortex shedding persists but weakens, corresponding to lift fluctuations (Figure 4.15) which, however, are much smaller than those corresponding to the uncontrolled flow.

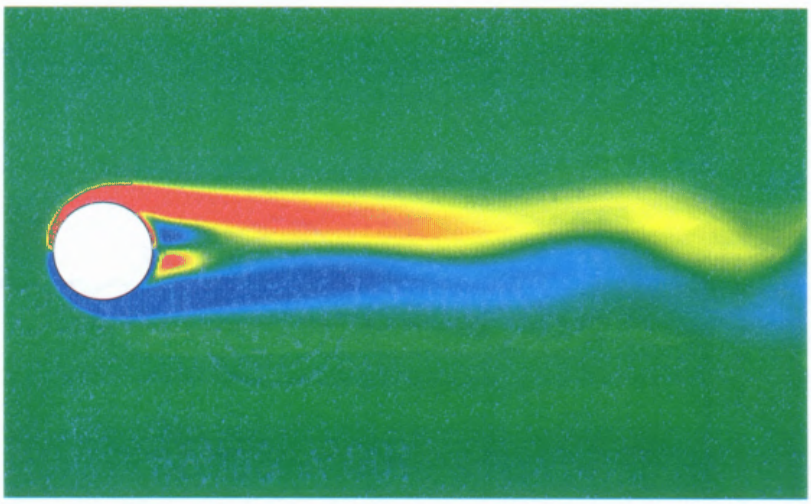

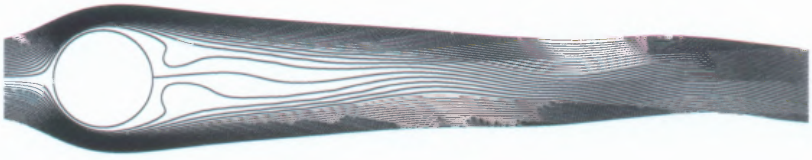

(a) t=600

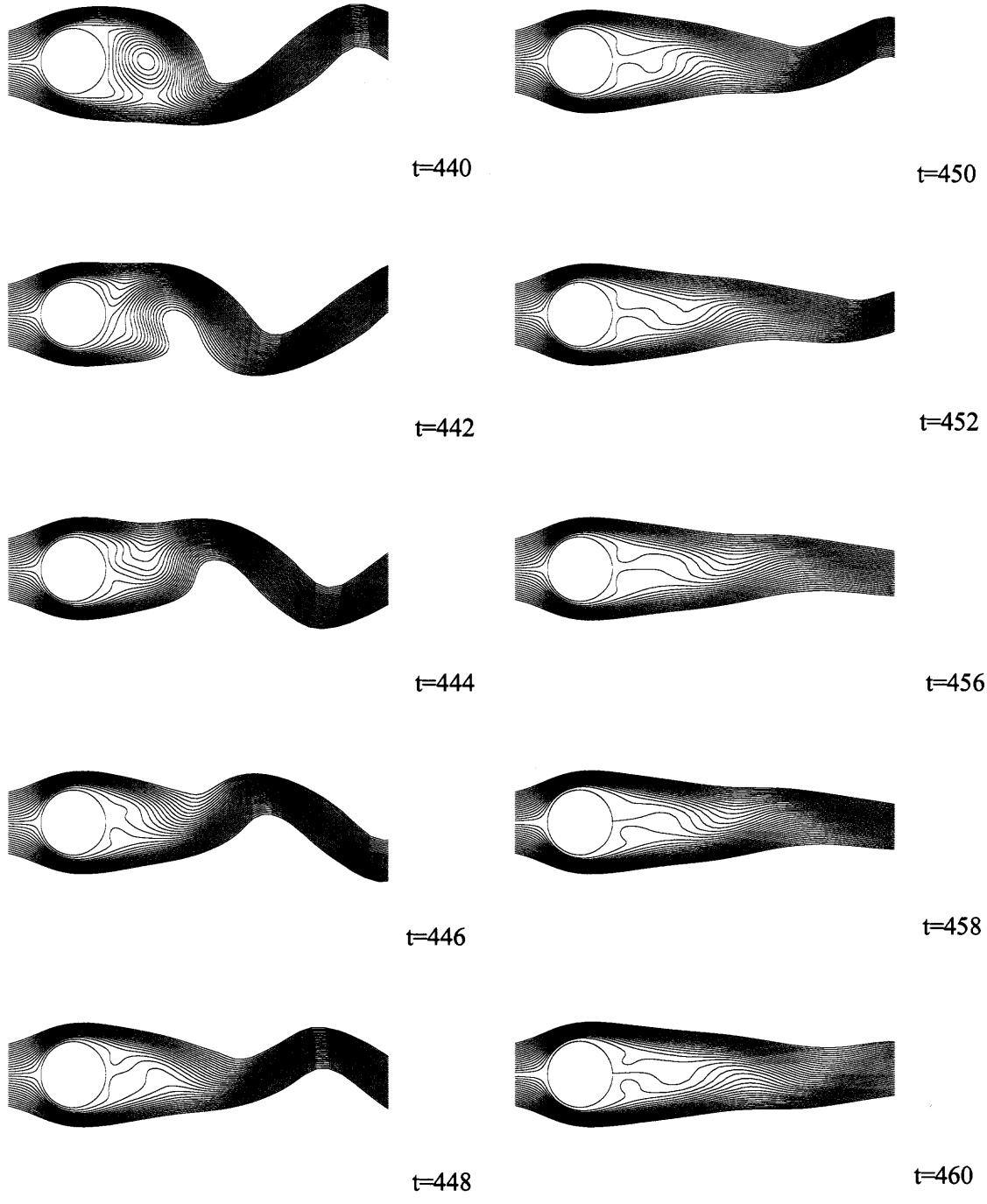

Figure 4.10 Flow streamlines showing the destabilization of vortex shedding by the closed-loop control technique based on $C_{pd} = 0$. Control starts at time $t = 440$.

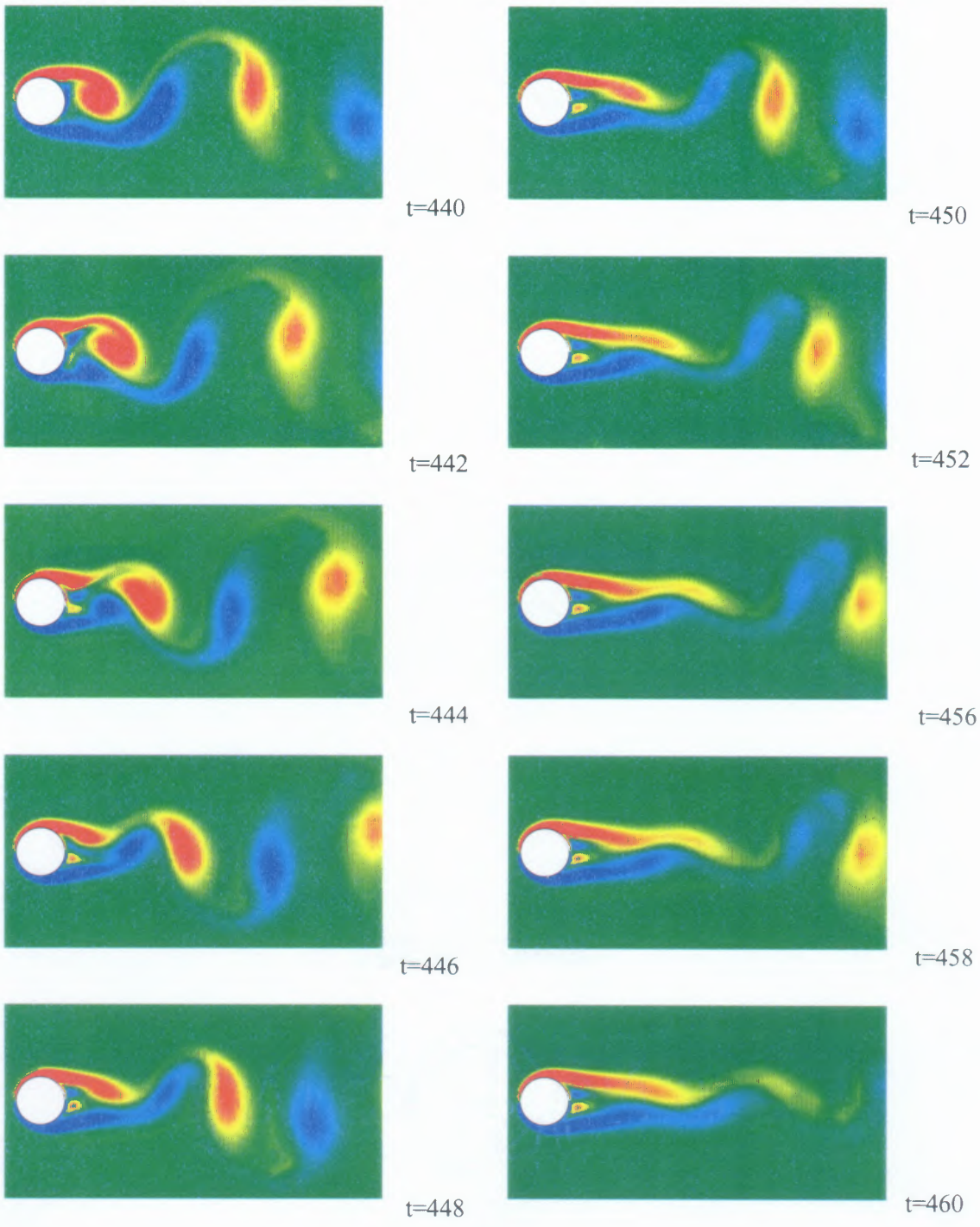

Figure 4.11 Vorticity contours showing the destabilization of vortex shedding by the closed-loop control technique based on $C_{pd} = 0$. Control starts at time $t = 440$.

After this initial period, vortex shedding disappears completely leading to a steady reattached flow, whose lift is constant and equal to zero (Figure 4.16).

Figures 4.12 and 4.13 show the vorticity and pressure distributions on the cylinder surface from the front stagnation point to the rear stagnation point, without control and with the two closed-loop control algorithms. Using both control methods ($C_d = 0 and C_{pd} = 0$), the separation point has been suppressed (or, equivalently, moved to the rear stagnation point). The vorticity obtained with the closed-loop control technique based on $C_d = 0$ is larger than that obtained with control whose target is $C_{pd} = 0$. This is due to the larger value of the interaction parameter in the first case, resulting in a larger wall shear stress, and therefore larger vorticity. Similarly, Figure 4.13 shows that the pressure obtained with the first technique is lower than that corresponding to the second technique.

Figure 4.14 allows a comparison between the time history of the interaction parameter using both techniques ($C_d = 0$ and $C_{pd} = 0$). The interaction parameter corresponding to $C_{pd} = 0$ is smaller than that obtained with $C_d = 0$. This is due to the fact that $C_{pd} = 0$ requires less energy since, in this case, the flow needs to counteract the friction effect only.

The time history of the force coefficient for the closed-loop control technique whose target is $C_{pd} = 0$ is shown in Figure 4.15. Figures 4.16 and 4.17 show the time history of the force coefficient for both $C_{pd} = 0$ and $C_d = 0$. The value of the lift coefficient in both cases is very close to zero, but the lift fluctuation time in the case where $C_{pd} = 0$ is the goal is longer than it is for $C_d = 0$. For $C_{pd} = 0$, the total drag reduces to the friction drag C_{fd}. In this case, the latter is smaller than it is when $C_d = 0$ is imposed, corresponding to a smaller interaction parameter.

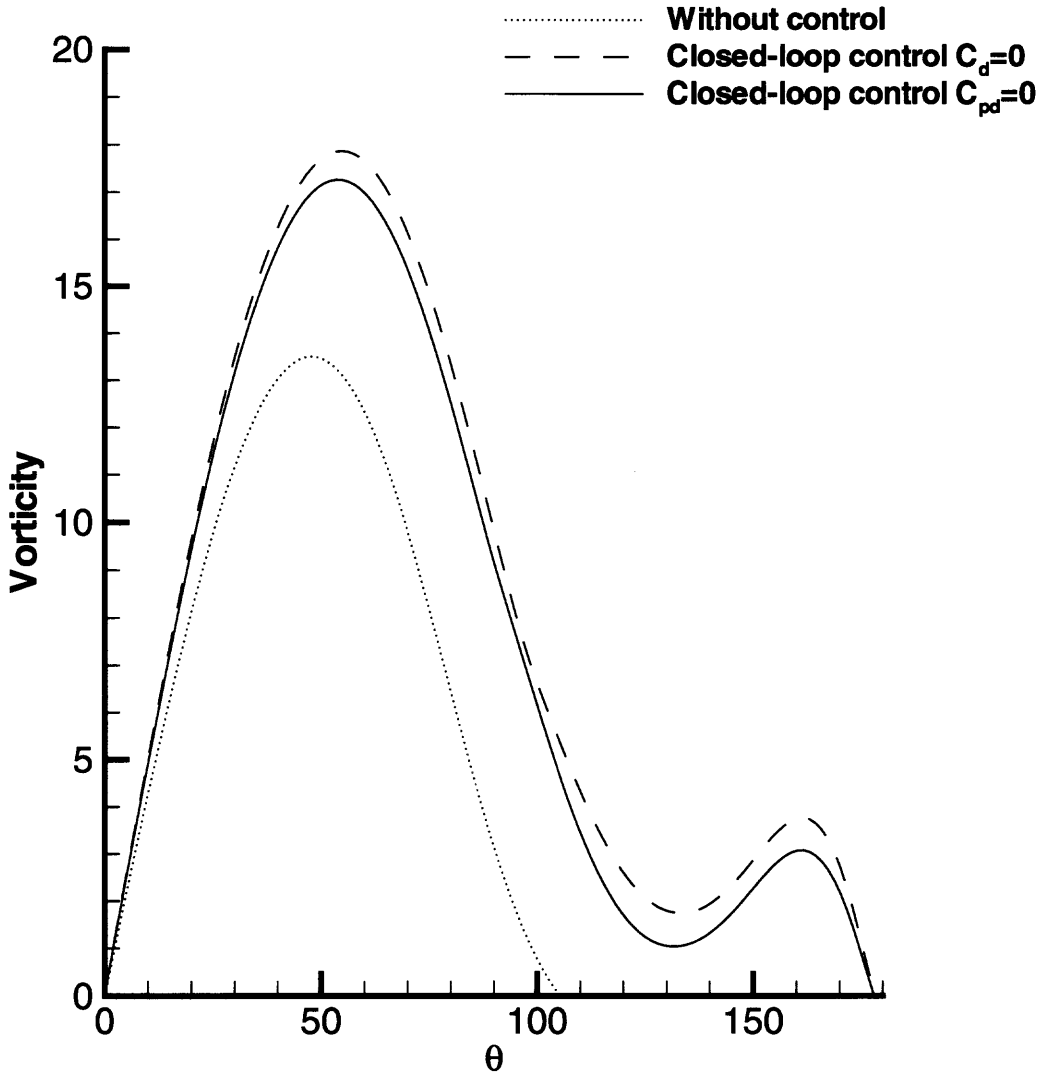

Figure 4.12 Vorticity distributions on the cylinder surface from the front stagnation point to rear stagnation point for the uncontrolled flow and the flow controlled with the two closed-loop control techniques ($C_{pd} = 0$ and $C_d = 0$). Control starts at time $t = 440$.

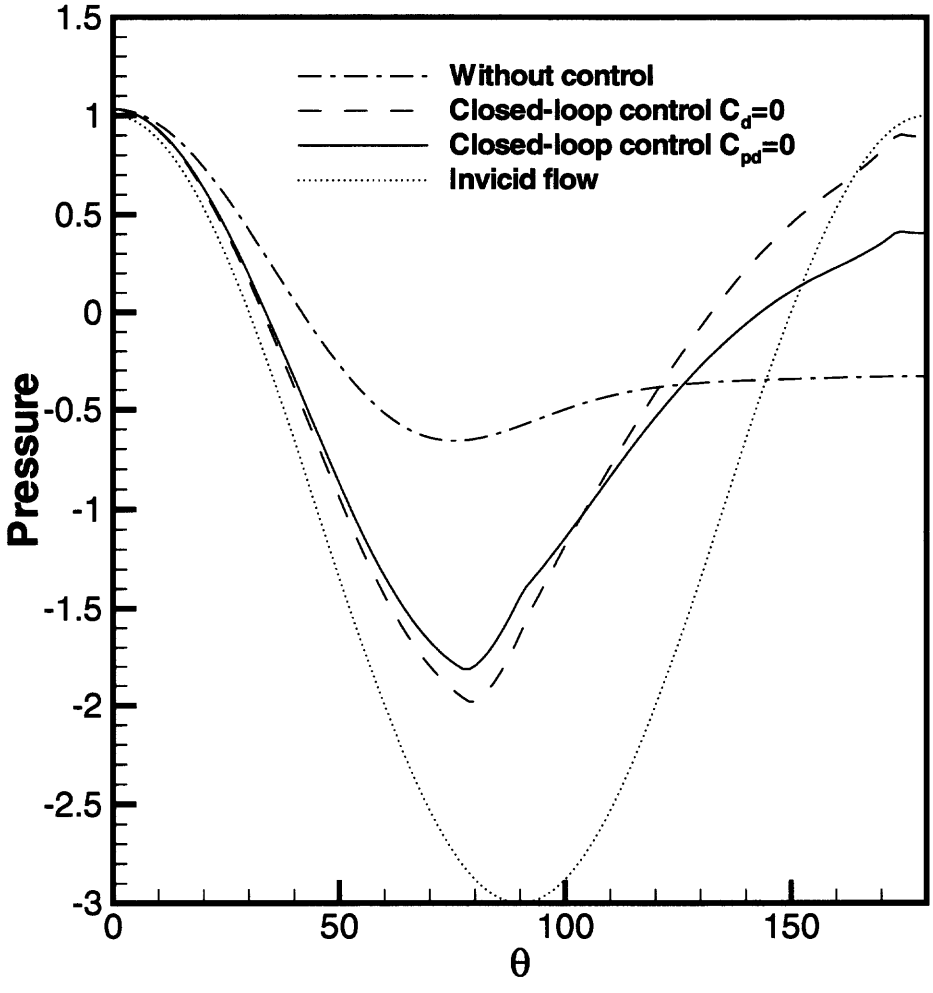

Figure 4.13 Pressure distribution on the cylinder surface from the front stagnation point to the rear stagnation point for the uncontrolled flow and the flow controlled with the two closed-loop control techniques ($C_{pd} = 0$ and $C_d = 0$). Control starts at time $t = 440$.

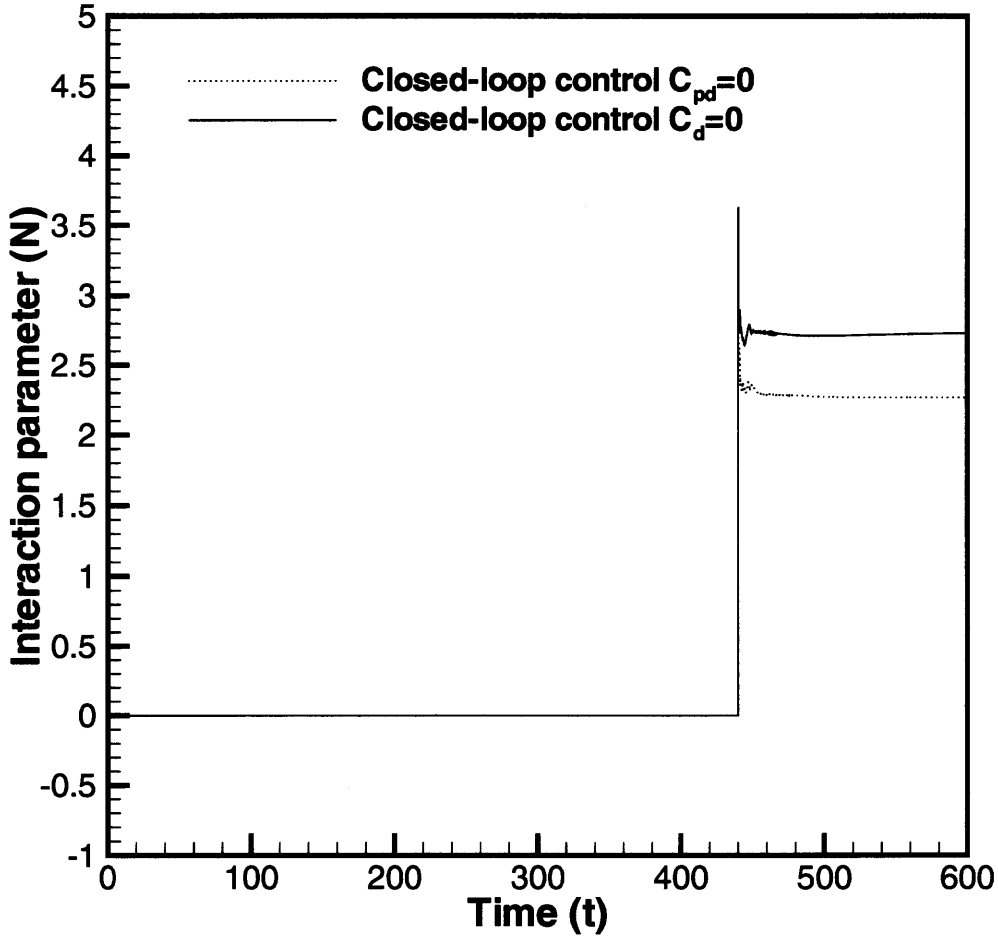

Figure 4.14 Time history of the interaction parameter for the flow controlled with the two closed-loop control techniques ($C_{pd} = 0$ and $C_d = 0$). Control starts at time $t = 440$.

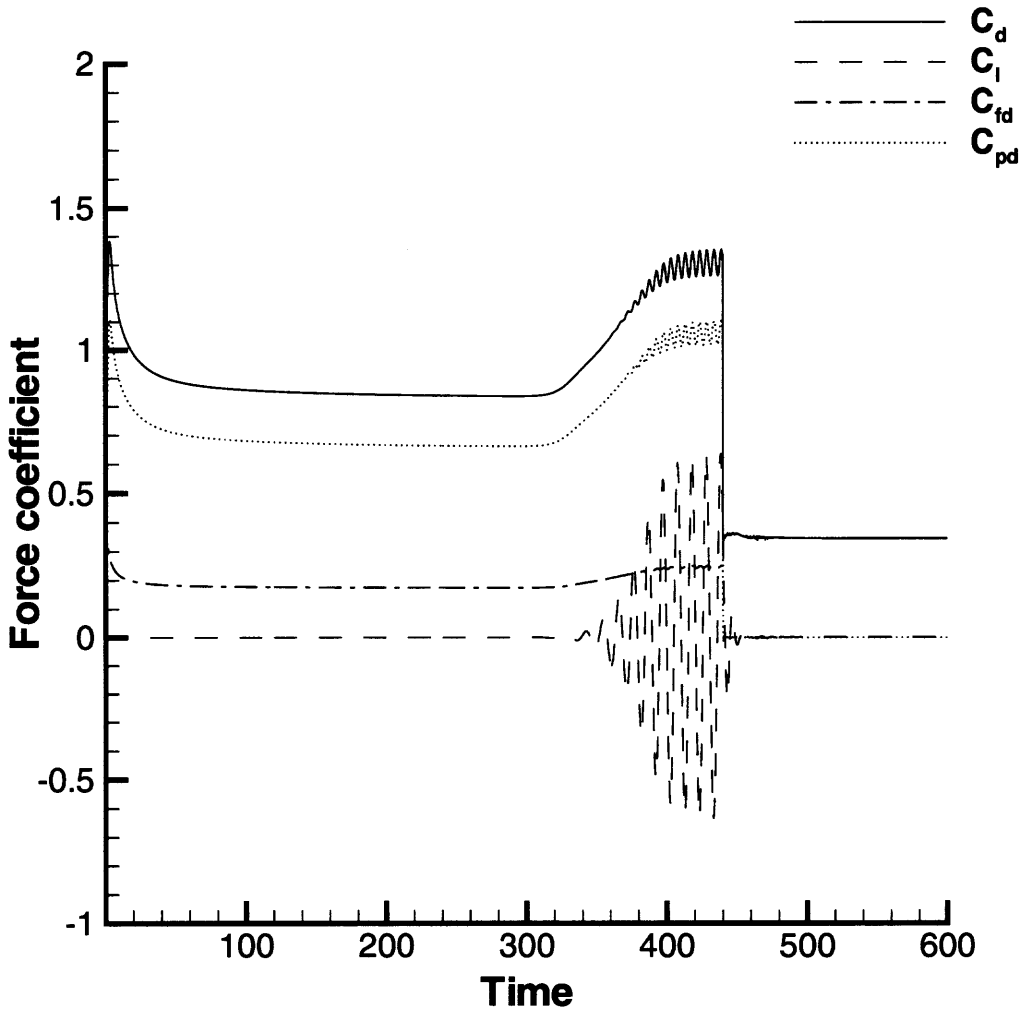

Figure 4.15 Time history of the force coefficient for feedback control with $C_{pd} = 0$. Control starts at time $t = 440$.

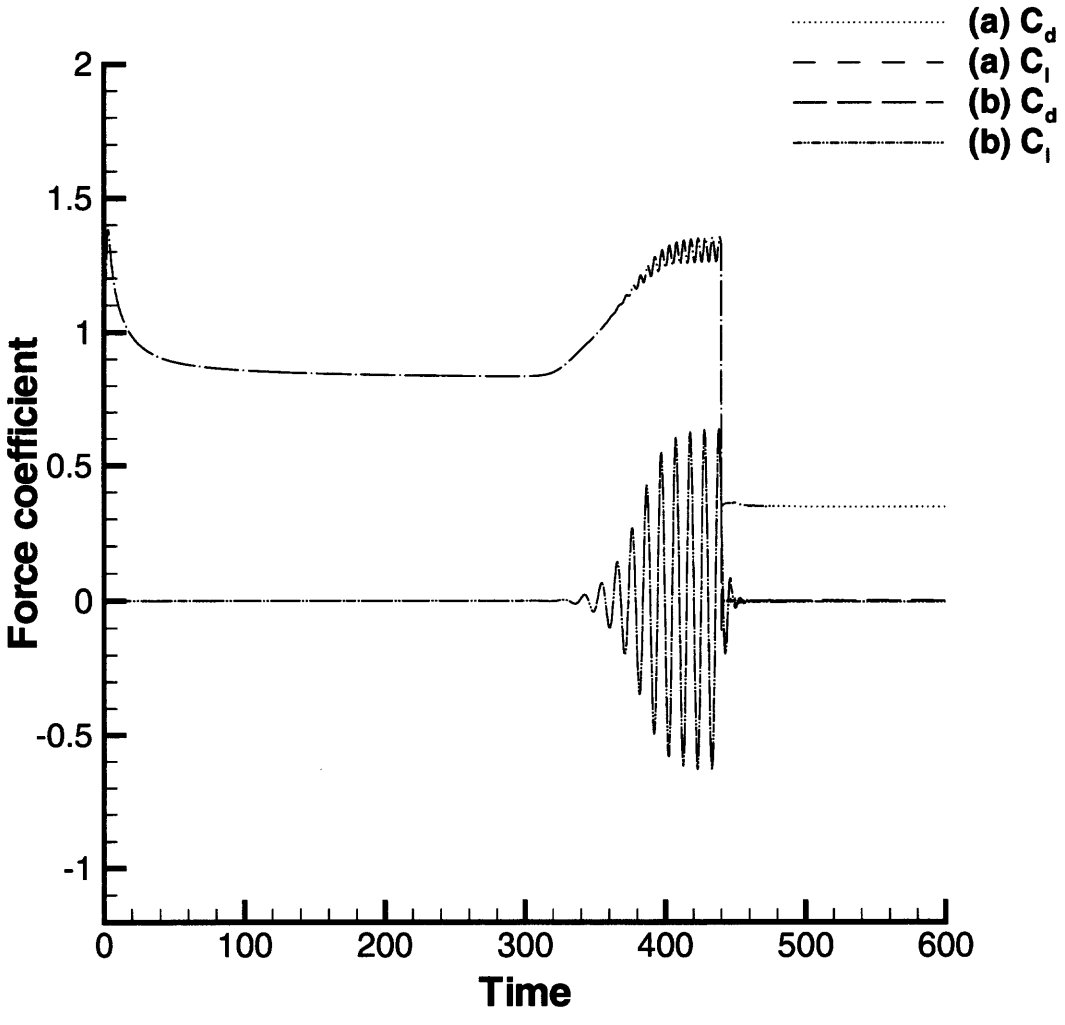

Figure 4.16 Time history of the drag and lift force coefficients for the flow controlled with the closed-loop control technique based on (a) $C_{pd} = 0$ and (b) $C_d = 0$. Control starts at time $t = 440$.

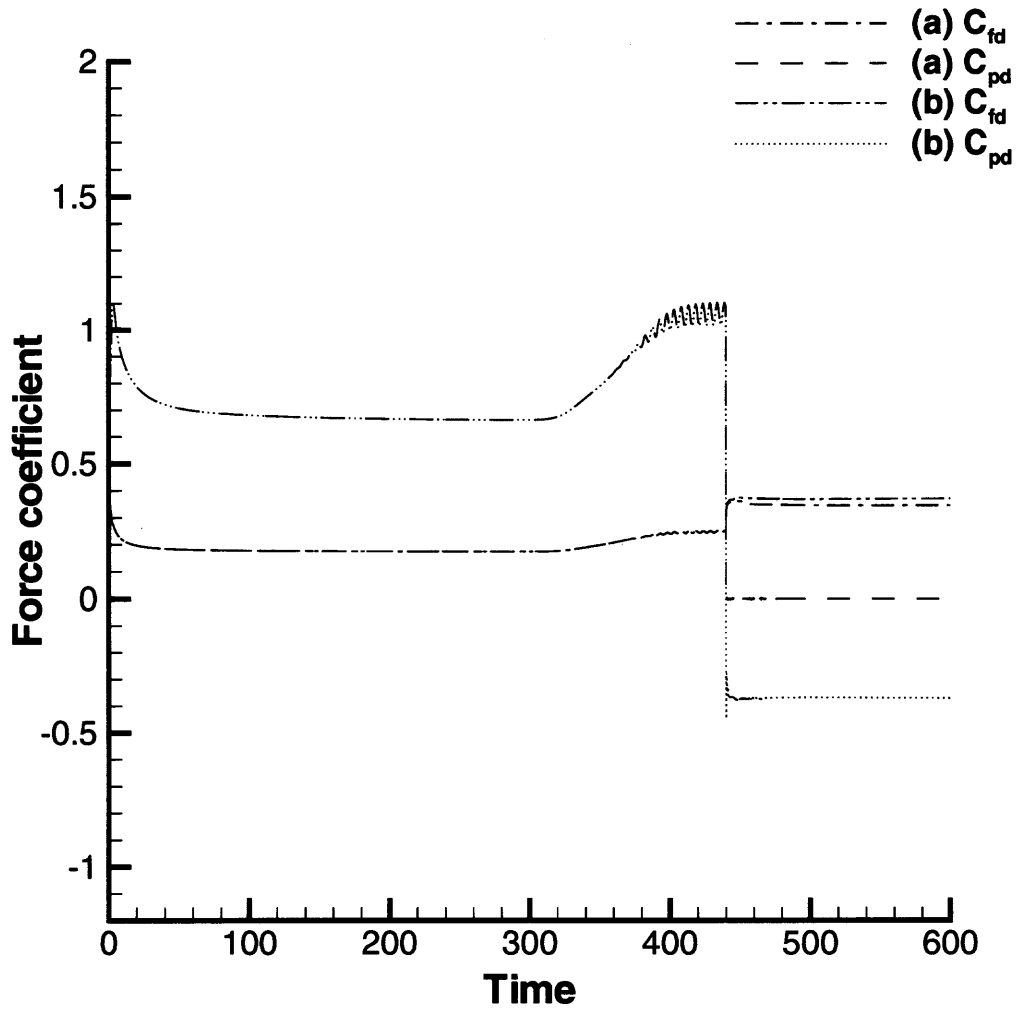

Figure 4.17 Time history of the drag and lift force coefficients for the flow controlled with the closed-loop control technique based on (a) $C_{pd} = 0$ and (b) $C_d = 0$. Control starts at time $t = 440$.

4.3 Summary

Closed-loop control procedures targetting either zero total drag, $C_d = 0$, or zero pressure drag, $C_{pd} = 0$, were developed and applied to the flow behind a circular cylinder at $Re = 200$. In both cases, the location of sensors was limited to the surface of the cylinder and to the measurement of the wall shear stress. The actuators consisted of arrays of electrodes and magnets located on the cylinder surface and exerting a Lorentz force on the fluid. The location of the actuators was determined by the information fed by the sensors (more precisely, the location of the separation of the separation point), and the intensity of the Lorentz force was calculated from the requirement that $C_d = 0$ or $C_{pd} = 0$.

For the closed-loop control technique whose target is zero drag, i.e. $C_d = 0$, vortex shedding is fully suppressed, and the flow becomes stable after a relatively short time. The (total) drag and lift coefficients have been reduced to almost zero successfully. The pressure drag reaches a negative value in order to balance the (positive) friction drag. For the closed-loop control technique whose target is $C_{pd} = 0$, the time needed to control the flow is longer than for the first technique ($C_d = 0$). The lift coefficient of the stabilized controlled flow is close to zero, and the friction drag and interaction parameter values are smaller than they were when the first technique ($C_d = 0$) was employed.

CHAPTER 5

CLOSED-LOOP CONTROL OF VORTEX-INDUCED VIBRATIONS

The appearance of vortex shedding is accompanied by a fluctuation of the lift force. If the cylinder is free to move in the cross-flow direction, it will vibrate in that direction due to the fluctuating lift. A general method to solve this *fluid/structure* interaction problem is by using the Arbitrary Lagrangian Eulerian (ALE) formulation, in conjunction with the new spectral discretization on unstructured grids, in order to deal with the moving computational domain and dynamic re-meshing (Warburton & Karniadakis, 1996). However, if we consider the motion of the cylinder in the fluid at rest by attaching one system of coordinates to it, the difficulty of a moving mesh can be eliminated (Dimas & Triantafyllou, 1994 and Newman & Karniadakis, 1997).

5.1 Governing Equations

Two frames of reference can be naturally introduced for the description of the problem. One is the inertial system connected to the stationary fluid. The other one moves with the cylinder and is therefore an accelerated system of reference . Their $two - dimensional$ Cartesian coordinates can be denoted by x', y' and x, y respectively, and the relationship between the two systems of coordinates is given as follows.

$$x' = x + \bar{x}(t)$$

$$y' = y + \bar{y}(t)$$

Here $\bar{x}(t)$ and $\bar{y}(t)$ denote the position of the accelerated system of reference, so the velocity components can be expressed as

$$u' = u + \frac{d\bar{x}(t)}{dt} = u + \bar{u} \tag{5.1}$$

$$v' = v + \frac{d\bar{y}(t)}{dt} = v + \bar{v} \tag{5.2}$$

The two-dimensional incompressible Navier-Stokes equations in the fixed inertial system can be written as

$$\nabla' \cdot \vec{u'} = 0 \tag{5.3}$$

$$\frac{\partial \vec{u'}}{\partial t} + (\vec{u'} \cdot \nabla')\vec{u'} = -\frac{1}{\rho}\nabla' p' + \nu \nabla'^2 \vec{u'} + \frac{\vec{F_l'}}{\rho} \tag{5.4}$$

Substituting Equations (5.1) and (5.2) into the above equations, we obtain the two-dimensional incompressible Navier-Stokes equations in the transformed system of coordinates.

$$\frac{\partial u}{\partial x} + \frac{\partial v}{\partial y} = 0 \tag{5.5}$$

$$\frac{\partial u}{\partial t} + u\frac{\partial u}{\partial x} + v\frac{\partial u}{\partial y} = -\frac{1}{\rho}\frac{\partial P}{\partial x} + \nu\left(\frac{\partial^2 u}{\partial x^2} + \frac{\partial^2 u}{\partial y^2}\right) + \frac{F_{lx}}{\rho} - \left(\frac{\partial \bar{u}}{\partial t} + \bar{u}\frac{\partial u}{\partial x} + \bar{v}\frac{\partial u}{\partial y}\right) \tag{5.6}$$

$$\frac{\partial v}{\partial t} + u\frac{\partial v}{\partial x} + v\frac{\partial v}{\partial y} = -\frac{1}{\rho}\frac{\partial P}{\partial x} + \nu\left(\frac{\partial^2 v}{\partial x^2} + \frac{\partial^2 v}{\partial y^2}\right) + \frac{F_{ly}}{\rho} - \left(\frac{\partial \bar{v}}{\partial t} + \bar{u}\frac{\partial v}{\partial x} + \bar{v}\frac{\partial v}{\partial y}\right) \tag{5.7}$$

Introducing the vorticity $\Omega = \nabla \times \vec{u}$ and the streamfunction Ψ in the transformed system of coordinates (x, y) as

$$\Omega = \frac{\partial v}{\partial x} - \frac{\partial u}{\partial y}$$

$$u = \frac{\partial \Psi}{\partial y}, \qquad v = -\frac{\partial \Psi}{\partial x}$$

The equation of motion for the vorticity can be obtained from Equations 5.5 – 5.7. It can be written as

$$\frac{\partial \Omega}{\partial t} + (u + \bar{u})\frac{\partial \Omega}{\partial x} + (v + \bar{v})\frac{\partial \Omega}{\partial y} = \nu\left(\frac{\partial^2 \Omega}{\partial x^2} + \frac{\partial^2 \Omega}{\partial y^2}\right) + \frac{1}{\rho}\left(\frac{\partial F_{ly}}{\partial x} - \frac{\partial F_{lx}}{\partial y}\right) \tag{5.8}$$

or, in cylindrical coordinates,

$$\begin{aligned}\frac{\partial\Omega}{\partial t}+(u_r+\bar{u}_r)\frac{\partial\Omega}{\partial r}+\frac{(u_\theta+\bar{v}_\theta)}{r}\frac{\partial\Omega}{\partial\theta} &= \nu[\frac{1}{r}\frac{\partial}{\partial r}(r\frac{\partial\Omega}{\partial r})+\frac{1}{r^2}\frac{\partial^2\Omega}{\partial\theta^2}] \\ &+ \frac{1}{\rho}[\frac{1}{r}\frac{\partial(rF_{l\theta})}{\partial r}-\frac{1}{r}\frac{\partial F_{lr}}{\partial\theta}] \qquad (5.9)\end{aligned}$$

where the dimensionless variables and the exponential-polar system of coordinates (ξ,η) introduced in Chapter 2 have been used. After performing a similar analysis to derive the equation for the streamfunction, we obtain the *vorticity/streamfunction* formulation of the Navier-Stokes equations in the transformed system of coordinates.

$$\begin{aligned}E\frac{\partial\Omega}{\partial t}+\frac{\partial(U_r\Omega)}{\partial\xi}+\frac{\partial(V_\theta\Omega)}{\partial\eta} &= \frac{2}{Re}(\frac{\partial^2\Omega}{\partial\xi^2}+\frac{\partial^2\Omega}{\partial\eta^2}) \\ &+ NE^{\frac{1}{2}}(\frac{\partial F_\theta}{\partial\xi}+2\pi F_\theta-\frac{\partial F_r}{\partial\eta}) \qquad (5.10)\end{aligned}$$

$$\frac{\partial^2\Psi}{\partial\xi^2}+\frac{\partial^2\Psi}{\partial\eta^2} = -E\Omega \qquad (5.11)$$

where

$$\begin{aligned}U_r &= E^{\frac{1}{2}}(u_r+\bar{u}_r)=\frac{\partial\Psi}{\partial\eta} \\ V_\theta &= E^{\frac{1}{2}}(u_\theta+\bar{u}_\theta)=-\frac{\partial\Psi}{\partial\xi} \\ E &= 4\pi^2e^{4\pi\xi}\end{aligned}$$

From the above derivation, we see that the equations of motion for the flow-induced vibrations in the transformed moving system of coordinates are identical to the equations of motion in the fixed system of coordinates for the fixed cylinder given in chapter 2. These simple relations facilitate our computational scheme.

When the cylinder is free to move in the cross-flow (y) direction, the equation of motion for the cylinder needs to be modeled. This is achieved through the forced vibration string equation with damping, where the spring is assumed to be mounted

by a linear spring damper mass system. The forced vibrating string equation with damping is given by Griffin (1992) and Blackburn (1996) as

$$\frac{d^2y(t)}{dt^2} + 2\alpha\omega_n\frac{dy(t)}{dt} + \omega_n^2 y(t) = \frac{F_{ty}(t)}{m}, \tag{5.12}$$

where $y(t)$ denotes the cylinder displacement in the cross-flow direction, α refers to the structural damping factor, m is the mass per unit length of the cylinder, $\omega_n = \sqrt{k/m} = 2\pi f_n$ is the angular natural frequency of the cylinder, k is the spring stiffness and F_{ty} is the total force exerted by the fluid onto the cylinder in the cross-flow direction.

The force $y-$ component of the force $F_{ty}(t)$ exerted by the fluid on the cylinder can be computed from the control volume formulation of the momentum equation in the fashion presented in Chapter 2. Starting with the definition of the lift coefficient $C_l = \frac{F_{ty}}{\frac{1}{2}\rho d u_\infty^2}$, we can write

$$\frac{F_{ty}(t)}{m} = \frac{1}{2}C_l u_\infty^2 \frac{\rho d}{m},$$

where we have assumed that the mass ratio $M^* = \frac{m}{\rho d^2}$ is equal to 1, and d denotes the diameter of cylinder. Considering the following dimensionless variables

$$y^* = y/d, \qquad t^* = tu_\infty/d, \qquad \omega_n^* = \omega_n d/u_\infty,$$

the dimensionless displacement of the cylinder (5.16) is given by

$$\frac{d^2y^*}{dt^{*2}} + 2\alpha\omega_n^*\frac{dy^*}{dt^*} + \omega_n^{*2}y^* = \frac{1}{2}C_l. \tag{5.13}$$

The coupled *fluid/cylinder* problem is solved in three steps, using the same method as that used by Newman and Karniadakis (1997). First, given the cylinder

motion $y(t)$, the fluid equations (5.10), (5.11) are solved. Then, the lift force on the cylinder is computed. Finally, the cylinder motion is updated using Equation (5.13).

The same numerical methods as those described in Chapter 2 has been used, that is the alternating-direction-implicit (ADI) algorithm to solve the vorticity transport equation (5.10), and the efficient algorithm using fast Fourier transforms (FFT) to solve the Poisson equation (5.11) with second-order accuracy. The displacement equations (5.13) are solved using the Runge-Kutta method. Everywhere except on the surface of the cylinder, the flow is potential initially, i.e. at $t = 0$.

5.2 Numerical Results

Numerical calculations are carried out for a number of cases for the two Reynolds number values $Re = 100$ and $Re = 200$. In all cases, we assume that the cylinder is free to vibrate in the cross-flow direction (only) and that the mass ratio is chosen to be equal to 1.

5.2.1 Vibrations Without Control

In a forced linear mass damper system, when the forcing frequency is close to the damped natural frequency, the mass oscillates at the forcing frequency and the maximal response amplitude occurs. In order to obtain a significant flow-induced vibration response, we adjust the natural frequency of the cylinder vibration to the frequency of vortex shedding. The fixed-cylinder vortex shedding frequency can be used in this estimation (Newman and Karniadakis 1997). At Reynolds numbers $Re = 100$ and $Re = 200$, the Strouhal number of the fixed cylinder is $St = 0.167$ and $St = 0.207$, respectively. Griffin (1992) has compiled many experimental data from several investigations and shown that the amplitude of cylinder vibrations seems to

follow a universal curve when plotted against the mass-damping or reduced damping parameter S_g, defined as

$$S_g = 8\pi^2 St^2 \alpha \frac{m}{\rho d^2}.$$

as before, St denotes the Strouhal number, $St = 2af/u_\infty$, and f refers to the vortex shedding frequency. Newman & Karniadakis (1997) have compared their numerical results with the experimental data compiled by Griffin (1992). Both results show an amplitude limiting response as the mass-damping parameter (S_g) tends to zero and a decrease of the vibration amplitude as S_g increases. However, the numerical simulations underpredict the cylinder vibration amplitude for low values of S_g and overpredict the cylinder vibration amplitude for high values of S_g. Newman & Karniadakis (1997) explain this discrepancy by the fact that three-dimensionality must play a dominant role in cylinder response which their two-dimensional simulation does not capture, while the Reynolds number for the experimental investigations well cover the three-dimensional regime, varying from $Re = 300$ to $Re = 10^6$.

Figure 5.1 allows to compare our numerical results with those of Newman & Karniadakis at $Re = 100$. Our results are in good agreement with theirs, in particular showing the same trend with respect to the mass-damping parameter. Our maximal amplitude of the cylinder vibration at $Re = 200$ is approximately one cylinder diameter, which also agrees well with Newman & Karniadakis (1997)'s findings. Figures 5.2 and 5.3 display the time varying displacement of the cylinder in the cross-flow direction for the two sets of parameter values $Re = 100$, $S_g = 0.3$, and $Re = 200$, $S_g = 0.1$. Examples of streamlines and relative vorticity contours for the first set of parameter values ($Re = 100$ and $S_g = 0.3$) are shown in Figure 5.4 over one half-cycle of the cylinder motion, starting with the cylinder in its upper

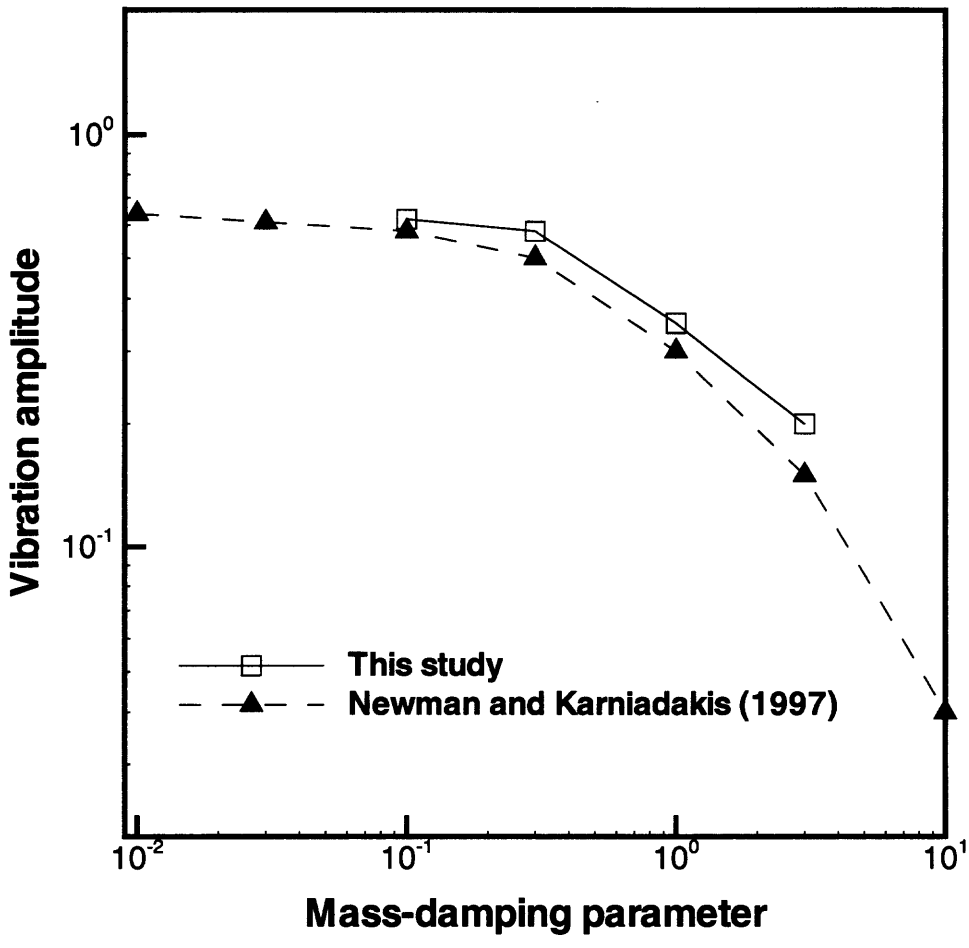

Figure 5.1 Vortex-induced vibration amplitude versus the mass-damping parameter at $Re = 100, M^* = 1$.

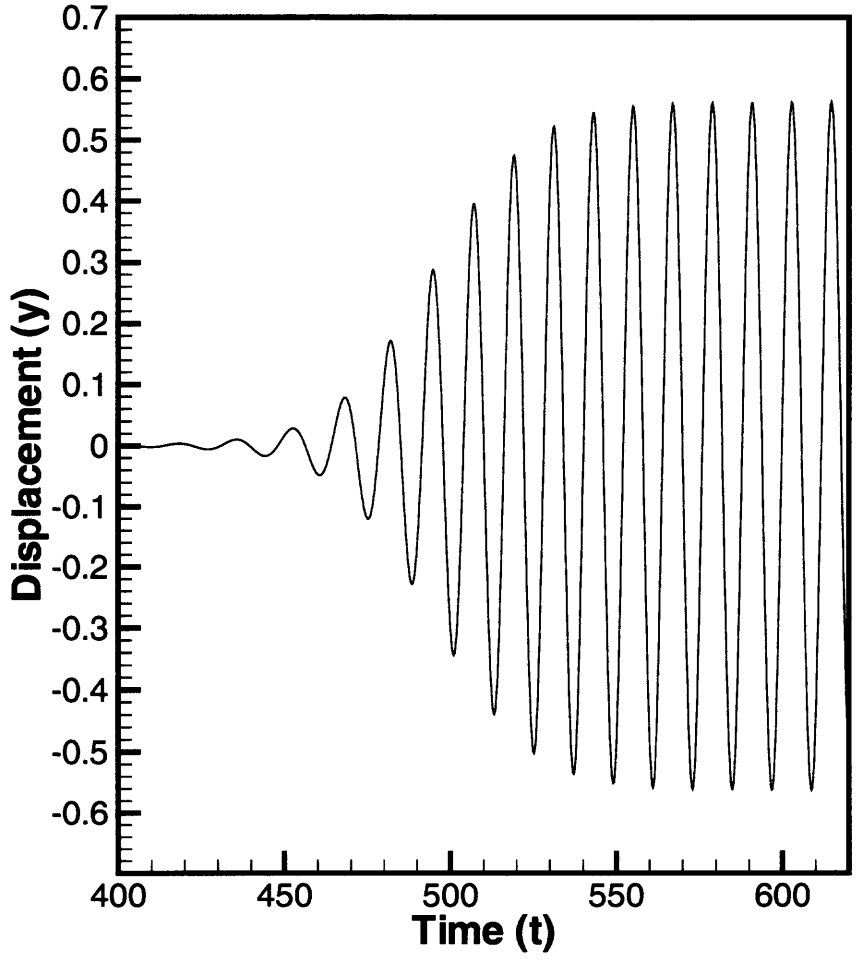

Figure 5.2 Trajectory of the moving cylinder subjected to flow-induced vibrations without control at the parameter values $Re = 100$, $S_g = 0.3$.

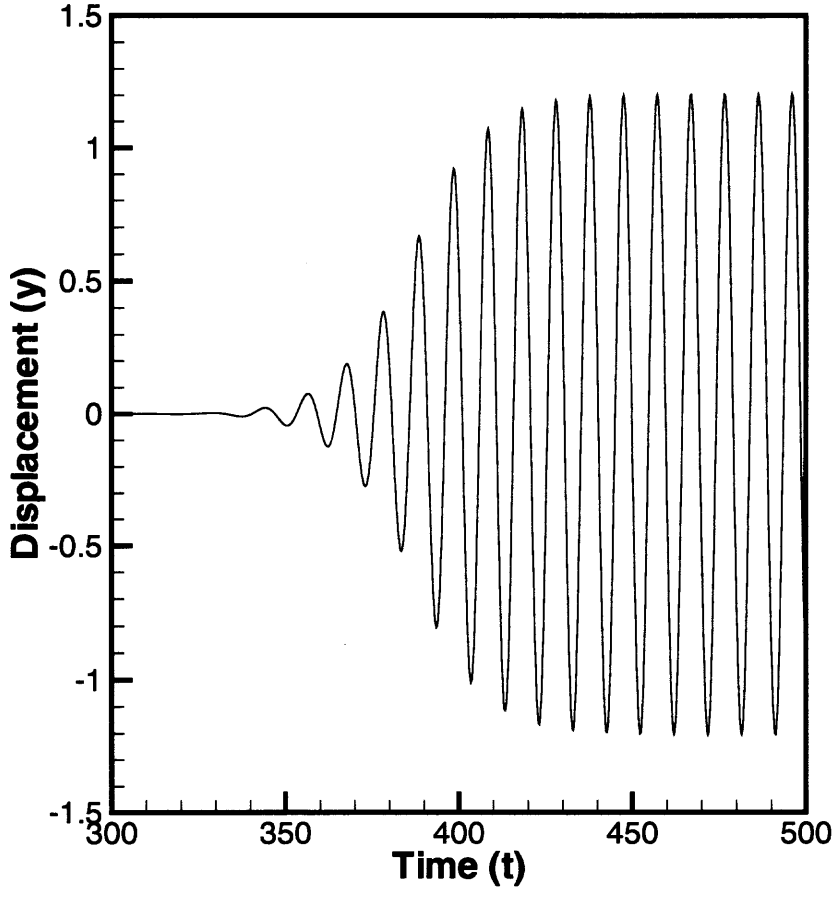

Figure 5.3 Trajectory of the moving cylinder subjected to flow-induced vibrations without control at the parameter values $Re = 200, S_g = 0.1$.

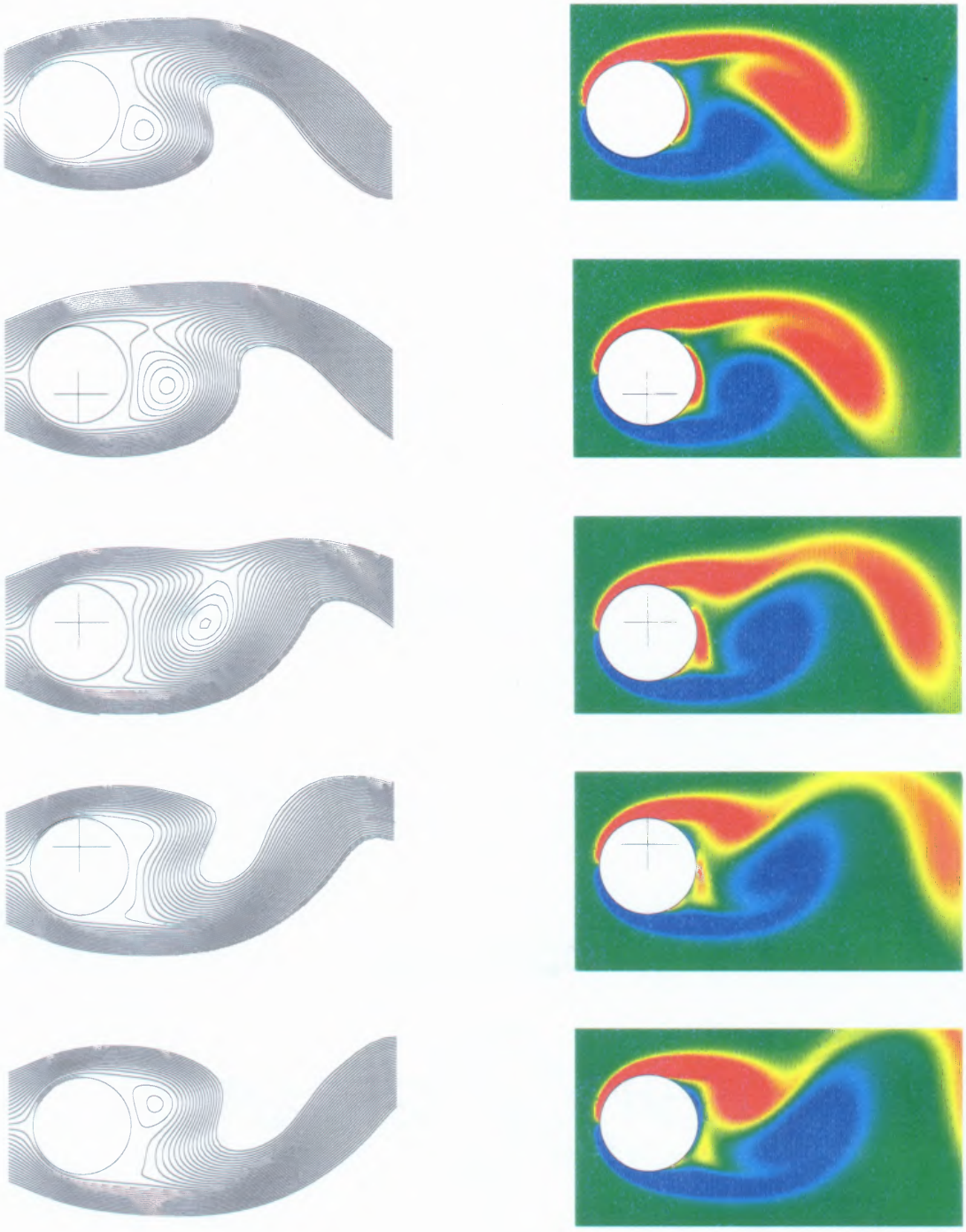

Figure 5.4 Instantaneous streamlines and vorticity contours over half a cycle for the vortex induced vibration problem with amplitude $A = 0.56$ at the parameter values $Re = 100$, $S_g = 0.3$.

position. The frequency of the cylinder vibration is identical to the frequency of vortex shedding.

5.2.2 Suppression of Vibrations By Closed-Loop Control

In this section, we apply the closed-loop control technique ($C_d = 0$) developed in Section 4.1, in order to control the vibrations of the cylinder at the two Reynolds number values $Re = 100$ and $Re = 200$. The closed-loop control algorithm is applied starting at time $t = 600$ for $Re = 100$ and at $t = 500$ for $Re = 200$.

Figures 5.5 and 5.6 display the time history of the cylinder displacement before and after control for both sets of parameters $Re = 100$, $S_g = 0.3$, and $Re = 200$, $S_g = 0.1$. Before control, the cylinder vibrates with the same frequency of vortex shedding, and the amplitude of the vibration is about 0.56 for $Re = 100$ and 1.20 for $Re = 200$. After our closed-loop control algorithm is turned on, the amplitude of the cylinder decreases with time until it reaches the zero value.

Figure 5.7 shows the time history of the interaction parameter at $Re = 100$ and $Re = 200$. It is clear that the control of the cylinder vibration at $Re = 200$ requires a larger interaction parameter than at $Re = 100$. When this result is compared to the fixed cylinder case reported in Figure 4.8a, one observes that the control of the flow at Reynolds number $Re = 200$ requires a longer time and a larger Lorentz force when the cylinder is free to vibrate.

Figure 5.8 shows the streamline and vorticity contours of the steady solution obtained after the control algorithm is applied and when the cylinder is free to vibrate (here, $Re = 100$). Streamlines and vorticity contours recorded at various times that illustrate the destabilization of vortex shedding can be observed in Figures 5.9 and 5.10.

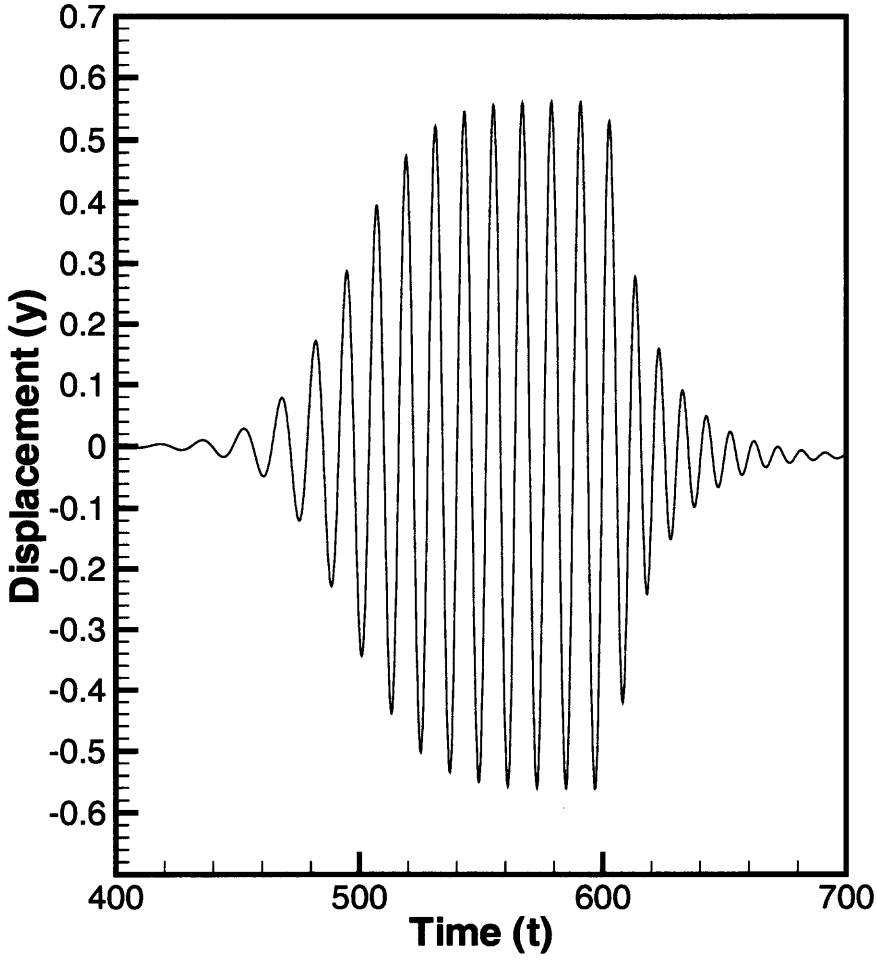

Figure 5.5 Displacement of the free cylinder before and after control is applied for the parameter values at $Re = 100, S_g = 0.3$.

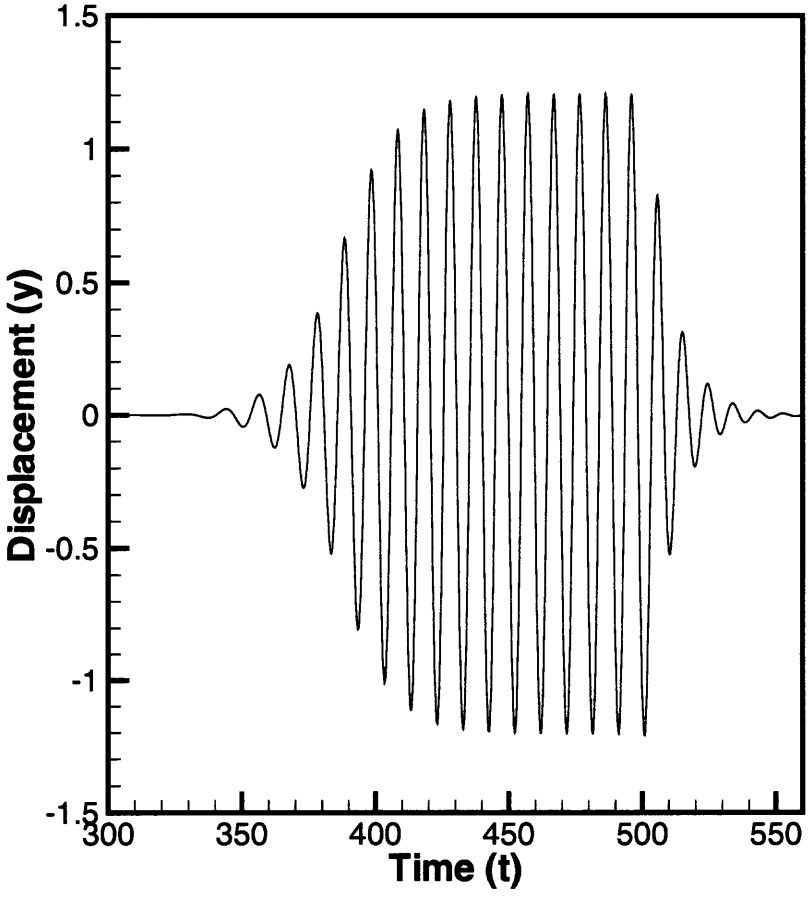

Figure 5.6 Displacement of the free cylinder before and after control is applied for the parameter values $Re = 200, S_g = 0.1$.

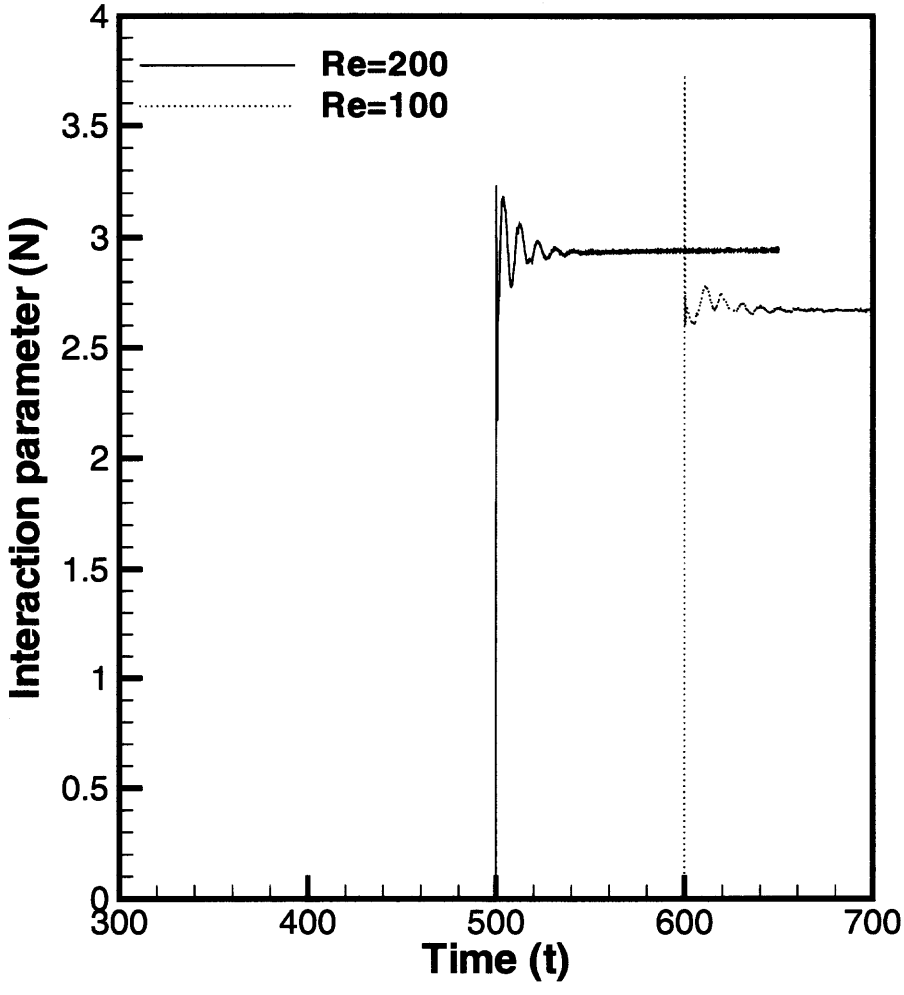

Figure 5.7 Time history of the interaction parameter for the controlled flow corresponding to the free cylinder at the two sets of parameter values $Re = 100$, $S_g = 0.3$, and $Re = 200$, $S_g = 0.1$.

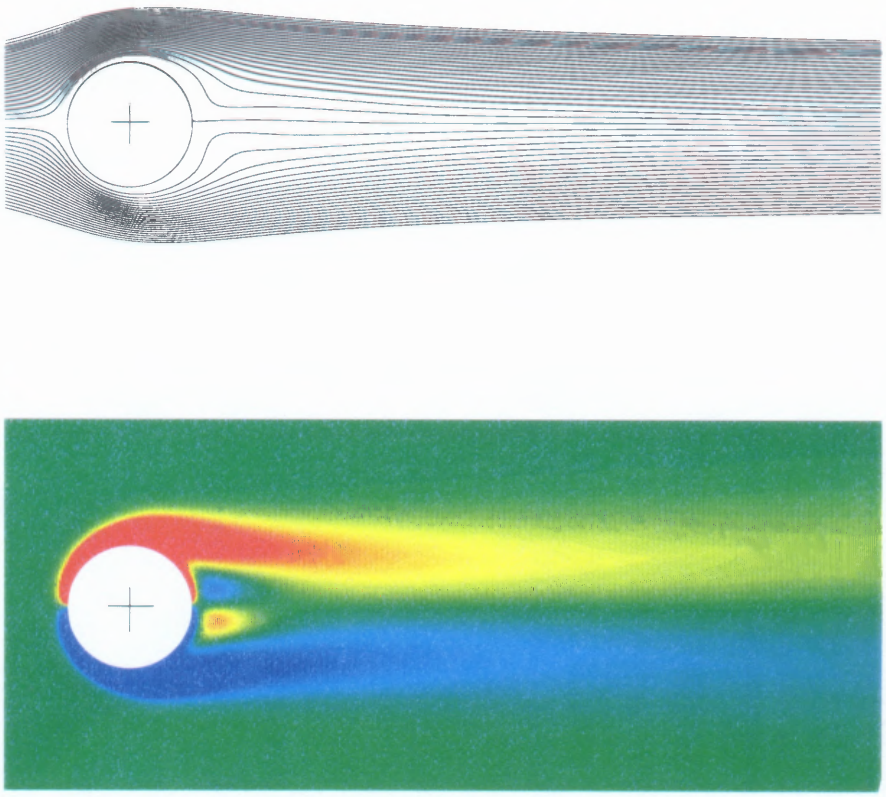

Figure 5.8 Streamlines and vorticity contours of the steady flow solution obtained after controlling the vortex-induced vibration problem (at time $t = 700$) at the parameter values $Re = 100$ and $S_g = 0.3$.

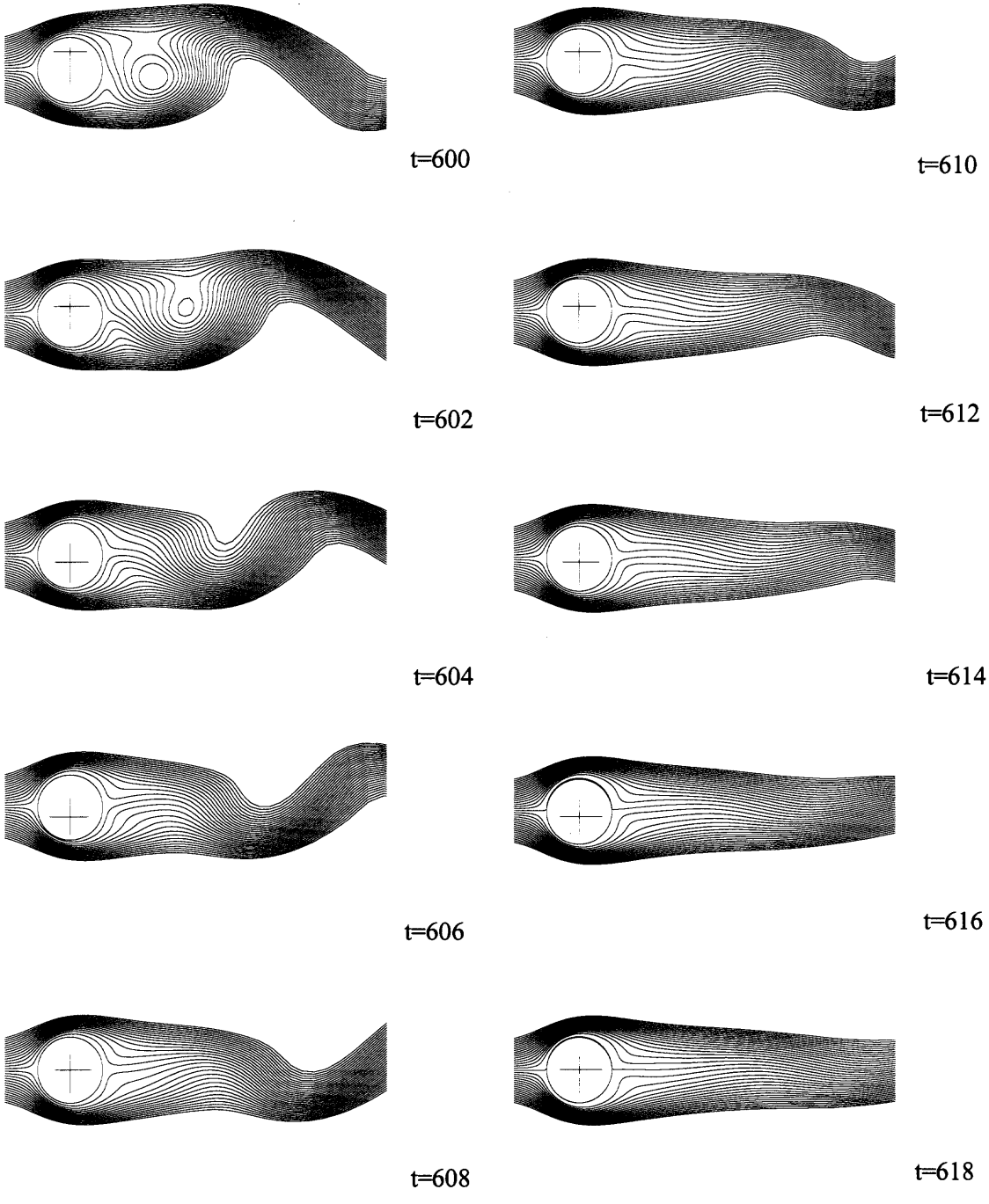

Figure 5.9 Instantaneous streamlines at various times showing the suppression of flow induced vibrations under the action of our control algorithm for the parameter values $Re = 100, S_g = 0.3$. The cross corresponds to the initial location of the center of the cylinder.

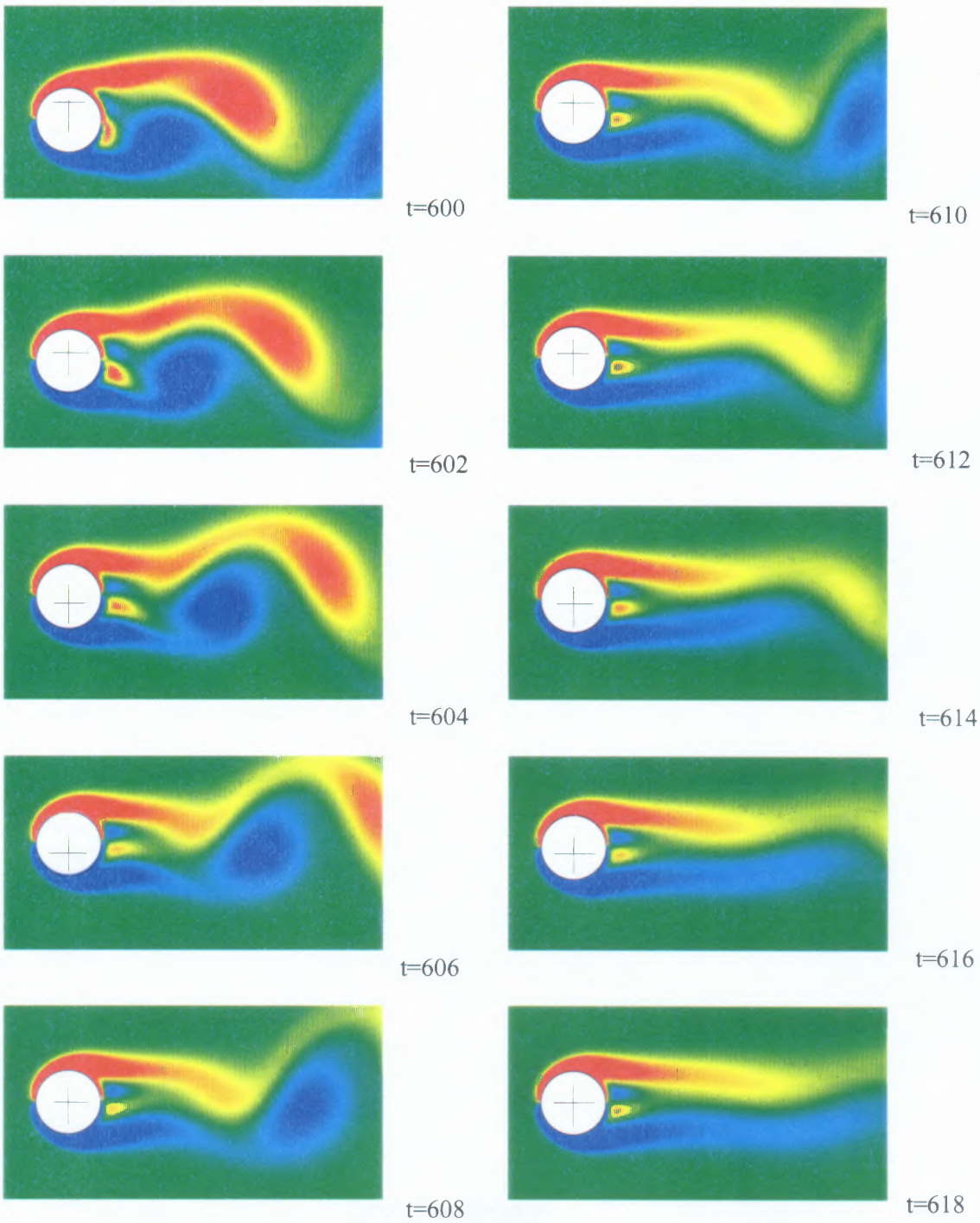

Figure 5.10 Instantaneous vorticity contours at various times showing the suppression of flow induced vibrations under the action of our control algorithm for the parameter values $Re = 100, S_g = 0.3$.

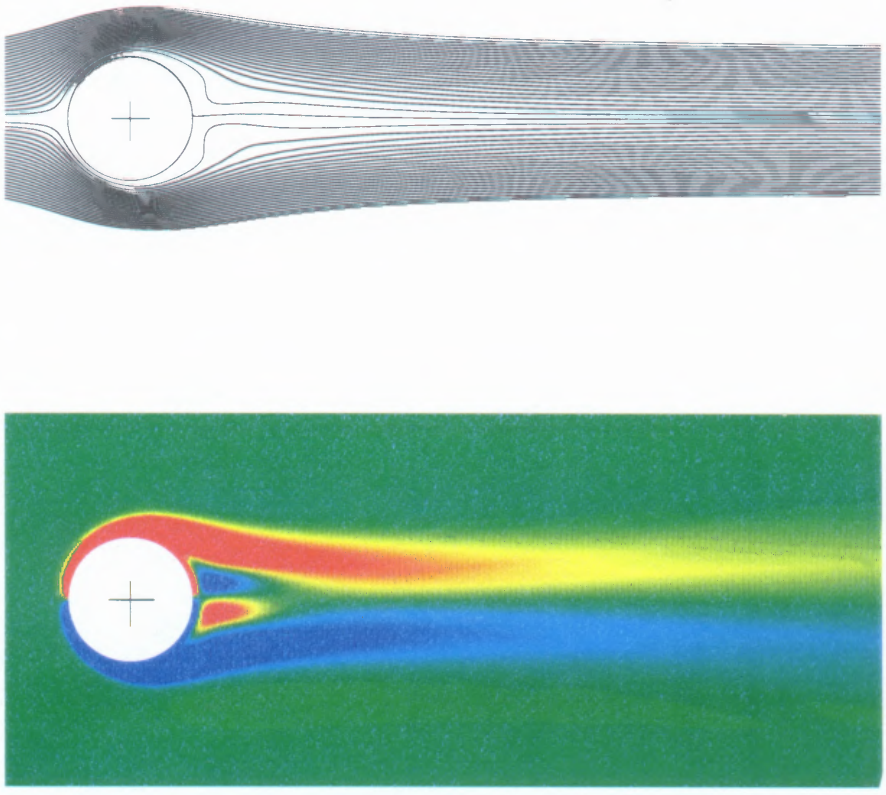

Figure 5.11 Streamlines and vorticity contours of the flow steady solution obtained after controlling the vortex-induced vibration problem (here, time is $t = 550$) at the parameter values $Re = 200, S_g = 0.1$.

Figures 5.11, 5.12 and 5.13 are similar to Figures 5.8, 5.9 and 5.10 but were obtained at Reynolds number $Re = 200$, instead of $Re = 100$.

5.3 Summary

In this chapter, vortex-induced vibrations of a cylinder has been simulated numerically in the cross-flow direction at the Reynolds number values $Re = 100$ and $Re = 200$. The results presented correspond to the well-documented lock-in response

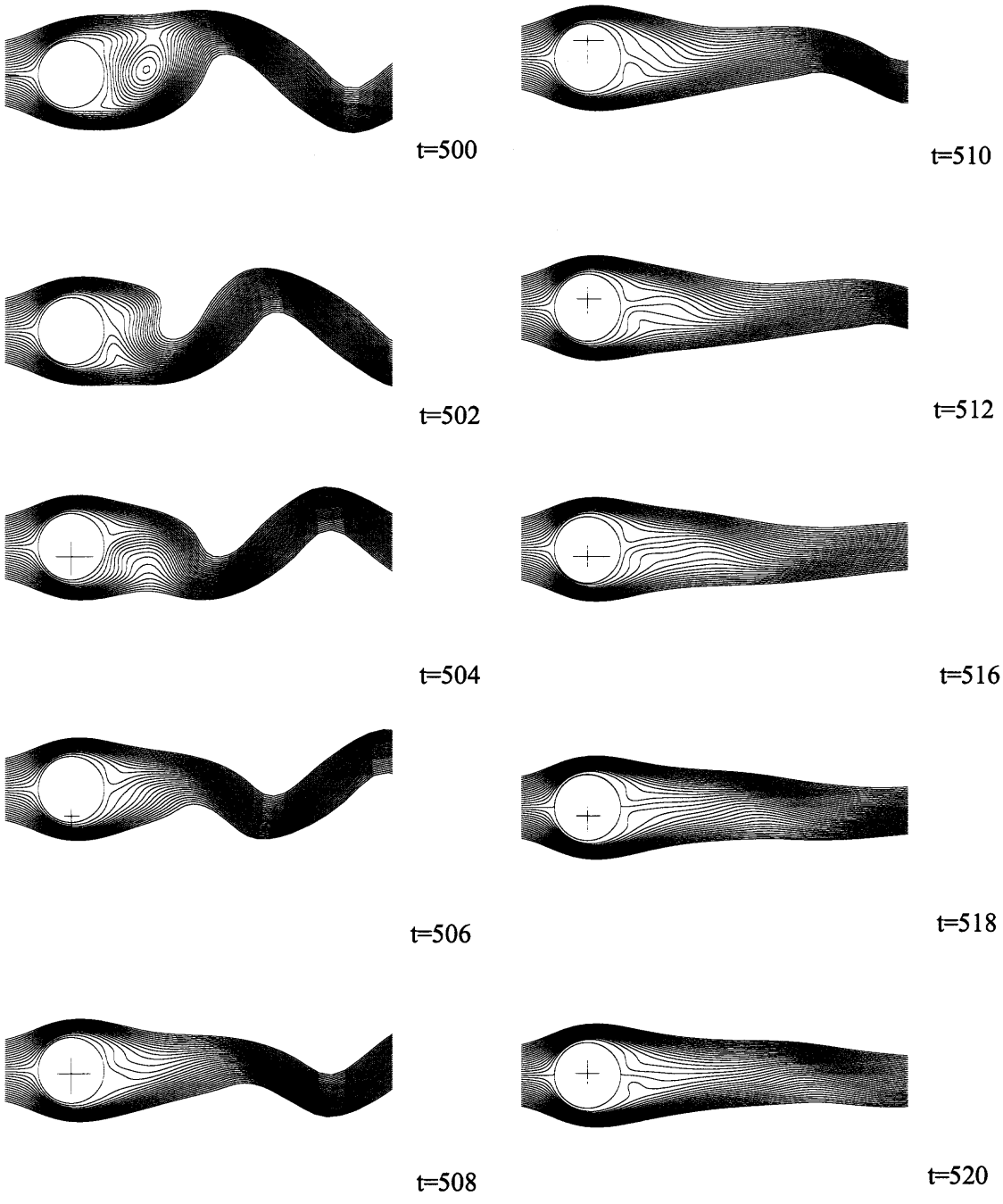

Figure 5.12 Instantaneous streamlines at various times showing the suppression of flow induced vibrations under the action of our control algorithm for the parameter values $Re = 200, S_g = 0.1$.

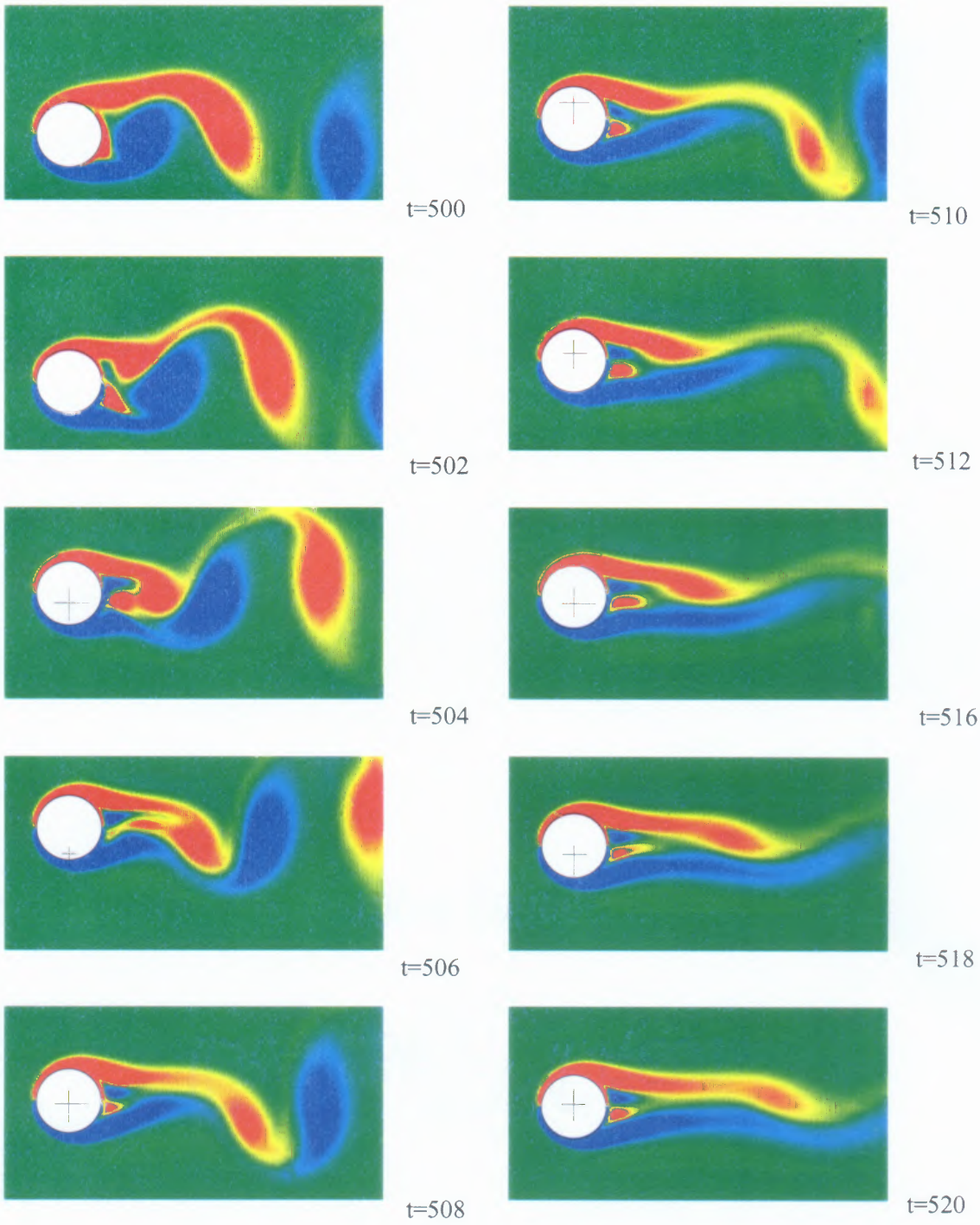

Figure 5.13 Instantaneous vorticity contours at various times showing the suppression of flow induced vibrations under the action of our control algorithm for the parameter values $Re = 200, S_g = 0.1$.

and are in good agreement with previous experimental and numerical results. The closed-loop control algorithm targetting zero drag coefficient, i.e. $C_d = 0$, which was developed in Section 4.1, was applied successfully to suppress the cylinder flow-induced vibration at the Reynolds number values $Re = 200$ and $Re = 100$. Our numerical results show that the suppression of flow-induced vibrations requires a longer time and a larger interaction parameter (larger Lorentz force) than the suppression of vortex shedding in the fixed cylinder case.

CHAPTER 6

CONCLUSIONS

In this dissertation, we have developed both open and closed-loop electro-magnetic control procedures for manipulating wake flows past a circular cylinder in an electrically low-conducting fluid (*e.g.* seawater). The intent was to avoid both vortex shedding and flow separation from the body, as well as reduce the mean drag significantly and prevent the lift from becoming non-zero at all times. This was achieved through the introduction of a Lorentz force in the azimuthal direction generated by an array of permanent magnets and electrodes located on the solid structure.

Regarding the open loop control methods, static Lorentz forces were applied on either the whole cylinder surface or a portion of it. When the Lorentz force is distributed on the whole surface, vortex shedding behind the cylinder weakens as the Lorentz force increases, and eventually disappears. The total drag coefficient is always smaller than the value it had when the Lorentz force was turned off. which is in good agreement with the results of Weier *et al*(1998). Localized Lorentz forces along the rear surface of the cylinder were also used to control vortex shedding. Our numerical results show that the efficiency of localized Lorentz forces is almost identical to that of the Lorentz forces applied to the entire surface. The total drag coefficient decreases as the Lorentz force intensity increases. Time periodic Lorentz forces were also explored, with the Lorentz force frequency higher than the Strouhal frequency. In this case, when the interaction parameter was properly chosen, the cylinder flow coincided with a vortex street with a smaller width than in the unforced case. For force frequencies near the Strouhal frequency, the lock-in phenomenon occurs even for small interaction parameter values. In this case, the frequency of the flow is determined by the Lorentz force frequency. As the Lorentz force frequency

increases, the flow exhibits two different frequencies, one coinciding with the Lorentz force frequency, and the other one corresponding to the natural shedding frequency.

Closed-loop control procedures were developed targetting either zero total drag coefficient, $C_d = 0$, or zero pressure drag coefficient, $C_p = 0$. The location of sensors for both types of feedback was limited to the surface of the cylinder and consisted in recording the wall shear stress. Actuators was simulated by the action of the Lorentz force on the cylinder surface. The value of the interaction parameter (or intensity of the Lorentz force) was calculated from the requirement that $C_d = 0$ or $C_p = 0$, depending on the case considered. When the control algorithm based on $C_d = 0$ was applied, vortex shedding completely disappeared, and the flow stabilized to a steady solution in a short amount of time. The total drag and lift coefficient were reduced to zero successfully, while the pressure drag reached a negative value in order to balance the friction drag. When the closed-loop control based on zero pressure drag coefficient, $C_{pd} = 0$, was applied, vortex shedding also disappeared but the process took longer than in the previous case ($C_d = 0$). The steady solution the flow reaches under control has a nearly zero lift, and a friction drag and interaction parameter smaller than in the previous case ($C_d = 0$).

Finally, the vortex-induced vibration of the cylinder has been simulated numerically in the cross-flow direction at Reynolds number values $Re = 100$ and $Re = 200$. The results presented correspond to the lock-in response, as previous experimental and numerical results were available in this regime. The previous closed-loop control ($C_d = 0$) algorithm previously developed was applied successfully to the control of cylinder vibrations at both Reynolds numbers ($Re = 200$ and $Re = 100$). Our numerical results have shown that the control of cylinder vibrations requires a longer time and more energy (that is, a larger interaction parameter, and therefore a more intense Lorentz force) than the flow corresponding to a fixed cylinder.

REFERENCES

1. Abergei, F. & Termam, R. 1990 On some control problems in fluid mechanics. Theor. Comput. Fluid Dyn., **1**, 303.

2. Apelt, C. J. & West, G. S., 1975 The effects of wake splitter plates on bluff-body flow in the range $10^4 < R < 5 \times 10^4$, Part2: J. Fluid Mech. **71**, 145.

3. Apelt, C. J., West, G. S. & Szewczyk, A. A., 1973 The effects of wake splitter plates on the flow past a circular cylinder in the range $10^4 < R < 5 \times 10^4$. J. Fluid Mech. **61** , 187.

4. Aubry, N. & Tang, S. 1998 Controlling vortex shedding by insertion of vortices. Proceedings of the ASME Fluids Engineering Division Summer Meeting. June 21-25, Washington, D.C.

5. Bearman, P. W. 1967 The effect of base bleed on the flow behind a two-dimensional model with a blunt trailing edge. Aero. Q. **18**, 207.

6. Blackburn, H. M. & Karniadakis, G. E. 1993 Two and three-dimensional simulations of vortex induced vibration of a circular cylinder. Proc. 3rd Inst Offshore and Polar Engng conf. Singapore, **3**, 715-720.

7. Blackburn, H. & Henderson, R. 1996 Lock-in behavior in simulated vortex-induced vibration. Experimental Thermal and Fluid Science **12**, 184-189.

8. Blevins, R. D. 1990 Flow Induced Vibration. Van No strand Reinhold Company. New York

9. Blevins, R. D. 1985 The effect of sound on vortex shedding from cylinders. J. Fluid Mech. **161**, 217.

10. Bouard, R. & Coutanceau, M. 1980 The early stage of development of the wake behind an impulsively started cylinder for $40 \leq Re \leq 10^4$. J. Fluid Mech. **101**, 583-607.

11. Brika, D., & Laneville, A. 1993 Vortex-induced Vibration of a Long Flexible Circular Cylinder. J. Fluid Mech. **250**, 481-508.

12. Wood, C. J. 1967 Visualization of an incompressible wake with base bleed. J. Fluid Mech. **29**, 259-272.

13. Chang, C. C. & Chern, R. L. 1991 A numerical study of flow around an impulsively started circular cylinder by a deterministic vortex method. J. Fluid Mech. **233**, 246-263.

14. Choi, H., Temam, R., Moin, P. & Kim, J. 1993 Feedback control for unsteady flow and its application to the stochastic Burgers equation. J. Fluid Mech. **253**, 509.

15. Cimbala, J. M. and Garg, S. 1991 Flow in the wake of a freely rotatable cylinder with splitter plate. AIAA J. **29**, 1001.

16. Collins, W. M. & Dennis, S. C. R. 1973 Flow past an impulsively started circular cylinder. J. Fluid Mech. **60**,105-127.

17. Crawford, C. & Karniadakis, G. E. 1997 Reynolds stress analysis of EMHD-controlled wall turbulence. Part I Streamwise forcing. Phys. Fluids , **9**, No. 3, 788-806.

18. Dimas, A. A & Triantafyllou, G. S. 1994 Nonlinear interaction of shear flow with a free surface. J. Fluid Mech. **260**, 211-246.

19. Dutsch, H., Durst, F., Becker, H. & Lienhart, H. 1998 Low Reynolds number flow around an oscillating circular cylinder at low Keulegan-Carpenter numbers. J. Fluid Mech. **360**, 249-271.

20. Fowcs Williams, J. E. & Zhao, B, C. 1988 The active control of vortex shedding In Intel. Symp. on flow induced vibration and noise. ASME **1**, 51-60.

21. Gailitis, A. & Lielausis, O. 1961 On a possibility to reduce the htdrodynamical resistance of a plate in an electrolyte. Applied Magnetohydrodynamics. Reports of the Physics Institute Riga **12**, 143-146.

22. Gerrard, J. H. 1966 The mechanics of the formation region of vortices behind bluff bodies. J. Fluid Mech. **25**, 401.

23. Griffin, O. M. 1992 Vortex-induced vibrations of bluff bodies. NSF workshop on Riser Dynamics, University of Michigan.

24. Griffin, O. M. 1972 Flow near self-excited and forced vibrating circular cylinders. J. Engng. Industry, May 1972, 539-547.

25. Griffin, O. M. & Hall, M. S. 1991 Review: Vortex Shedding Lock-on Control in Bluff Body Wakes. Journal of Fluids Engineering. **113**, 526-537.

26. Griffin, O. M. & Koopmann, G. H. 1977 The vortex-exited lift and reaction forces on resonantly vibrating cylinders. Journal of Sound and Vibration.

27. Gu, W., Chyu, C. & Rockwell, D. 1994 Timing of vortex formation from an oscillating cylinder. Physics of Fluids **6**, 3677-3682.

28. Gunzburger, M. D. & Lee, H. C. 1996 Feedback control of Karman vortex shedding. Journal of Applied Mechanics, **63**, 828-835.

29. Hammache, M. & Gharib, M. 1991 An experimental study of the parallel and oblique vortex shedding from circular cylinder. J. Fluid Mech. **232**, 567-590.

30. Hartlen, R. T. & Currie, J. G. 1970 Lift oscillator model of vortex induced vibration. J. Engng. Mech. Div. ASCE, **96**, 577-591.

31. Henderson, R. D. & Karniadakis, G. E. 1995 Unstructured spectral element methods for simulation of turbulent flows. J. Comput. Phys. **122**, 191-217.

32. Henderson, R. D. & Barkley, D. 1996 Secondary instability in the wake of a circular cylinder. Phys. Fluid **8**, 1683-1685.

33. Henoch, C. & Stace, J. 1995 Experimental investigation of a salt water turbulent boundary layer modified by an applied streamwise magneto-hydrodynamic body force. Phys. Fluids **7** (6), 1371-1383.

34. Hover, F. S., Techet, A. H. & Triantafyllour, M.S. 1998 Forces on oscillating uniform and tapered cylinders in crossflow. J. Fluid Mech. **363**, 97-114.

35. Hover, F. S., Miller, S. N. & Triantafyllou, M. S. 1997 Vortex induced vibration of marine cables: Experiments using force feedback. J. Fluids and Structures **11**, 307.

36. Hover, F. S., Miller, S. N., & Triantafyllou, M. S. 1997 Vortex-induced vibration of marine cables: Experiments using force feedback. J. Fluid Struct. **11**, 306-326.

37. Kang, S. & Choi, H. 1999 Laminar flow past a rotating circular cylinder. Phys. Fluids **11**, 3312.

38. Karniadakis, G. E. & Triantafyllou, G. S. 1989 Frequency selection and asymptotic states in laminar wakes. J. Fluid Mech. **199**, 441-469.

39. Kwon, K. & Choi, H., 1996 Control of laminar vortex shedding behind a circular cylinder using splitter plates. Phys. Fluids **8**, 479.

40. Lahjomri, J., Caperan, P. & Alemany, A. 1993 The cylinder wake in a magnetic field aligned with the velocity. J. Fluid Mech. **253**, 421-448.

41. Lin, X. W., Bearman, P. W. & Graham, J. M. 1996 A numerical study of oscillatory flow about a circular cylinder for low values of Beta parameter, J. Fluid Struct. **10**, 501.

42. Lu, X. Y. & Dalton, C. Calculation of the timing of vortex formation from an oscillating cylinder. J. Fluids Struct. **10**, 527.

43. Min, C. & Choi, H. 1999 Suboptimal feedback control of vortex shedding at low Reynolds numbers. J. Fluid Mech. **401**, 123-156.

44. Monkewitz, P. A., Berger, E. & Schumm, M. 1989 Feedback control of global oscillations in fluid systems. AIAA Paper **89**(0991).

45. Mutschke, G., Gerbeth, G., & Shatrov, V. 1997 Two- and three-dimensional instabilities of the cylinder wake in an aligned magnetic field. Phys. Fluids **9**, 3114.

46. Mutschke, G., Shatrov, V. & Gerbeth, G. 1998 Cylinder wake control by magnetic fields in liquid metal flows. Experimental Thermal and Fluid Science **16**, 92-99.

47. Naudascher, E. 1987 Flow-induced streamwise vibration of structures. J. Fluid Struct. **1**, 265-298.

48. Newman, D. J. & Karniadakis, G. E. 1995 Direct numerical simulations of flow over a flexible cable. Proc. sixth Intl Conf. on Flow-Induced Vibration, 193-203. Balkema, Rotterdam.

49. Newman, D. & Karniadakis, G. E. 1996 Simulations of flow over a flexible cable: A comparison of forced and flow induced vibration. J. Fluid Struct. **10**, 439-453.

50. Newman, D. J. & Karniadakis, G. E. 1997 A direct numerical simulation study of flow past a freely vibrating cable. J. Fluid Mech. **344**, 95-136.

51. Nosenchuck, D. M., Brown, G. L., Culver, H. C., Eng, T. I. & Huang, I. S. 1995 Spatial and temporal characteristics of boundary layers controlled with the Lorentz force. 12^{th} Australian Fluid Mechanics Conference, Sydney.

52. Obasaju, E. D., Ermshaus, R. & Naudascher, E. 1990 Vortex-induced streamwise oscillations of a square-section cylinder in a uniform stream. J. Fluid Mech. **213**, 171-189.

53. Ongorem, A. & Rockwell, D. 1988 Flow Structures from an Oscillating Cylinder. Part 1. Mechanisms of Phase Shift and Recovery in the Near Wake. J. Fluid Mech. **191**, 197-223.

54. Ongoren, A. & Rockwell, D. 1988 Flow structure from an oscillating cylinder, Part 1: Mechanisms of phase shift and recovery in the near wake. J. Fluid Mech. **191**, 197 -223.

55. Papangelou, A. 1992 Vortex shedding from slender cones at low Reynolds numbers. J. Fluid Mech. **242**, 229-321.

56. Park, D. S., Ladd, D. M. & Hendricks, E. W. 1993 Feedback back control of a global mode in spatially developing flows. Phys. Lett. **182**, 224.

57. Park, D. S., Ladd, D. M. & Hendricks, E. W. 1994 Feedback back control of von karman vortex shedding behind a circular cylinder at low Reynolds numbers. phys. Fluids **6**, 2390-2405.

58. Roussopoulos, K. 1993 Feedback control of vortex shedding at low Reynolds numbers. J. Fluid Mech. **248**, 267.

59. Schewe, G. 1983 On the force fluctuations acting on a circular cylinder in crossflow from subcritical up to transcritical Reynolds numbers. J. Fluid Mech. **133**, 265-285.

60. Schumm, M,, Berger, E. & Monkewitz, P. A. 1994 Self-excited oscillations in the wake of two-dimensional bluff bodies and their control. J. Fluid Mech. **271**, 17.

61. Sheridan, J. & Carberry, J. 1998 Special brief note on the near-wake topology of an oscillation cylinder. Journal of Fluids and Structures **12**, 215-220.

62. Smith, P. A. & Stansby, P. K. 1988 Impulsively started flow around a circular cylinder by the vortex method. J. Fluid Mech. **194**, 45-77.

63. Sritharan, S. S. 1992 An optimal control problem in exterior hydrodynamics. Proc. R. Soc. Edinburgh Scr. A, **121**, 5.

64. Sritharan, S. S. 1991 Dynamic programming of the Navier–Stokes equations. Syst. Control Lett. **16**, 299.

65. Strykowski, P. J. & Hannemann, H. 1991 Temporal simulation of the wake behind a circular cylinder in the neighborhood of the critical Reynolds number. Acta Mechanica, **90**, 1-20.

66. Tang, S. & Aubry, N. 1997 On the symmetry breaking instability leading to vortex shedding. Phys. Fluids **9**, (9), 2550-2560.

67. Tanida. Y., Okajima, A. B., Watanabc, Y. 1973 Stability of a circulated cylinder oscillating in uniform flow or in a wake. J. Fluid Mech. **61**, 769-784.

68. Tatsuno, M. and Bearman, P. W. 1990 A visual study of the flow around an oscillating circular cylinder at low Keulegan-Carpenter numbers and low Stokes numbers. J. Fluid Mech. **211**, 157-182.

69. Techet, A. H. & Triantafyllou, M. S. 1998 The evolution of a 'Hybrid' shedding mode. conference on bluff body wakes and vortex-induced vibration. **1** (4).

70. Tokumaru, P. T. & Dimotakis, P. E. 1991 Rotary oscillation control of a cylinder wake. J. Fluid Mech. **224**, 77-90.

71. Tokumaru, P. T. & Dimotakis, P. E. 1991 Rotary Oscillating Control of a Cylinder Wake. J. Fluid Mech. **224**, 77-90.

72. Triantafyllou, M.S. & Howell, C. T. 1992 Nonlinear impulsive motions of low-tension cables. J. Engng. Mech. **118**, 807-830.

73. Unal, M. F. & Rockwell, D. 1988 On vortex formation from a cylinder. Part 2. Control by splitter-plate interference. J. Fluid Mech. **190**, 513.

74. Warburton, T. C. & Karniadakis, G. E. 1996 The wake of oscillating cylinder close to a free surface. Bull. Am. Phys. Soc. **41**, 1732.

75. Wehrmann, O. H. 1965 Reduction of velocity fluctuations in a Karman vortex street by a vibrating cylinder. Phys. Fluids **8**, 760-761.

76. Weier, T., Gerbeth, G., Posdziech, O., Lielausis, O. & Platacis, E., 1998 Some results on electromagnetic control of flow around bodies. Proc. of the Intern. Symp. on Seawater Drag Reduction, Newport, Rhode Island, 395-400.

77. Weier, T., Gerbeth, G., Mutschke, G., Platacis, E. & Lielausis, O. 1998 Experiments on cylinder wake stabilization in an electrolyte solution by means of electromagnetic forces localized on the cylinder surface. Experimental Thermal and Fluid Science **16**, 84-91.

78. Williamson, C. H. K. 1996 Mode A secondary instability in the wake of a circular cylinder. Phys. Fluid **8**, 1683-1685.

79. Williamson, C. H. K. & Roshko, A. 1988 Vortex formation in the wake of an oscillating cylinder. J. Fluids Struct. **2**, 355-381.

80. Wood, C. J. 1964 The effect of base bleed on a periodic wake. J. R. Aeronaut. Soc. **68**, 477.

81. You, D., Choi, H., Choi, M. & Kang, S. 1998 Control of flow induced noise behind a circular cylinder using splitter plates. AIAA **36**, 1961.

82. Zhou, C. Y., So, R. M. C. & Lam, K. 1998 Vortex-induced vibrations on bluff bodies in a cross flow. *Proc. on Bluff Body Wakes and Vortex-induced Vibration.* ASME Fluids Engineering Division Summer Meeting, **12** (1), Washington, D.C. June 21-25.